WITS
UNIVERSITY

Colloidal synthesis of molybdenum diselenide nanomaterials for supercapacitor applications

ZAKHELE NDALA

(491384)

Supervisors: Ms Siziwe Gqoba and Prof Nosipho Moloto

Johannesburg, 2018

A dissertation submitted to the Faculty of Science, University of the Witwatersrand, in partial fulfilment of the requirements for the degree of Master of Science.

……
(Signature of candidate)

……
(Signature of supervisor)

……....
(Signature of Co-supervisor)

Declaration

I declare that the work reported herein is my own independent work. Submitted at the School of Chemistry, University of the Witwatersrand, Johannesburg. This work has not been submitted for any degree or examination in any other institution of higher learning.

……

(Signature of candidate)

Date:……..2018

Abstract

Herein we report on the synthesis of $MoSe_2$ nanomaterials using novel colloidal synthetic methods and their application as electrode materials in supercapacitors. Supercapacitors are energy storage devices with high power density and high cycle stability that can be used in applications that require rapid charge/discharge. The drawback in supercapacitors is their low energy density. Nanomaterials with high surface area are being explored as alternatives to activated carbon which has been a commonly used electrode material in supercapacitors. This is done to increase the energy density of supercapacitors. $MoSe_2$ has been identified as an excellent candidate for use as an electrode material in supercapacitors because of its interesting properties. $MoSe_2$ is a layered transition metal dichalcogenide (TMD) that is similar to graphene in structure and possesses interesting structural, optical and electronic properties. $MoSe_2$ also has a high surface to volume ratio. A colloidal synthetic process was used for the synthesis of the $MoSe_2$ nanomaterials, after which the effect of various reaction parameters was investigated. The reaction was run at 300 °C using oleylamine (OAm) as the solvent and surfactant. A time study on the synthesis of the nanomaterials revealed $MoSe_2$ few-layer nanosheets grow from a flocculate formed in the initial stages of the reaction (30 min). At longer reaction times (e.g. 90 min) the flocculate is consumed to form wrinkled few-layer nanosheets. A variation of the metal precursor in the reaction results in changes to the morphology of the $MoSe_2$ nanomaterials. The formation of the flocculate in the initial stages of the reaction when molybdenum hexacarbonyl is used as the metal precursor results in the formation of wrinkled few-layer nanosheets. The use of molybdic acid as the metal precursor results in the formation of nanoparticles with a central core which leads to the formation of $MoSe_2$ nanoflowers. The effect of adding a co-surfactant to the reaction system was also investigated. The effect of adding oleic acid as a co-surfactant in the reaction along with oleylamine resulted in changes to the thickness of the nanosheets synthesized and slight changes in the morphology. The use of 1-octadecene as a co-surfactant resulted in the increased reactivity of the selenium precursor which increased the number of nanosheets growing per nanoflower. The electrochemical properties of the $MoSe_2$ nanomaterials were investigated to determine the suitability of the nanomaterials for use as supercapacitor electrodes. The $MoSe_2$ nanomaterials synthesized using colloidal synthesis exhibited electric double layer capacitance behaviour. The effect of the morphology on the electrochemical performance of the $MoSe_2$ nanomaterials was investigated using $MoSe_2$ nanoflowers and few-layer nanosheets. The $MoSe_2$ nanoflowers were shown to have a higher specific capacitance at 81 Fg^{-1} than the few-layer nanosheets at 30 Fg^{-1}. The nanoflowers also had better capacitance retention at higher current densities in the charge-discharge analysis compared to the few-layer nanosheets. The nanoflowers had higher capacitance retention of 68% compared to 20% for the few-layer nanosheets. The nanoflowers also had a lower equivalence series resistance (ESR) of 34.0 Ω compared to that of the few-layer nanosheets at 57.1 Ω.

Acknowledgements

I would like to first and foremost express my gratitude to the almighty God for the life he has given me and the opportunity to pursue my dreams. Most importantly thank you to my wonderful parents and brothers, your love and support is what has got me where I am and is my greatest inspiration.

I would also like to express my sincere gratitude to my supervisors Prof Nosipho Moloto and Ms Siziwe Gqoba for their guidance, advice and support in this project. Thank you to them for all the long nights spent going through all my work and for teaching me the tricks of the trade not only in material science and nanotechnology but also in other aspects of my career.

I would also like to thank all the people who have helped me in the characterisation of my materials. Firstly, thank you to Dr Poslet Shumbula at Mintek who has been a great help with the TEM analysis, this could not be possible without the beautiful images he has taken. I would also like to express my gratitude to Dr Rudolph Erasmus for helping me with the Raman spectroscopy analysis of my materials. Special thanks to Dr Sibulelo Vilakazi for allowing me to use her instrumentation for the electrochemical characterisation of my materials. Thanks to the Wits MMU unit for providing the microscopic instrumentation and expertise necessary to get the best images possible.

I would also like to express my gratitude to all my colleagues who have helped me throughout the project. The CATOMAT and Moloto nanomaterials group for the opportunity to present my work to them and their valuable constructive criticism which has helped me grow as a researcher. Thanks to Dr Izaak Kotze for helping me with the NMR analysis. Special thanks to my partners in science Mr Ndivhuwo Shumbula and Siyabonga Nkabinde whose constructive criticism and input has kept me on my toes and forced me to do better.

Publications

1. Zakhele Ndala, Siziwe Gqoba, Nosipho Moloto, The effect of a co-surfactant to oleylamine in the colloidal synthesis of $MoSe_2$ nanomaterials. TO BE SUBMITTED

2. Zakhele Ndala, Siziwe Gqoba, Nosipho Moloto, Investigating the electrochemical properties of $MoSe_2$ few-layer nanosheets and nanoflowers for supercapacitor electrode applications. TO BE SUBMITTED

Presentations

1. Oral presentation at Catalysis Organometallics and materials (CATOMAT) seminar held at Chemistry department, University of the Witwatersrand on the 14/03/2016.
2. Oral presentation at Catalysis Organometallics and materials (CATOMAT) seminar held at Chemistry department, University of the Witwatersrand on the 16/07/2016.
3. Poster presentation SACI Inorganic Chemistry Conference 2017 (INORG2017) seminar held at Western Cape, South Africa 25 – 29/06/2017.
4. Oral presentation at Catalysis Organometallics and materials (CATOMAT) seminar held at Chemistry department, University of the Witwatersrand on the 19/07/2018.

Table of contents

List of figures

List of tables

List of schemes

List of Abbreviations

BET- Brunauer- Emmett-Teller

CdS- Cadmium sulphide

CdSe- Cadmium selenide

CV- Cyclic voltammetry

CVD- Chemical vapor deposition

DDT- 1-dodecannethiol

DOSY- Diffusion ordered spectroscopy

EDLC- Electric double layer capacitor

EES-Electrical energy storage systems

EIS- Electrical impedance spectroscopy

ESR- Equivalence series resistance

FTIR- Fourier transform infrared spectroscopy

GCD- Galvanostatic charge-discharge

HRTEM- High resolution transmission electron microscopy

MoS_2- Molybdenum disulfide

$MoSe_2$- Molydenum diselenide

NMP- N-methyl pyrrolidinone

NMR- Nuclear magnetic resonance

NOE- Nuclear Overhauser effect

OA- Oleic acid

OAm- Oleylamine

ODE- 1-octadacene

PbS- Lead sulphide

PXRD- Powder X-ray diffraction

SEM- Scanning electron microscopy

TEM- Transmission electron microscopy

TGA-Thermogravimetric analysis

TMDs- Transition metal dichalcogenides

TOP- Trioctylphosphine

TOPO- Trioctylphoshine oxide

Chapter 1: Introduction

1.1 Background

In recent years the need for inexpensive and reliable energy has been a topic of great interest considering the recent load shedding situation in South Africa, which was caused by the inability of the grid to cope with the high demand of electricity at a given time. This has put the energy discussion in the forefront as more of the public recognise the important role that continuous and reliable energy supply plays in the economic development of the country. Due to the increased concern on the effect of carbon emissions on the environment, the continual depletion of fossil fuels which remain the main source of energy and the use of renewable energy sources to tackle both issues. The topic of energy has taken centre stage in the global community as well. The increased demand of electricity will continue to put pressure on the electrical grid and many solutions have been put forward to alleviate some of that pressure one of which is the implementation of electrical energy storage (EES) systems. The implementation of these storage systems can contribute to ensuring a more reliable electrical grid and can also help to integrate renewable energy sources into the grid.[1] The greatest contribution from these systems would obviously be in load shifting which would allow for the storage of energy when demand is low, the energy would then be stored for use when the grid is under pressure.[2] There are three main energy storage classes which are power quality, bridging power and bulk energy management, Table 1 shows these three classes and their applications.[3] The application of the different technologies depends on their discharge times.

Table 1.1: The Three classes of energy with their discharge times and possible applications.

Name	Example of application	Discharge time required
Power Quality	Transient stability, Frequency regulation and UPS	Seconds to minutes
Bridging power	Contingency reserves, Ramping	Minutes to ~ 1 hr

Bulk energy management	Load shifting and capacity	Firm	Hours

These energy storage technologies range from lithium ion batteries to hydro power and compressed air systems, Fig.1.1 details the different technologies and in which energy storage class they could fit into.[4]

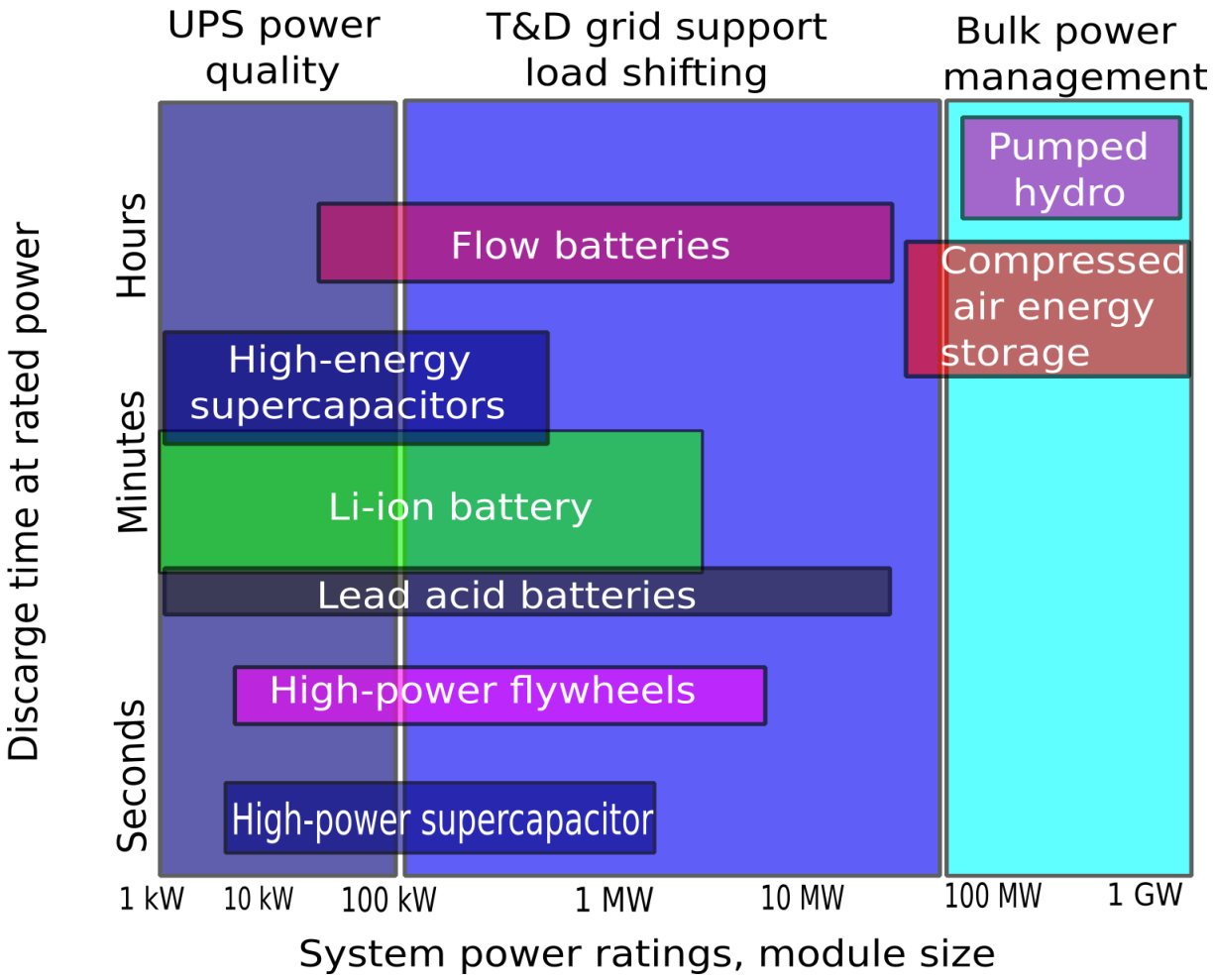

Figure 1.1: Diagram showing the different energy storage technologies and the energy class where they could be applied.

Supercapacitors have attracted a lot of interest in the energy storage sector as they have several advantages over batteries. The device architecture is identical to that of a conventional capacitor Fig. 1.2 with the major difference being the identity and nature of the electrode.[5]

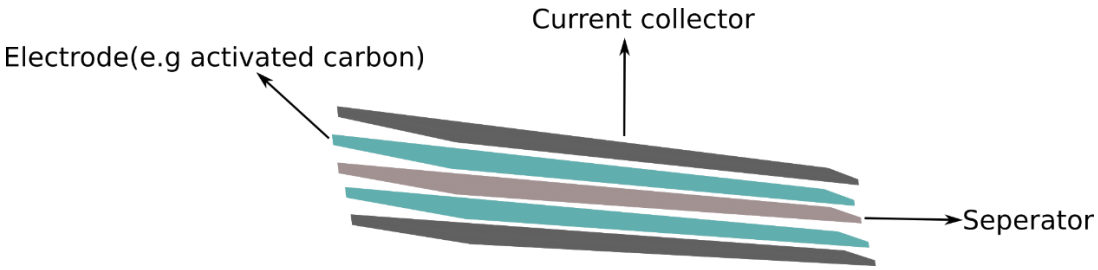

Figure 1.2: Device architecture of a supercapacitor.

They are suitable for applications that require fast discharge times so they are perfect for power quality applications in the electric grid as shown in Fig 1.1. The unique properties of supercapacitors such as their high-power density and capacitance, short charge-discharge times and long cycle life allow the devices the versatility to be applied to many applications.[6] Supercapacitors have been mostly applied in small applications such as in backup power (UPS),memory backup systems and portable devices but are advancing to the point where they are now being utilised for large scale applications such as in electrical and hybrid vehicles, high power energy applications and large-scale grid applications.[7-9] Table 2 shows how supercapacitors stack up against other energy storage technologies.[10]

Table 1.2: Comparison of the different energy storage technologies.

Storage technology	Energy density (Wh/kg)	Power density (W/kg)	Energy capital cost ($/kWh)	Power capital cost ($/kW)
Supercapacitor	0.5-5	1000-10000	500-15000	100-400
SMES	1-10	500-2000	1000-10000	200-500
Flywheel	10-50	500-4000	2000-5000	150-400
Li-ion	70-200	150-500	600-2500	1200-4000

The data indicates that supercapacitors have a much higher power density and the lowest power capital per cost but it also has the lowest energy density and the highest energy capital per cost compared to the other technologies especially batteries.[10] This energy density handicap limits the possible areas where supercapacitors can be applied, especially considering that the energy density for batteries is that much higher. This is currently a hot topic in supercapacitor research, to increase the energy

density of supercapacitors to be comparable to that of batteries. One way of achieving this goal is to introduce electrodes with a very high surface area to increase the energy density of the material. Activated carbon has been the most commonly used electrode for supercapacitors but there has been active and increased attention in exploring alternatives to this material. 2D materials such as graphene have been shown to be excellent materials for supercapacitor electrodes, another group of 2D materials that have been identified as potential candidates for supercapacitor electrodes are transition metal dichalcogenides (TMDs).[11] TMDs are vertically stacked layered semiconductor materials, with the layers weakly held together by van der Waals forces.TMDs like MoS_2 and $MoSe_2$ have received increased attention for use as supercapacitor electrodes because of their unique properties such as their high surface area, high carrier mobility and redox active structures.[5-13] A significant amount of work has been done with MoS_2 whilst $MoSe_2$ has been largely ignored. This project focuses on the colloidal synthesis of $MoSe_2$ nanomaterials for supercapacitor electrode applications. A comparison of the properties of MoS_2 and $MoSe_2$ suggests that $MoSe_2$ could be a more suitable material for supercapacitors than MoS_2. $MoSe_2$ has been noted as having a more metallic character than MoS_2 due to the higher metallic character of Se compared to S, this property along with the higher interplanar spacing of the layers which would allow ions to intercalate into the layers therefore resulting the storage of more energy makes $MoSe_2$ a better candidate for supercapacitors than MoS_2.

1.2 Problem statement

TMDs and their nanocomposites have been investigated as electrodes for supercapacitors with favourable results but if these materials are to be used in commercial supercapacitors they must be produced in large batches. TMDs are currently produced using exfoliation methods namely mechanical and liquid exfoliation. The challenge encountered when using both mechanical and liquid exfoliation is that the methods are difficult to scale-up and are thus not suitable for large scale production of TMDs.[14] Mechanical exfoliation methods have so far only been used in lab scale for research purposes. Liquid exfoliation has thus far been the most promising of the exfoliation methods. Liquid exfoliation using lithium intercalation has been the more popular synthetic approach as it can produce large amounts of the materials.[15]Lithium intercalation could be used to circumvent the problem encountered

with liquid exfoliation methods but unfortunately when using Li intercalation the Li^+ ions are physisorbed on the nanosheets which deteriorates their electrical and thermal properties.[15] Chemical vapor deposition (CVD) has proven to be an excellent technique for synthesis of the molybdenum dichalcogenide nanosheets as it can produce good quality nanosheets and the thickness of the material can be controlled, CVD also has the added advantage that it can be scaled up.[16-17] Unfortunately, CVD involves the use of very high temperatures and is not a simple synthetic procedure. Alternative synthetic methods such as chemical solution synthetic methods are now being explored to address the difficulties experienced when the above-mentioned methods are employed. The Colloidal synthetic method that has been widely used for the synthesis of semiconductor nanomaterials is one of the methods that are currently being explored. The colloidal method has been used previously to synthesize various semiconductor nanomaterials including layered materials.[18] The colloidal method is an appealing choice for the synthesis of the nanomaterials as it deals with some of the disadvantages of the synthetic procedures previously mentioned and adds on many advantages as well. The method is fit for the large-scale production of crystalline and monodisperse nanostructures, the method has the added advantages of being highly reliable, cost effective and energy efficient.[19] The most enticing feature of the colloidal synthetic method is the ability to control aspects of the synthesized products such as the size and shape of the nanomaterials.[20] This control is achieved by altering some of the reaction parameters such as temperature, precursor selection and capping agent.

1.3 Aim and objectives of the study

This work focuses on the colloidal synthesis of $MoSe_2$ nanomaterials with various morphologies and to determine which morphology of the nanomaterials would be best suited for use as an electrode material in supercapacitors.

To achieve the above-mentioned aim, the following objectives were identified.

- Synthesis of the $MoSe_2$ nanomaterials using colloidal synthesis.
- The characterization of the synthesized nanomaterials using techniques such as PXRD, Raman spectroscopy, UV-Vis absorption spectroscopy, TEM, SEM among others.

- Investigate the effect the various reaction parameters such as reaction time, choice of precursor and surfactants on the structural, morphological and optical properties of the nanomaterials.
- Electrochemical characterization of the $MoSe_2$ nanomaterials using cyclic voltammetry, galvanostatic charge-discharge and impedance spectroscopy to assess the suitability of the nanomaterials for use as electrodes in supercapacitors.
- To investigate the effect of the morphology of the $MoSe_2$ nanomaterials on the electrochemical properties of the nanomaterials.

Chapter 2: Literature review

2.1 Transition metal dichalcogenides

$MoSe_2$ belongs to a family of materials called transition metal dichalcogenides which are layered materials much like graphite. They have the general formula MX_2 where M is a transition metal (M = Mo, W, Nb, Ti, Ta, Re) and X is a chalcogen (X= S, Se, Te). TMDs include layered materials such as MoS_2, WSe_2 and $NbSe_2$. Bulk TMDs have very diverse properties; $MoSe_2$ and WSe_2 exhibit semiconductor properties, HfS_2 behaves like an insulator and VSe_2 is a semi-metal.[21-23] $NbSe_2$ and TaS_2 can even exhibit low temperature phenomena such as superconductivity. Very much like graphite these materials can be exfoliated to obtain 2D atomic crystals of the materials. These 2D atomic crystals exhibit interesting properties due to quantum confinement effects.[24-25]

2.1.1 Structure and properties of $MoSe_2$

$MoSe_2$ is composed of atomically thin layers that are comprised of a layer of molybdenum atoms arranged in graphite like hexagonal structure sandwiched between two layers of selenium atoms.The Mo is bonded to the Se in a trigonal prismatic co-ordination.[26] The intra-layer Mo-Se bonds are covalent bonds while the layers themselves are held together by weak van der Waals forces, the distance between the layers is ~ 6.5 Å. A representation of the structure of $MoSe_2$ is shown in Fig. 2.1.[26]

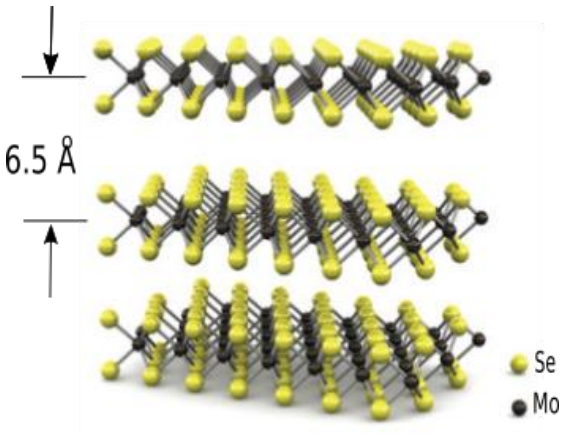

Figure 2.1: Crystal structure of bulk $MoSe_2$.[27]

The Mo adopts a +4 oxidation state and the Se has an oxidation state of -2. The transition metal is covalently bonded to six Se atoms and the Se is bonded to three metal atoms. The length of the Mo-Mo bonds ranges between ~ 3.15 Å and 4.03 Å.[27] The co-ordination of the Mo in the $MoSe_2$ can either be octahedral or trigonal prismatic as shown in Fig. 2.2.

Figure 2.2: Co-ordination of the Mo to the Se in $MoSe_2$ crystal structure.[27]

The different bonding of the Mo atoms to the Se gives rise to two different phases of $MoSe_2$. The trigonal prismatic (D_{3h}) is called the 2H, and the octahedral (O_h) phase is called 1T.[27] The 2H phase is a semiconducting material while the 1T is metallic. The metallic 1T phase would obviously be more preferred for most applications because of its larger electrical conductivity but unfortunately the phase is known to be thermodynamically unstable and converts to the 2H phase.[28] The pioneering work on graphene proved that the single layer allotrope of carbon exhibits exotic and exciting properties compared to its bulk multilayer counterpart graphite. This phenomenon has been proven to extend to a host of other layered materials. Single to few layer nanomaterials of $MoSe_2$ have been identified to have interesting properties that are not observed in the bulk counterpart. The most interesting property of TMDs such as MoS_2, WS_2 and $MoSe_2$ is that they show a switch from an indirect to a direct band-gap when they move from a bulk material to mono or few-layer nanomaterials.[29]The electron band structures of various TMDs showing transformation from indirect to direct band-gap is shown in Fig. 2.3.

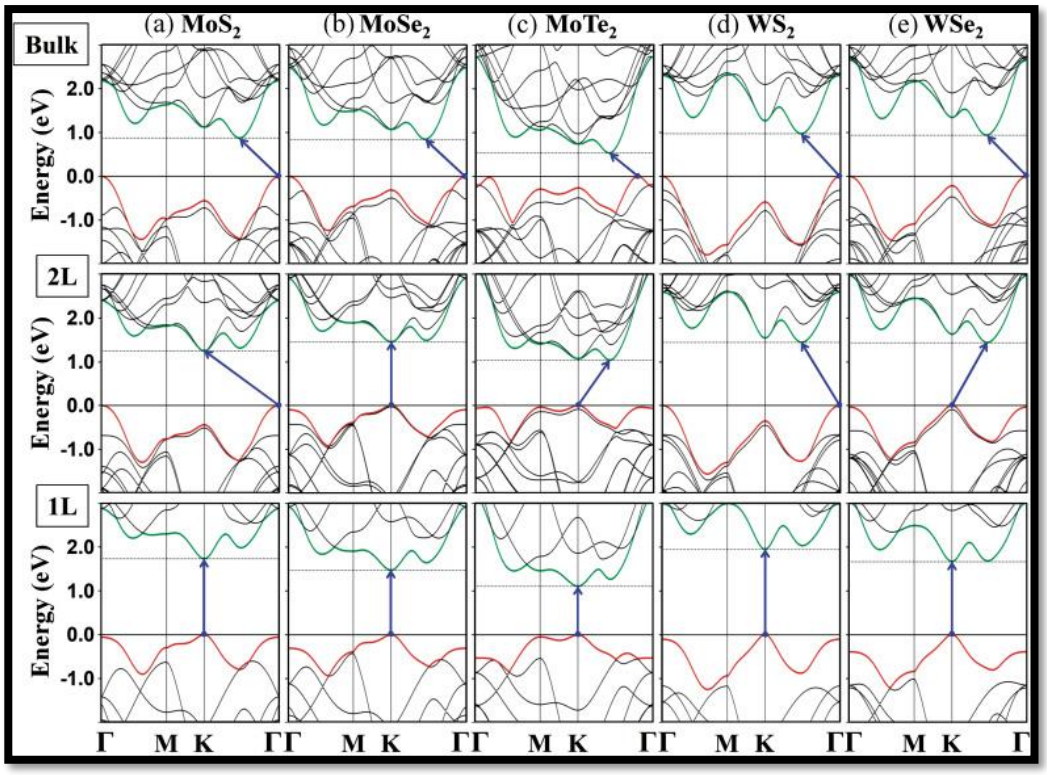

Figure 2.3: Band structures of (a) MoS_2, (b) $MoSe_2$, (c) $MoTe_2$, (d) WS_2, and (e) WSe_2 from the bulk (upper panels) to double-layer (2L, middle panels) and single-layer (1L, bottom panels). The horizontal solid lines in each panel indicate the VBM and the dotted lines indicate the CBM. The solid blue arrows indicate the lowest energy transitions.[29]

This is due to a change in the optical band structure of the material when the change is made to a monolayer and to bi-layer for $MoSe_2$. $MoSe_2$ has an indirect band-gap of 1.09 eV in the bulk and a direct band-gap of 1.55 eV in mono to few-layers.[30]The UV-Vis absorption spectrum of the material has been shown to have two exciton peaks. These exciton peaks are due to a direct electron transition at the K-point.There are two exciton peaks for the single band-gap transition because of the splitting of the valence band at the K-point which is due to spin orbital coupling and inter-layer interaction.[31]The optical properties of TMDs differ from one another, for instance the band-gap of monolayer MoS_2 is lager at 1.9 eV compared to that of monolayer $MoSe_2$ at 1.5 eV.[31] It has also been found that the $MoSe_2$ few-layer nanosheets have a degenerate direct and indirect band-gap whereas the indirect and direct band-gaps in MoS_2 are well separated and far from degenerate.[32] Researchers have also discovered other subtle differences between $MoSe_2$ and MoS_2 that could

make $MoSe_2$ a much more suitable for materials for certain application compared to MoS_2. $MoSe_2$ has various advantages over MoS_2 that make it a more suitable candidate for use as materials for supercapacitor electrodes. $MoSe_2$ has a higher intrinsic electrical conductivity than MoS_2 because Se is a more metallic atom than S.[33] $MoSe_2$ also has a larger interlayer spacing (0.645 nm) than MoS_2 (0.615 nm) which $MoSe_2$ it could store more charge than MoS_2, therefore $MoSe_2$ could be more suitable for applications in devices such as Li-ion batteries and supercapacitors.[33]

2.2 Colloidal synthesis

Colloidal synthesis techniques entail the formation of colloids which are nanocrystals or crystalline nanoclusters that are made up of a few hundred or a few thousand atoms. The atoms agglomerate together to form the colloids that are dispersed in some solvent.[34] There are physical and chemical approaches to nanoparticle synthesis. Physical approaches are “top-down” processes that break down bulk material into nanocrystalline materials as shown in Fig. 2.4. Colloidal synthesis is essentially a “bottom-up” synthetic procedure which means the nanocrystals are built from the bottom up “atom by atom” or “molecule by molecule” to form the nanocrystal.[34]

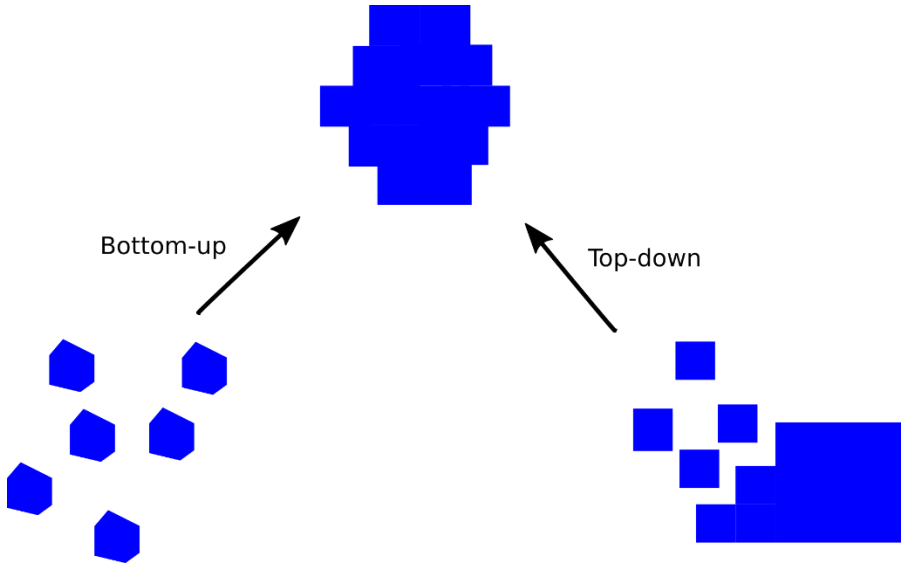

Figure 2.4: The bottom-up and top-down approaches to nanocrystal synthesis.

Colloidal synthesis relies on chemical techniques such as chemical reduction, thermal decomposition or sol-gel synthesis to produce the atoms needed from various precursors. The thermal decomposition approach utilizes organometallic precursors that are decomposed in an organic solvent at elevated temperatures. Chestoney *et al.*

was able synthesize crystalline and stable group II-VI semiconductor nanomaterials using the colloidal method in 1998, unfortunately the nanomaterials synthesized were not monodisperse.[36] The colloidal method was adapted from the work done by Chestoney *et al.* to allow for the synthesis of monodisperse semiconductor nanoparticles.[37] The synthesis procedure developed by Bawendi *et al.* was coined the "hot-injection" method. The hot-injection method has been used for the synthesis of various semiconductor nanomaterials including TMDs.[37-39] There are several other methods that are variants of the hot-injection method that have also been used for semiconductor nanomaterials. The theory behind the formation of the nanocrystals through colloidal synthesis is still to be fully understood. The theoretical principle of the nanocrystal nucleation is based on the work by Becker *et al.* which was done in the 1930's and the nucleation of metal and semiconductor nanocrystals can best be explained by the work of LaMer and Dinger in the 1950's.[40-41] The theoretical work on nucleation and growth is still being disputed by a number of researchers in the scientific community but the methods are still used to explain the nucleation and growth of nanocrystalline materials.

2.2.1 Nucleation and growth

The process of nucleation is the first step in a first order phase transition. It is the process whereby a small number of ions, atoms or molecules coalesce from liquid or gas phase to form a site which is the nucleus where other particles can agglomerate to form a crystal. The classical nucleation theory(CNT) is a theoretical model that describes the nucleation process. It describes the nucleation process as a thermodynamic system that seeks to minimize the Gibbs free energy in the formation of the nucleus.[42] This theory was first developed by Becker *et al.* using work done by Gibbs.[43] Homogenous nucleation describes the spontaneous formation of a nucleus from a supercritical state called supersaturation. The Gibbs free energy of a nucleus is expressed as the sum of a positive and negative term, the negative term expresses a bonding between two monomers or a monomer and a cluster that leads to a lowering of the Gibbs free energy and the positive term expresses unfavorable bonding that would lead to an increase in the Gibbs free energy. The Gibbs free energy(ΔG) of a spherical cluster is expressed as:

$$\Delta G = -\frac{4}{3}\pi r^3 |G_v| + 4\pi r\gamma \qquad (2.1)$$

Where r is the radius, γ is the surface energy per unit area and $|\Delta G_v|$ is the difference in the Gibbs bulk free energy per unit volume. A plot of the Gibbs free energy with respect to the radius in Fig. 2.5 shows the effect of the surface energy on the positive term and the effect of the bulk free Gibbs energy on the negative term.[42]

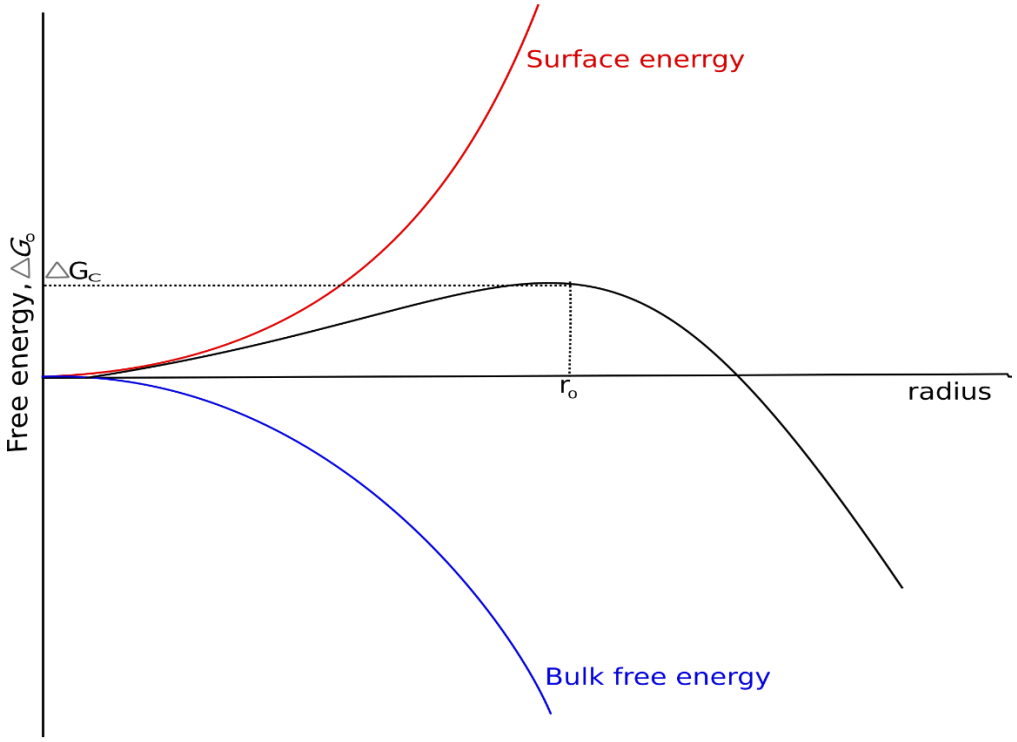

Figure 2.5: A plot of the Gibbs free energy against the radius of the clusters.

The figure also shows there is a maximum Gibbs energy at a critical cluster radius r_c, this is the radius at which the cluster of particles become stable which corresponds to the nucleus. When the radius of the cluster is < r_c the cluster is unstable and dissolves into solution, the clusters with radius > r_c are stable and growth is favorable. One can solve for r_c by dΔG/dr = 0 which gives

$$r_c = \frac{2\gamma}{|\Delta G_v|} \tag{2.2}$$

Substituting (2) into equation (1) gives:

$$\Delta G = \frac{16\pi\gamma^3}{|\Delta Gc|^2} \tag{2.3}$$

The nucleation rate can be expressed using the Arrhenius equation where the energy barrier to nucleation is the activation energy; nucleation must then be a statistical process where $J(\Delta G_c, T)$ is the nucleation rate.

$$J(\Delta G_c, T) = A\ exp(\frac{-\Delta G_c}{K_b T}) \tag{2.4}$$

LaMer nucleation theory

LaMer *et al.* developed a theory to explain nucleation in nanoparticle synthesis. They suggest a homogeneous nucleation where there is a burst of nucleation after supersaturation that leads to the formation of many nuclei with the same size.[41] The subsequent growth of the nuclei occurs without the formation of new nuclei. The process can be described in three stages as depicted in Fig. 2.6: (i) The increase of monomer concentration in solution due to the decomposition of precursor, the concentration of monomer increases until the solution reaches critical supersaturation of monomer concentration (C_s); (ii) The saturation will increase until it reaches a level C_{min}, at this point the energy barrier for nucleation is overcome which leads to rapid nucleation (burst nucleation); (iii) Burst nucleation leads to a drastic drop in monomer concentration which results in a drop in the supersaturation level, the nucleation process then stops.

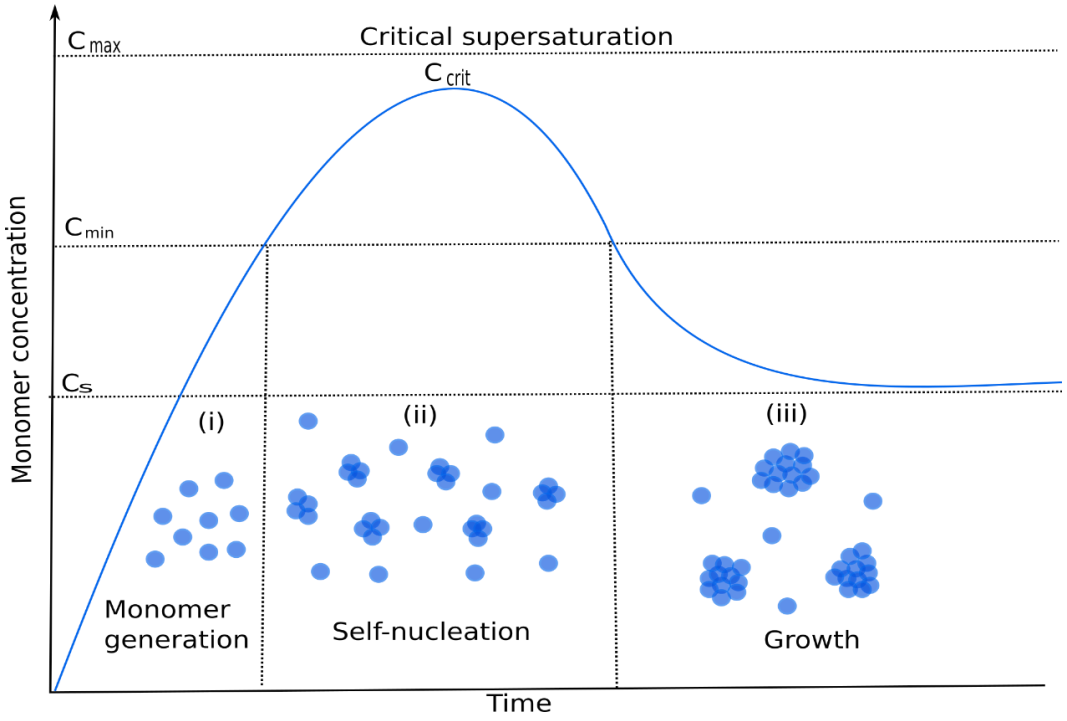

Figure 2.6: A graphical representation of the LaMer and Dinegar nucleation.

The nuclei then begin to grow due to the diffusion of monomer to the nucleation site. LaMer and Dinger's description can explain how monodisperse colloidal solutions form. The theory is unable to explain instances where there is broad distribution of nanoparticle sizes.

Growth of nanoparticles in the colloidal synthetic procedure

The growth of the nanoparticles in colloidal synthesis can be explained using Ostwald ripening.[44] The growth mechanisms can explain the formation of nanoparticles with a broad size distribution.[44] The process describes a heterogeneous growth process whereby small crystals dissolve and redeposit into larger particles. This phenomenon is caused by the thermodynamic instability of small particles compared to larger particles, since the particles at the surface are a lot less stable then the particles at the interior of the crystal. Smaller particles have a lot more particles exposed at the surface and are therefore less stable than larger particles. The molecules in small particles will detach from the particles and diffuse in the solution until they attach to the larger particles. The number of smaller particles will continue to decrease and the number of larger particles will increase. This will lead to an increase of the average size of the particles. Ostwald ripening is an undesirable phenomenon when one attempts to synthesize small particle size nanoparticles that are monodisperse. Therefore, the burst nucleation step is crucial in colloidal synthesis.

2.2.2 Anisotropic growth of two-dimensional nanocrystal and the TMDs

The surface energy of the exposed crystallographic facets plays a vital role in determining the shape of the nanocrystal formed after nucleation. This is due to the fact that the growth of the nanocrystal whether it be isotropic or anisotropic is determined by the surface energy of the expressed facets. In an isotropic phase where the energy of the expressed facets is the same; the shape of the nanocrystal will be a sphere, but for nanocrystal with facets that have different energies the shape may be more complex. The Wulf construction which was developed by George Wulf is a well-established method of determining the equilibrium shape of the crystal.[45] This theorem shows that certain planes are preferred over others due to their lower surface energy and surface area and these facets determine the shape of the crystal. The Wulf construction can normally be used to predict the shape of a nanocrystal by determining its thermodynamic equilibrium state but there are several examples where nanocrystal have assumed shapes that were not the most thermodynamically favourable shape. There are several synthesis parameters that force nanocrystals to form in thermodynamically non favourable shapes such as 2D structures. One of the factors that influence the anisotropic growth of nanocrystals is defects. Defect induced anisotropy is one of the major causes of two-dimensional anisotropic growth; one

example is twin plane defects in metal nanoparticles that causes the formation of metal nanoprisms and nanoplates.[46] Kinetic effects can also determine the shape of the nanocrystals. The shapes of the particles can be heavily dependent on the growth rates of the nanoparticles. If the growth rate of the nanocrystal is high the rapid addition of precursor does not favour any facets and high energy facets can grow to determine the shape of the nanocrystal. When the growth rate is slow the high energy facets tend to grow faster.[47] This effect of the growth rate is partly dependent on the nature of the precursor utilised to be more specific it depends on the reactivity of the precursor used. One other important parameter is the temperature of the growth reaction, the temperature can affect the kinetics of the nanocrystal growth and it also acts on the formation of the ligand assemblies which are another important shape control parameter. The influence organic ligands have been researched extensively in the synthesis of inorganic nanocrystals. This extends to the anisotropic growth of nanocrystals to form two dimensional nanomaterials.[48] In the case of transition metal dichalcogenides however which are naturally layered materials the shape of the material is governed by the Wulf construction. The challenge in the colloidal synthesis of these materials is the control the thickness and lateral dimensions of the synthesized nanomaterials.[49]

2.2.3 The effect of precursor on colloidal synthesis

The selection of suitable precursor for colloidal synthesis is one of the most important parameters to consider when designing a synthetic method. Colloidal synthesis relies on the formation of free monomer for nucleation and growth of nanoparticles to occur. How quickly that monomer is made available and how quickly that monomer will react to begin the nucleation process influences the size and shape of the nanomaterials synthesized.[50] The precursor must undergo a chemical process that will allow for the release of free monomer into the reaction solution. Decomposition is one of the processes used to break down precursors to release the required monomer. The Precursor is normally a complex consisting of a metal that is bound to ligand. The monomer required in this case is normally the metal. This can also be extended to organic molecules where the monomer is the chalcogen atom in the organic molecule. The reactivity of the monomer is determined by how strongly the ligands bind to the monomer. The process at which the precursor (P) decomposes to form free monomer (M) where the formation rate of this process is k_f can be expressed as:

$$P \xrightarrow{K_f} M \tag{2.5}$$

In this process, we can assume that the formation of monomer is a first order reaction. The reaction constant will then depend on the temperature and activation energy which will allow us to express it as:

$$\frac{d[M]}{dt} = -\frac{d[P]}{dt} = Aexp\{\frac{-E_a}{RT_v}\}[P] \tag{2.6}$$

Where A is the prefactor, T_v is the temperature of the reaction solution at any given time and E_A is the activation energy. The formation of monomer will the depend on the temperature of the reaction solution and the activation energy which is related the binding energy of the ligands to the monomer. Then depending on the E_A the reactivity of any given monomer will be characterized as low reactivity (high E_A), moderate (medium E_A) and high reactivity (low E_A). Embden and co-workers have simulated scenarios where one has a low, moderate and high reactivity monomer and the results were as follows: High reactivity monomer, the binding energy of the ligands and the monomer is low so the dissociation of the monomer from the ligands can occur rapidly at low or room temperature.[50] This rapid formation of monomer results in high nucleation and growth rates. The formation of nuclei happens quickly and the nuclei begin to absorb monomer rapidly resulting in the quenching of further nucleation. This leads to low yield of the nanoparticles and the particles have broad particle size distribution.

When utilizing a moderately reactive monomer, the binding energy of the ligands is slightly lower than the high reactivity monomer. The dissociation of the monomer from the ligands is achieved when the temperature slightly elevated, when the required temperature is reached nucleation is triggered. The formation of monomer occurs quickly for a brief period, this is then followed by subsequent growth. The rates of nucleation and growth are balanced which leads to a good nanoparticle yield with narrow particle size distribution. Low reactivity monomer, the rate of dissociation of the monomer from the ligands occurs slowly at relatively high temperatures. The gradual release of monomer results in the slow formation of nuclei in a longer period, nuclei of small and large sizes occur. This leads to Ostwald ripening where the smaller particles dissolve and the larger particles absorb the monomer released from the smaller particles. The larger particles continue to absorb monomer. The decrease of the monomer concentration results in an increase of the critical size, this prevents the

formation of new nuclei. The remaining monomer is further absorbed by the larger particles. This process leads to a low yield of nanoparticles with a very broad size distribution. These observations show the relationship between the reactivity of the monomer and the properties of the nanoparticles formed, this highlights the importance of choosing the right precursor in colloidal synthesis.

2.2.4 The role of the capping agent in colloidal synthesis

In colloidal synthesis, the reactions are normally conducted in organic solvents which can also act as capping agents that bind to the surface of the nanoparticles to stabilize the nanoparticles, to prevent the nanoparticles from aggregating to form larger clusters and to protect the surface from oxidation.[51] The added advantage of using organic solvents is the ability to reach high reaction temperatures, the expanded temperature range allows for access to synthesize nanomaterials inaccessible using an aqueous solvent. The capping agents can also be used to control the size and shape of the nanoparticles synthesized.[52] There are different binding mechanisms that allow for the binding of the capping agent which could be chemisorption, electrostatic interaction or hydrophobic interaction.

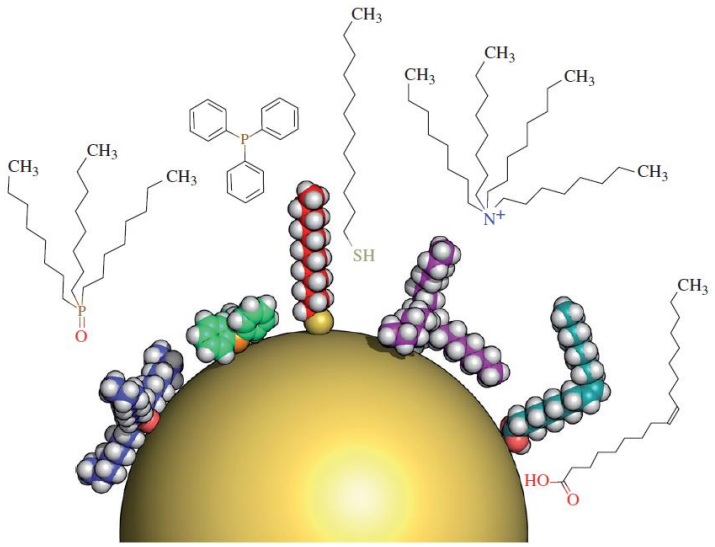

Figure 2.7: The binding of various capping agents with different head groups on the surface a nanoparticle. The ligands are adsorbed on the surface of the spherical particle, the ligands structures and their space-filled models are depicted. Left to right: trioctylphosphine oxide (TOPO), triphenylphosphine, dodecanethiol(DDT), tetraoctylammonium bromide (TOAB) and oleic acid (OA).[51]

The interaction is normally achieved using the head group of the large organic molecule. The identity of the head group is essential because different functional groups have different affinities to certain crystal facets. One example is the affinity of thiol functional groups to gold nanoparticles. In colloidal synthesis, the organic solvents or ligands used have a head group that has an electron donating group such as an amine, hydroxy, phosphine or a thiol Fig. 2.7. The ligands are in a dynamic process of binding and unbinding on the surface of the nanoparticles.[53] The ligands can then be removed by excessive washing or they might be replaced by a ligand with greater affinity to the surface of the nanoparticles. Capping agents are also able to control to control the reactivity of monomer species by binding to them. The preferential binding of the heads groups of capping agents to certain crystal facets of the nanoparticles can be used to control the morphology of the synthesized nanomaterials.[54] These surfactants have also been used to induce anisotropic growth to form 2D atomic crystals. Soft colloidal templating synthesis can be used to produce 2D atomic crystals, surfactants like oleyl amine or oleyl alcohol can be used to direct the crystal growth.[55] Hyeon *et al.* demonstrated this by synthesizing stacked CdSe nanosheets by first forming a lamellar shaped complex using $CdCl_2$ and oleyl alcohol or oleyl amine, this template is then reacted with a selenium source to form the CdSe nanosheets.[56] The TMDs are different because they will naturally self-assemble in colloidal synthesis to form nanosheets. The struggle then is finding a way to use the surfactants to control the thickness and the lateral dimensions of the synthesized nanosheets.[49] In 2D atomic crystals one could ideally control both the lateral dimensions of the crystal and the number of layers by choosing the right capping agent. Jung *et al.* have investigated the effect of use of different capping agents in the synthesis of WSe_2 and $MoSe_2$ nanomaterials.[57] They found that the use of amine ligands allows for control of the lateral dimensions of the $MoSe_2$ nanosheets as the amine ligand preferentially bind to the edge sites and inhibits lateral growth. The use of ligands such as oleyl alcohol which contain hydroxyl groups are able to preferentially bind to the basal plane of the nanosheets which inhibits vertical growth leading to the formation of monolayer nanomaterials. Interestingly enough Guo *et al.* have investigated the effect of oleylamine (OAm) and oleic acid (OA).[58] The group synthesized the nanomaterial using OAm only, OA only and a 1:1 mixture of OA and OAm. They found out that the use of oleylamine resulted in ultrathin nanosheets that

were superimposed to form a nanonetwork. The use of oleic acid on the other hand resulted in the formation of a nanoflower like morphology. These results contradict the results reported by Jung *et al*. The use of a capping agent with a hydroxyl group may not be a sure way obtaining monolayer nanosheets. There are other factors that obviously need to be considered, these factors will be investigated in this project. The use of monolayer $MoSe_2$ nanomaterials would not be ideal for use as supercapacitor electrodes, few-layer nanomaterials will be more suited as the electrolyte ions will be able to intercalate in between the layers resulting in the storage of more charge.

2.3 Introduction to supercapacitors

2.3.1 What are supercapacitors?

Supercapacitors are energy storage devices that work in a similar way to conventional capacitors except they use electrodes with a high surface area and thinner dielectric materials to achieve a higher capacitance.[59] These modifications in the supercapacitors give the devices greater energy densities than a conventional capacitor and greater power densities than those found in batteries.

Background in the workings of a supercapacitor

The make-up of a conventional capacitor consists of two electrodes separated by an insulating dielectric material. When a voltage is applied to a capacitor opposite charges begin to accumulate on the surface of the two electrodes, the charges are kept separate by the insulating dielectric material. The separation of the charges by the dielectric creates an electric field that allows a capacitor to store energy.[60] The capacitance is then defined as the ratio of the stored charge over the voltage applied on the capacitor. The capacitance C of a capacitor is directly proportional to the surface area A of the two electrodes and is inversely proportional to the distance D between the electrodes:

$$C = \varepsilon_r \varepsilon_o \frac{A}{D} \tag{2.7}$$

Where ε_o is the permittivity of free space and ε_r is the dielectric constant of the insulating dielectric material between the two electrodes.

The energy and power density are two important attributes of the capacitor. The energy density is the energy stored in the capacitor per unit of volume:

$$E = \frac{1}{2}CV^2 \quad (2.8)$$

The maximum power of a capacitor is directly proportional to the applied voltage and is inversely proportional to the ESR which is the equivalent series resistance:

$$P_{max}\frac{V^2}{4 \times ESR} \quad (2.9)$$

The ESR is the resistance contribution of the internal components of the capacitor (e.g current collectors, electrodes and the dielectric material). Conventional capacitors have high power densities and lower energy densities compared to batteries.[61] This means they can store a lot less energy per unit mass or volume than a battery but it can deliver the energy it has stored a lot faster than a battery. The supercapacitors operate on the same basic principles that govern a conventional capacitor but as previously mentioned make use of high surface area electrodes and thin dielectric material to decrease the distance between the electrodes. This is what leads to the high capacitance in supercapacitors compared to the conventional capacitor and therefore higher energy densities. Supercapacitors have low ESR contributions so the power densities are also higher than that of conventional capacitor.

2.3.2 The classes of supercapacitors

The three classes of supercapacitors are electrochemical double layers supercapacitors, pseudocapacitors and hybrid supercapacitors. The differences between the three classes are the mechanisms that are used for storage, the mechanisms are faradaic, non-faradaic and a combination of the two.[62] Pseudocapacitors use faradaic processes which involve oxidation-reductions reactions where the charge is transferred between the electrode and the electrolyte. The electrochemical double layer supercapacitors use non-faradaic processes which involve the distribution of the charges on the surface of the electrodes by physical processes that do not involve the breaking and forming of bonds.[63] There are various types of hybrid capacitors from asymmetric pseudo/EDLC, Composite and rechargeable battery types.[64]

Electrochemical double layer supercapacitors (EDLC)

Electrochemical double layer supercapacitors use non-faradic methods for the storage of charge. When a voltage is applied to the supercapacitor charge begins to accumulate at the surface of the electrodes. The ions in the electrolyte begin to move

to the electrode of opposite charge. An electric double layer forms between the charge on the surface of the electrode and the charges on the electrolyte.[65]

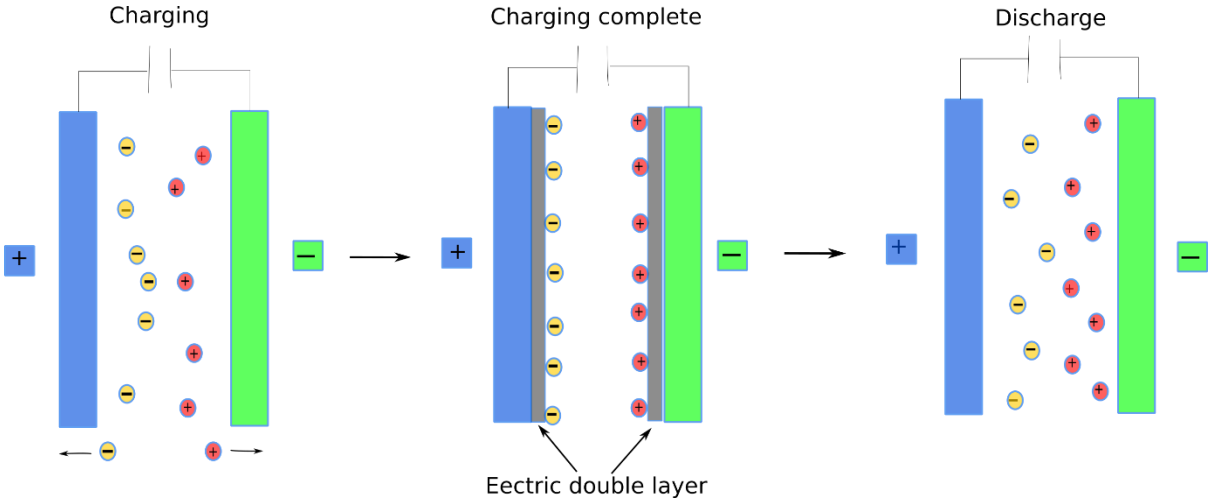

Scheme 2.1: The charging and discharging processes in an electric double layer supercapacitor.

The use of large surface area electrodes and the formation of the electric double layer allows for enhanced storage capabilities. Traditionally activated carbon is the material used as electrodes in EDLCs but the electrodes have also been made using carbon nanotube arrays.[66] Activated carbon is used as an electrode for EDLCs because it is a porous material with a large surface area. The material has a combination of micro, meso and macro pores, work on the material has revealed that large pores result in high power densities and smaller pores lead to high power densities.Carbon nanotubes have been an even more successful material for supercacapcitor applications. The carbon nanotubes are grown in such a way that they form an interconnected network of mesopores that allows for the use of nearly all the area available.[67] The use of these carbon nanotube networks yields improved capacitative behavior than activated carbon. Various other materials are now being investigated for possible use in supercapacitors such as TMDs.

Pseudocapacitors

Pseudocapacitors are able to store energy by utilizing storage mechanism that use redox or faradaic charge transfer reactions that occur at or near the surface of an electrode as it comes into contact with the electrolyte. There are three different mechanisms that give rise to pseudocapacitance namely redox pseudocapacitance,

underpotential deposition and intercalation pseudocapacitance.[68] Redox pseudocapacitance arises due to redox reactions that occur at or near the electrode surface when electrolyte ions adsorb on the surface of the electrode, the redox reactions result in faradaic charge transfer between the electrode and electrolyte ions.[69] Underpotential deposition is brought about by the deposition by adsorption of a monolayer of metal ions on another metal with a higher redox potential.[70] Intercalation pseudocapacitance occurs when ions intercalate into the layers or tunnels of a redox active material which gives rise to a faradaic charge transfer Fig. 2.8.[71]

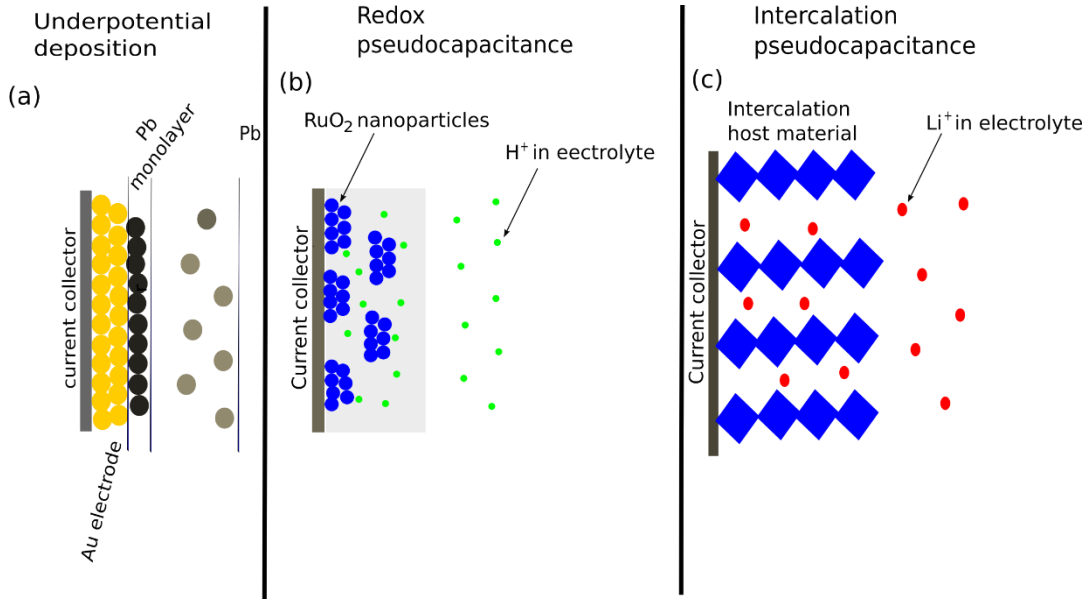

Figure 2.8. The different pseudocapacitance mechanisms: (a) Underpotential deposition, (b) redox pseudocapacitance and (c) intercalation pseudocapacitance.

The three different mechanisms differ only in the physical processes and the materials that are used to invoke them. The mechanism are connected by the fact the processes are brought about by faradaic charge transfer processes at the interface between the electrode and electrolyte interface. The capacitance in a pseudocapacitor is determined by the equation:

$$C = \left(\frac{nF}{m}\right)\frac{X}{E} \tag{2.10}$$

Where n is the number of electrons, F is the faraday constant, m is the mass of active electrode material, E is the potential and X is the fractional coverage of the active electrode material surface or inner structure. A plot of E vs X is not linear as one would

expect in a traditional capacitor so that capacitance is not always constant, this is why phenomenon is known as pseudocapacitance.[68] An example of underpotential deposition is the deposition of a lead monolayer on a gold electrode Fig.6 (a).[72] Intercalation pseudocapacitance has been observed in materials such as orthorhombic T-Nb_2O_5, the pseudocapacitance is achieved by insertion of Li atoms in the matrix of the layered structure in a non-aqueous electrolytes fig 6(b).[73] The redox couple of Nb which id +5/+6 allows the materials to hold up to 2 Li^+ per molecule Nb_2O_5. The prime example of redox pseudocapacitance is that observed in RuO_2 which was the first observation of pseudocapacitance in any material.[74] RuO_2 can absorb hydrogen protons(H^+) which is accompanied by the transfer of an electron. It was also discovered that the use of hydrated RuO_2 improved that capacity of the materials which alluded to the importance of structural water.[75] Accompanied by use of nanostructured porous architecture of the material the capacity can be significantly increased.[75] The storage mechanism is expressed as:

$$RuO_x(OH)_y + \delta H^+ + \delta e^- \leftrightarrow RuO_{x-\delta}(OH)_{y-\delta} \quad (2.11)$$

The conductivity of RuO_2 and its high outer surface area also helps to improve capacity by allowing for fast electron transfer and the high outer surface area reduces diffusion distances.

2.3.3 MoS_2 and $MoSe_2$ as supercapacitor electrodes

MoS_2 has been the most investigated out of the different TMDs. Although more attention has now been directed to $MoSe_2$ nanomaterials. There is controversy in whether these materials show electric double layer supercapacitance or pseudocapacitance. Swapnil *et al.* observed EDLC and pseudocapacitance in their electrochemical studies of MoS_2 synthesized using chemical bath deposition.[76] The group observed that the material displayed different storage mechanisms when different electrolytes where used.[76] The pseudocapacitance was only observed when strong basic electrolytes such as NaOH and KOH were used but electric double layer supercapacitance was observed in electrolytes such as $NaSO_4$. The proposed mechanism for the double layer capacitance in $NaSO_4$ and K_2SO_4 was (Eq 2.12):

$$(MoS_2)_{surface} + C^+ (Na^+ \text{ or } K^+) + e^- \leftrightarrow (MoS_2\text{-}C^+)_{surface} \quad (2.12)$$

The proposed mechanism (Eq 13) for the pseudocapacitance mechanism in NaOH and KOH is defined as follows:

$$MoS_2 + C^+ + e^- \leftrightarrow MoS - SC^+ \quad (2.13)$$

The pseudocapacitance is observed partly due to the insertion of the cations into the layers of the material. The group continued to evaluate the performance of the MoS_2 electrodes using $NaSO_4$ as the electrolyte, the specific capacitance of the electrode was determined to be 576 Fg^{-1} and the energy density was found to be 14.58 $Whkg^{-1}$. The electrode also displayed good capacitance retention with the capacitance being 82% at 3000 cycles. Work done by Chhowalla *et al.* brought into focus the use of the 1T phase of MoS_2 which is metallic and has a higher electrical conductivity than the 2H phase of the material.[77] The study also confirms a pseudocapacitative behavior of the material. The electrochemical study of the material was done in various electrolytes which confirmed the intercalation of the different cations of the electrolytes in the layers of the material. The metallic 1T phase of the material also achieved much high capacitance which was observed to ~ 400-700 F cm^{-3}, a much higher capacitance than its 2H counterpart.[77] Balasingam *et al.* were able to evaluate the performance of $MoSe_2$ as an electrode material in supercapacitors.[78] The group suggested that there are EDLC and pseudocapacitive characteristics observed in the analysis of the material using cyclic voltammetry (CV). The CV of the material at various scan rates maintained a rectangular shape which show EDLC behaviour. However, there was peak broadening at the anodic and cathodic scans which indicate redox behaviour in the $MoSe_2$ nanosheets. The storage mechanisms are represented as:

$$(MoSe_2) + H^+ + e^- \leftrightarrow MoSe - SeH^+ \quad (2.14)$$

$$(MoSe_2)\ surface + H^+ + e^- \leftrightarrow (MoSe_2 - H^+)\ surface \quad (2.15)$$

Equation (14) describes the EDLC storage mechanism and equation (15) describes the pseudocapacitance storage mechanism.

The $MoSe_2$ electrodes exhibited a specific capacitance of 199 Fg^{-1} at a scan rate of 2 mV, the electrodes also had a cyclic stability of 75 % at 10 000 cycles.

2.4 Electrochemical techniques for evaluating supercapacitors

There are two electrochemical cell configurations that are used for the characterization of supercapacitor electrode materials, the two-electrode cell and the three-electrode cell. The two-electrode system is suitable for evaluating fully assembled supercapacitors as the system architecture resembles a fully assembled supercapacitor, this system is used for evaluating a supercapacitor at non-ideal conditions. The three-electrode system is more suitable for the evaluation of supercapacitor electrode materials and not a fully assembled device, this involves the

use of minute amounts of active materials. As previously mentioned the two-electrode system configuration resembles a fully assembled supercapacitor.[79] The system has two electrodes, a cathode and an anode. The electrodes are separated by a separator to eliminate the risk of short circuits. The electrodes and the separator between them are sandwiched by metal current collectors. This system is encapsulated in a metal casing that is used to apply pressure to it. The cell is then dipped into an electrolyte that would be ideally be sucked up by the separator. The whole cell is then vacuum dried to remove any air. The electrodes are prepared by making a film of the active material on stable electrodes sheets either by pasting or spraying the active material on the sheets.[80] The three-electrode system consists of a reference electrode, a counter electrode and a working electrode. The reference electrode is normally an Ag/AgCl, a platinum wire is used as the counter electrode and the working electrode is then the active material coated on a current collector. The working electrode is connected to a potentiostat that control the potential of the working electrode and monitors the current or the current is controlled and the potential is monitored. There are various working electrode set-ups that can be utilized for electrode materials testing, the most common is the use of a stainless steel or nickel foam current collector with the active material coated on the surface in the form of a paste.[81-82]The paste is created by using the active material, a binder which is normally which is normally a binder such as PVDF (polyvinylidene fluoride) to ensure that active material does not dissolve into the electrolyte, carbon is normally added into the mixture for materials that do not have sufficient electrical conductivity.[81-82]

2.4.1 Cyclic Voltammetry

Cyclic voltammetry (CV) is an electrochemical technique that is able to evaluate electrochemical phenomena such as redox reactions, the technique is able to give qualitative and quantitative data about the material being studied. To obtain a CV, a potential is applied to the working electrode with respect to the fixed potential of a reference electrode. The potential of the working electrode linearly sweeps back and forth between two potentials. These potentials are normally limited by the operating limits of the electrolyte being used. The potential is scanned back and forth between the potential range at various scan rates (v) which influence the current observed

(v α $\sqrt{i}$).[83] The current (i) is then plotted against the potential applied (*E*) to yield a CV. The cyclic voltammograms of an ideal supercapacitor are shown in Fig. 2.9.

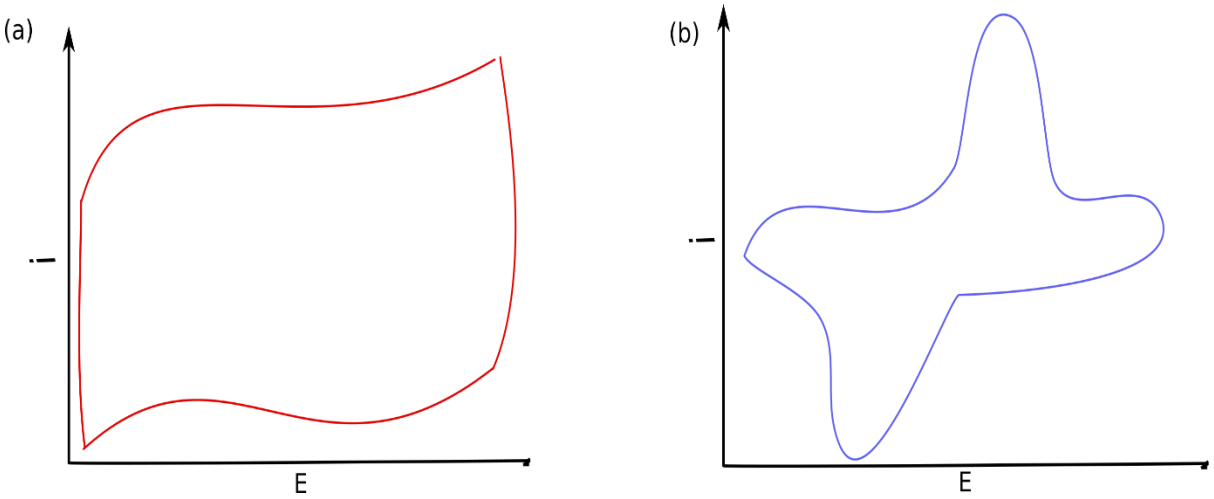

Figure 2.9: Voltammogram shapes of (a) electric double layer supercapacitance, (b) pseudocapacitance.

The ideal voltammogram for capacitative current would be perfectly rectangular. Supercapacitor materials do not behave ideally so for a EDLC the voltammogram has a distorted rectangular shape as shown in Fig. 2.9(a) and for a pseudocapacitor the oxidation and reduction peaks for the faradaic electron transfer reactions become visible Fig. 2.9(b).[84-85] The CV is primarily used to determine whether the electrode material behaves like a supercapacitor but it can also be used to determine capacitance. The capacitance can be calculated using the following equation:

$$C = \frac{\int idV}{2v\Delta V} \tag{2.16}$$

Where $\int idV$ is the total area under the peak, v is the scan rate and ΔV is the potential window at which the potential is being scanned.[86] The specific capacitance (C_s) can be calculated by dividing the capacitance with the mass of the active material used in the measurement.

$$Cs = \frac{C}{m} \tag{2.17}$$

Where m is the mass of active material used in the measurement. The specific capacitance is the more accurate value amount of material used for measurement will affect the capacitance calculated. The specific capacitance can be used as a standard to use when comparing the performance of different materials.

2.4.2 Galvanostatic charge-discharge (GCD)

GCD measurements are used to evaluate the performance of the electrode active materials after continual charge and discharge processes. GCD is essentially a chrono electrochemical method where either the potential or current is measured with respect to time while the other parameter is kept constant. In GCD the measurements are carried out by applying a constant current and measuring the change in potential with respect to time.[87] The discharge curve in a GCD measurement is used to determine the capacitance, this is the more reliable and generally accepted way of determining capacitance. The discharge curves for EDLC and pseudocapacitors are different due to their difference in the discharge mechanism, the EDLC discharges linearly as shown in Fig. 2.10(a) while a pseudocapacitor in non-linear due to the redox reactions as depicted in Fig. 2.10b.[88-89]

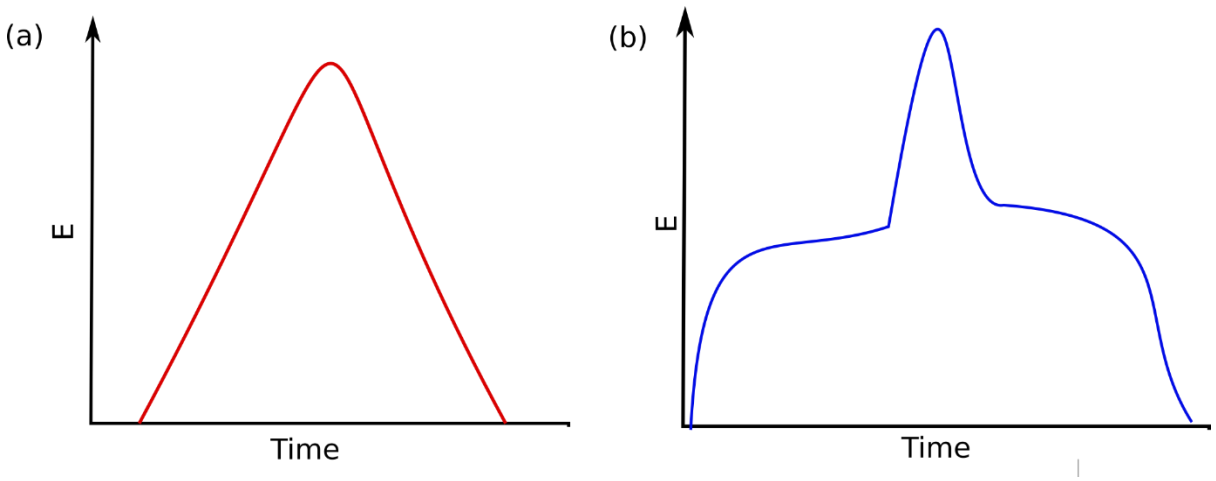

Figure 2.10: The GCD curves for: (a) electric double layer supercapacitor, (b) pseudocapacitance

The capacitance for an EDLC supercacapcitor is calculated from the slope of the linear discharge curve:

$$C = \frac{I}{dV/dt} \tag{2.18}$$

Where I is the applied current and dV/dt is the slope of the discharge curve. The capacitance in a pseudocapacitor is determined as follows

$$C = \frac{(\Delta t)(I)}{\Delta V} \tag{2.19}$$

where Δt is the time it takes to discharge, I is the applied current and ΔV is the change in the potential in the discharging phase. In the discharge curve, there is a rapid and sudden drop in the potential that is observed in the beginning of the discharge process.

This drop in the potential is called the IR(internal resistance) drop, the value of the IR drop can be used to calculate the ESR.[90] The ESR is calculated using the following:

$$ESR = \frac{\Delta V(IR\ drop)}{2I} \quad (2.20)$$

Where ΔV(IR drop) is the change in potential at initial discharge and I is the applied current.

Internal resistance

The ESR is an important parameter in the evaluation of the performance of a supercapacitor as it represents the resistance of the supercapacitor components such as contact resistance (i.e. resistance between current collector and electrodes) and electrolyte resistance.[91] ESR affects the power delivery performance of the supercapacitor, this would effectively impede the charging and discharging in the device.

2.4.3 Electrical Impedance spectroscopy (EIS)

The measurement of resistance in a circuit only applies to a single element in the circuit and not the entire circuit, impedance on the other hand measures the ability of a whole circuit to resist the flow of current.[92] In the experiment, a small sinusoidal potential is applied and the response of the cell is measured, this is done at various frequencies. The response is displayed as either a Nyquist or Bode plot. Impedance assumes an AC current of a specific frequency in Hz.[93] In supercapacitor evaluation, the Nyquist plot is the frequently used and is represented in Fig. 2.11. The Nyquist plot is normally separated into three segments: high, medium and low frequency regions. The horizontal axis is the real axis and the vertical axis is the imaginary impedance axis. The high frequency region of the region of the Nyquist indicates the equivalent series resistance.

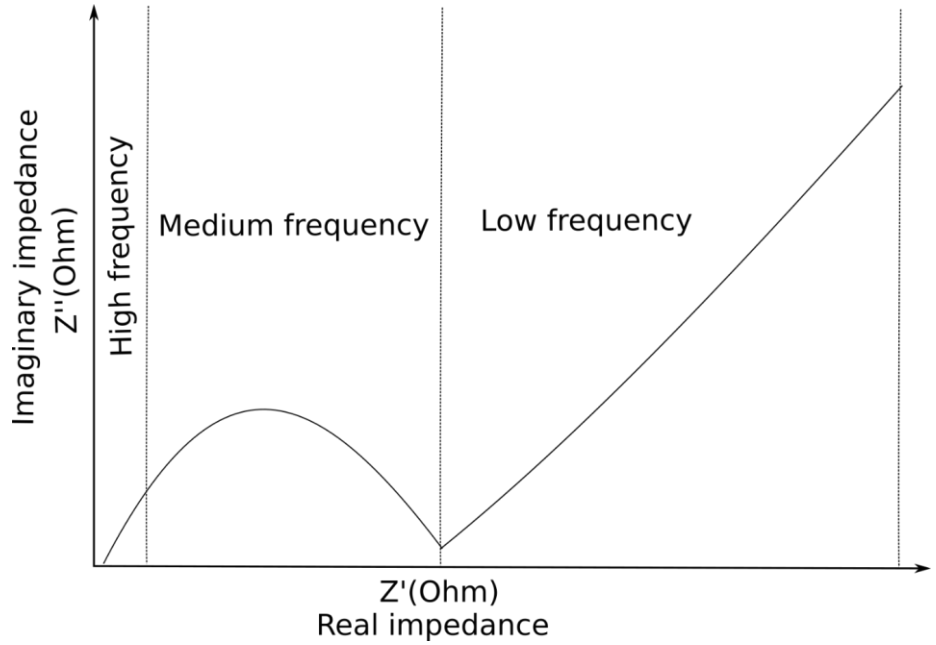

Figure 2.11: Typical complex plane Nyquist plot.

The ESR can be determined by reading the value where the curve intersects the x-axis which represents the real impedance.[94] The middle section which resembles a semi-circle represents the charge transfer resistance between the electrolyte and the electrode surface. The low frequency region mass transport processes are dominant. The diameter of the semi-circle is a measure of the charge transfer resistance, the smaller the diameter the less dominant the charge transfer resistance. The slope of the signal in the low frequency region is a measure of the electrolyte diffusion referred to as the Warburg resistance, low diffusion resistance will result in a steep slope of the graph in the low frequency region. These systems are normally quite complex so models are used to interpret what is happening in the system. The electrochemical system is modelled as an electrical circuit this circuit is called an equivalence circuit and models the cell and its chemistry.[95] The equivalent circuit measurements is fitted against the measured impedance spectra, depending on how well the model fits the impedance spectra it can be used to make predictions on the behaviour of the electrochemical cell. Primarily though in supercapacitors the method is just used to determine if the cell shows supercapacitor behaviour and to determine the ESR.

2.4.4 Cycle stability

An ideal supercapacitor should operate at full capacity after being continually charged and discharged, therefore cycle stability is another important parameter to evaluate electrode materials. Electrode materials being tested at lab scale are normally tested for 1000 to 10 000 cycles. GCD measurement are used to evaluate cycle stability, a single charge-discharge at a constant current density constitutes a single cycle.[96] There are several processes that can reduce the performance of the electrode material, subjecting the electrode materials to an extreme amount of charge-discharge cycles degrades the materials and causes corrosion in the components of the supercapacitor which then leads to a reduction in the capacitance.[88] When the electrode material degrades it causes the ESR to increase thus causing the performance of the supercapacitor to decreases.

References

1. Amrouche, S. O.; Rekioua, D.; Rekioua, T.; Bacha, S., Overview of energy storage in renewable energy systems. *International Journal of Hydrogen Energy* **2016,** *41* (45), 20914-20927.
2. Barzin, R.; Chen, J. J.; Young, B. R.; Farid, M. M., Peak load shifting with energy storage and price-based control system. *Energy* **2015,** *92*, 505-514.
3. Goodenough, J.; Abruna, H.; Buchanan, M. *Basic Research Needs for Electrical Energy Storage. Report of the Basic Energy Sciences Workshop on Electrical Energy Storage, April 2-4,* **2007**; DOESC (USDOE Office of Science (SC)): 2007.
4. Dunn, B.; Kamath, H.; Tarascon, J.-M., Electrical energy storage for the grid: a battery of choices. *Science* **2011,** *334* (6058), 928-935.
5. Bissett, M. A.; Worrall, S. D.; Kinloch, I. A.; Dryfe, R. A., Comparison of two-dimensional transition metal dichalcogenides for electrochemical supercapacitors. *Electrochimica Acta* **2016,** *201*, 30-37.
6. Gidwani, M.; Bhagwani, A.; Rohra, N., Supercapacitors: the near Future of Batteries. *International Journal of Engineering Inandntions* **2014,** *4*, 22-27.
7. Miller, J. R.; Simon, P., Electrochemical capacitors for energy management. *Science Magazine* **2008,** *321* (5889), 651-652.
8. Simon, P.; Gogotsi, Y., Materials for electrochemical capacitors. *Nature materials* **2008,** *7* (11), 845-854.

9. Hamilton, T., Next stop: Ultracapacitor buses. *Technology Review, MIT Technology Review* **2009**.
10. Hall, P. J.; Bain, E. J., Energy-storage technologies and electricity generation. *Energy policy* **2008,** *36* (12), 4352-4355.
11. Kumar, P.; Abuhimd, H.; Wahyudi, W.; Li, M.; Ming, J.; Li, L.-J., Two-Dimensional Layered Materials for Energy Storage Applications. *ECS Journal of Solid State Science and Technology* **2016,** *5* (11), Q3021-Q3025.
12. Savjani, N.; Lewis, E. A.; Bissett, M. A.; Brent, J. R.; Dryfe, R. A.; Haigh, S. J.; O'Brien, P., Synthesis of Lateral Size-Controlled Monolayer 1 H-MoS_2@ Oleylamine as Supercapacitor Electrodes. *Chemistry of Materials* **2016,** *28* (2), 657-664.
13. Wu, Z.; Li, B.; Xue, Y.; Li, J.; Zhang, Y.; Gao, F., Fabrication of defect-rich MoS_2 ultrathin nanosheets for application in lithium-ion batteries and supercapacitors. *Journal of Materials Chemistry A* **2015,** *3* (38), 19445-19454.
14. Li, X.; Zhu, H., Two-dimensional MoS_2: Properties, preparation, and applications. *Journal of Materiomics* **2015,** *1* (1), 33-44.
15. Yazyev, O. V.; Kis, A., MoS_2 and semiconductors in the flatland. *Materials Today* **2015,** *18* (1), 20-30.
16. Yu, J.; Li, J.; Zhang, W.; Chang, H., Synthesis of high quality two-dimensional materials via chemical vapor deposition. *Chemical Science* **2015,** *6* (12), 6705-6716.
17. Liu, B.; Fathi, M.; Chen, L.; Abbas, A.; Ma, Y.; Zhou, C., Chemical vapor deposition growth of monolayer WSe_2 with tunable device characteristics and growth mechanism study. *ACS nano* **2015,** *9* (6), 6119-6127.
18. Chang, J.; Waclawik, E. R., Colloidal semiconductor nanocrystals: controlled synthesis and surface chemistry in organic media. *RSC Advances* **2014,** *4* (45), 23505-23527.
19. Kho, R.; Torres-Martinez, C. L.; Mehra, R. K., A simple colloidal synthesis for gram-quantity production of water-soluble ZnS nanocrystal powders. *Journal of colloid and interface science* **2000,** *227* (2), 561-566.
20. Peng, X., Mechanisms for the shape-control and shape-evolution of colloidal semiconductor nanocrystals. *Advanced Materials* **2003,** *15* (5), 459-463.

21. Han, S. A.; Bhatia, R.; Kim, S.-W., Synthesis, properties and potential applications of two-dimensional transition metal dichalcogenides. *Nano Convergence* **2015,** *2* (1), 17.
22. Sipos, B.; Kusmartseva, A. F.; Akrap, A.; Berger, H.; Forró, L.; Tutĭs, E., From Mott state to superconductivity in 1T-TaS_2. *Nature materials* **2008,** *7* (12), 960.
23. Gordon, R.; Yang, D.; Crozier, E.; Jiang, D.; Frindt, R., Structures of exfoliated single layers of WS_2, MoS_2, and $MoSe_2$ in aqueous suspension. *Physical Review B* **2002,** *65* (12), 125407.
24. Mak, K. F.; Shan, J., Photonics and optoelectronics of 2D semiconductor transition metal dichalcogenides. *Nature Photonics* **2016,** *10* (4), 216-226.
25. Bernardi, M.; Ataca, C.; Palummo, M.; Grossman, J. C., Optical and electronic properties of Two-Dimensional layered materials. *Nanophotonics* **2017,** *6* (2), 479-493.
26. Lv, R.; Robinson, J. A.; Schaak, R. E.; Sun, D.; Sun, Y.; Mallouk, T. E.; Terrones, M., Transition metal dichalcogenides and beyond: synthesis, properties, and applications of single-and few-layer nanosheets. *Accounts of chemical research* **2014,** *48* (1), 56-64.
27. Chhowalla, M.; Shin, H. S.; Eda, G.; Li, L.-J.; Loh, K. P.; Zhang, H., The chemistry of two-dimensional layered transition metal dichalcogenide nanosheets. *Nature chemistry* **2013,** *5* (4), 263-275.
28. Kappera, R.; Voiry, D.; Yalcin, S. E.; Branch, B.; Gupta, G.; Mohite, A. D.; Chhowalla, M., Phase-engineered low-resistance contacts for ultrathin MoS_2 transistors. *Nature materials* **2014,** *13* (12), 1128.
29. Sun, Y.; Wang, D.; Shuai, Z., Indirect-to-Direct Band Gap Crossover in Few-Layer Transition Metal Dichalcogenides: A Theoretical Prediction. *The Journal of Physical Chemistry C* **2016,** *120* (38), 21866-21870.
30. Dong, N.; Li, Y.; Feng, Y.; Zhang, S.; Zhang, X.; Chang, C.; Fan, J.; Zhang, L.; Wang, J., Optical limiting and theoretical modelling of layered transition metal dichalcogenide nanosheets. *Scientific reports* **2015,** *5*.
31. Coehoorn, R.; Haas, C.; De Groot, R., Electronic structure of $MoSe_2$, MoS_2, and WSe_2. II. The nature of the optical band gaps. *Physical Review B* **1987,** *35* (12), 6203.

32. Tongay, S.; Zhou, J.; Ataca, C.; Lo, K.; Matthews, T. S.; Li, J.; Grossman, J. C.; Wu, J., Thermally driven crossover from indirect toward direct bandgap in 2D semiconductors: $MoSe_2$ versus MoS_2. *Nano letters* **2012,** *12* (11), 5576-5580.
33. Eftekhari, A., Molybdenum diselenide (MoSe 2) for energy storage, catalysis, and optoelectronics. *Applied Materials Today* **2017,** *8*, 1-17.
34. Pellegrino, T.; Kudera, S.; Liedl, T.; Muñoz Javier, A.; Manna, L.; Parak, W. J., On the development of colloidal nanoparticles towards multifunctional structures and their possible use for biological applications. *Small* **2005,** *1* (1), 48-63.
35. Wang, Y.; Xia, Y., Bottom-up and top-down approaches to the synthesis of monodispersed spherical colloids of low melting-point metals. *Nano letters* **2004,** *4* (10), 2047-2050.
36. Chestnoy, N.; Harris, T. D.; Hull, R.; Brus, L. E., Luminescence and photophysics of cadmium sulfide semiconductor clusters: the nature of the emitting electronic state. *The Journal of Physical Chemistry* **1986,** *90* (15), 3393-3399.
37. Murray, C.; Norris, D. J.; Bawendi, M. G., Synthesis and characterization of nearly monodisperse CdE (E=sulfur, selenium, tellurium) semiconductor nanocrystallites. *Journal of the American Chemical Society* **1993,** *115* (19), 8706-8715.
38. Franke, D.; Harris, D. K.; Chen, O.; Bruns, O. T.; Carr, J. A.; Wilson, M. W.; Bawendi, M. G., Continuous injection synthesis of indium arsenide quantum dots emissive in the short-wavelength infrared. *Nature communications* **2016,** *7*.
39. Xuan, T.-T.; Liu, J.-Q.; Yu, C.-Y.; Xie, R.-J.; Li, H.-L., Facile synthesis of cadmium-free Zn-In-S: Ag/ZnS nanocrystals for bio-imaging. *Scientific reports* **2016,** *6*, 24459.
40. Becker, R.; Döring, W., Kinetische behandlung der keimbildung in übersättigten dämpfen. *Annalen der Physik* **1935,** *416* (8), 719-752.
41. LaMer, V. K.; Dinegar, R. H., Theory, production and mechanism of formation of monodispersed hydrosols. *Journal of the American Chemical Society* **1950,** *72* (11), 4847-4854.
42. Polte, J., Fundamental growth principles of colloidal metal nanoparticles–a new perspective. *CrystEngComm* **2015,** *17* (36), 6809-6830.

43. Gibbs, J. W., On the equilibrium of heterogeneous substances. *American Journal of Science* **1878,** (96), 441-458.
44. Ostwald, W., Emancipation from scientific materialism. *Science Progress (1894-1898)* **1896,** *4* (24), 419-436.
45. Wulff, G., On the question of speed of growth and dissolution of crystal surfaces. *Z. Kristallogr* **1901,** *34*, 449-530.
46. Zhang, Q.; Li, N.; Goebl, J.; Lu, Z.; Yin, Y., A systematic study of the synthesis of silver nanoplates: is citrate a “magic” reagent? *Journal of the American Chemical Society* **2011,** *133* (46), 18931-18939.
47. Baletto, F.; Ferrando, R., Structural properties of nanoclusters: Energetic, thermodynamic, and kinetic effects. *Reviews of modern physics* **2005,** *77* (1), 371.
48. Chauhan, H.; Kumar, Y.; Deka, S., New synthesis of two-dimensional CdSe/CdS core@ shell dot-in-hexagonal platelet nanoheterostructures with interesting optical properties. *Nanoscale* **2014,** *6* (17), 10347-10354.
49. Chen, H.; Chen, Z.; Ge, B.; Chi, Z.; Chen, H.; Wu, H.; Cao, C.; Duan, X., General Strategy for Two-dimensional Transition Metal Dichalcogenides by Ion Exchange. *Chemistry of Materials* **2017,** *29* (23), 10019-10026.
50. van Embden, J.; Chesman, A. S.; Jasieniak, J. J., The heat-up synthesis of colloidal nanocrystals. *Chemistry of Materials* **2015,** *27* (7), 2246-2285.
51. Sperling, R. A.; Parak, W., Surface modification, functionalization and bioconjugation of colloidal inorganic nanoparticles. *Philosophical Transactions of the Royal Society of London A: Mathematical, Physical and Engineering Sciences* **2010,** *368* (1915), 1333-1383.
52. Pérez-Juste, J.; Pastoriza-Santos, I.; Liz-Marzán, L. M.; Mulvaney, P., Gold nanorods: synthesis, characterization and applications. *Coordination Chemistry Reviews* **2005,** *249* (17), 1870-1901.
53. Döllefeld, H.; Hoppe, K.; Kolny, J.; Schilling, K.; Weller, H.; Eychmüller, A., Investigations on the stability of thiol stabilized semiconductor nanoparticles. *Physical Chemistry Chemical Physics* **2002,** *4* (19), 4747-4753.
54. Bakshi, M. S., How surfactants control crystal growth of nanomaterials. *Crystal Growth & Design* **2015,** *16* (2), 1104-1133.

55. Ithurria, S.; Dubertret, B., Quasi 2D colloidal CdSe platelets with thicknesses controlled at the atomic level. *Journal of the American Chemical Society* **2008,** *130* (49), 16504-16505.
56. Son, J. S.; Wen, X. D.; Joo, J.; Chae, J.; Baek, S. i.; Park, K.; Kim, J. H.; An, K.; Yu, J. H.; Kwon, S. G., Large-Scale Soft Colloidal Template Synthesis of 1.4 nm Thick CdSe Nanosheets. *Angewandte Chemie* **2009,** *121* (37), 6993-6996.
57. Jung, W.; Lee, S.; Yoo, D.; Jeong, S.; Miró, P.; Kuc, A.; Heine, T.; Cheon, J., Colloidal synthesis of single-layer MSe_2 (M= Mo, W) nanosheets via anisotropic solution-phase growth approach. *Journal of the American Chemical Society* **2015,** *137* (23), 7266-7269.
58. Guo, W.; Chen, Y.; Wang, L.; Xu, J.; Zeng, D.; Peng, D.-L., Colloidal synthesis of $MoSe_2$ nanonetworks and nanoflowers with efficient electrocatalytic hydrogen-evolution activity. *Electrochimica Acta* **2017,** *231*, 69-76.
59. Demming, A., Supercapacitors empower sustainable energy storage. *Nanotechnology* **2016,** *27* (25), 250201.
60. Wang, X.; Lu, X.; Liu, B.; Chen, D.; Tong, Y.; Shen, G., Flexible Energy-Storage Devices: Design Consideration and Recent Progress. *Advanced Materials* **2014,** *26* (28), 4763-4782.
61. Miller, J. R.; Simon, P., Electrochemical capacitors for energy management. *Science Magazine* **2008,** *321* (5889), 651-652.
62. Venkataraman, A. Pseudocapacitors for Energy Storage. Portland State University, **2015.**
63. Aslani, M., Electrochemical double layer capacitors (supercapacitors). Stanford University: **2012.**
64. Laforgue, A.; Simon, P.; Fauvarque, J.; Conté, M.; Sarrau, J.; Lailler, P., Hybrid Supercapacitors–From Laboratory to Industrial Development. *work* **2002,** *6*, 8.
65. Jayalakshmi, M.; Balasubramanian, K., Simple capacitors to supercapacitors-an overview. *Int. J. Electrochem. Sci* **2008,** *3* (11), 1196-1217.
66. Obreja, V. V.; Dinescu, A.; Obreja, A. C., Activated carbon based electrodes in commercial supercapacitors and their performance. *International Review of Electrical Engineering* **2010,** *5* (1).
67. Pan, H.; Li, J.; Feng, Y., Carbon nanotubes for supercapacitor. *Nanoscale research letters* **2010,** *5* (3), 654.

68. Augustyn, V.; Simon, P.; Dunn, B., Pseudocapacitive oxide materials for high-rate electrochemical energy storage. *Energy & Environmental Science* **2014,** *7* (5), 1597-1614.
69. Grigorchak, I., Redox processes and pseudocapacitance of capacitors in light of intercalation nanotechnologies. *Russian journal of electrochemistry* **2003,** *39* (6), 695-698.
70. Oviedo, O. A.; Reinaudi, L.; García, S. G.; Leiva, E. P. M., *Underpotential deposition*. Springer: 2016.
71. Zhu, Y.; Peng, L.; Chen, D.; Yu, G., Intercalation pseudocapacitance in ultrathin $VOPO_4$ nanosheets: toward high-rate alkali-ion-based electrochemical energy storage. *Nano letters* **2015,** *16* (1), 742-747.
72. Chang, B.-Y.; Ahn, E.; Park, S.-M., Real-time staircase cyclic voltammetry Fourier transform electrochemical impedance spectroscopic studies on underpotential deposition of lead on gold. *The Journal of Physical Chemistry C* **2008,** *112* (43), 16902-16909.
73. Ohzuku, T.; Sawai, K.; Hirai, T., Electrochemistry of L-niobium pentoxide a lithium/non-aqueous cell. *Journal of power sources* **1987,** *19* (4), 287-299.
74. Trasatti, S.; Buzzanca, G., Ruthenium dioxide: a new interesting electrode material. Solid state structure and electrochemical behaviour. *Journal of Electroanalytical Chemistry and Interfacial Electrochemistry* **1971,** *29* (2), A1-A5.
75. Dmowski, W.; Egami, T.; Swider-Lyons, K. E.; Love, C. T.; Rolison, D. R., Local atomic structure and conduction mechanism of nanocrystalline hydrous RuO_2 from X-ray scattering. *The Journal of Physical Chemistry B* **2002,** *106* (49), 12677-12683.
76. Karade, S. S.; Dubal, D. P.; Sankapal, B. R., MoS_2 ultrathin nanoflakes for high performance supercapacitors: room temperature chemical bath deposition (CBD). *RSC Advances* **2016,** *6* (45), 39159-39165.
77. Acerce, M.; Voiry, D.; Chhowalla, M., Metallic 1T phase MoS_2 nanosheets as supercapacitor electrode materials. *Nature nanotechnology* **2015,** *10* (4), 313-318.
78. Balasingam, S. K.; Lee, J. S.; Jun, Y., Few-layered $MoSe_2$ nanosheets as an advanced electrode material for supercapacitors. *Dalton Transactions* **2015,** *44* (35), 15491-15498.

79. Tsay, K.-C.; Zhang, L.; Zhang, J., Effects of electrode layer composition/thickness and electrolyte concentration on both specific capacitance and energy density of supercapacitor. *Electrochimica Acta* **2012,** *60*, 428-436.
80. Yong, S.; Owen, J.; Tudor, M.; Beeby, S. In *Flexible solid-state fabric based supercapacitor*, Journal of Physics: Conference Series, IOP Publishing: 2015; p 012074.
81. Khawula, T. N.; Raju, K.; Franklyn, P. J.; Sigalas, I.; Ozoemena, K. I., The Effects of Morphology Re-Arrangements on the Pseudocapacitive Properties of Mesoporous Molybdenum Disulfide (MoS_2) Nanoflakes. *Journal of The Electrochemical Society* **2016,** *163* (9), A1927-A1935.
82. Yuan, C.; Zhang, X.; Su, L.; Gao, B.; Shen, L., Facile synthesis and self-assembly of hierarchical porous NiO nano/micro spherical superstructures for high performance supercapacitors. *Journal of Materials Chemistry* **2009,** *19* (32), 5772-5777.
83. Mabbott, G. A., An introduction to cyclic voltammetry. *J. Chem. Educ* **1983,** *60* (9), 697.
84. Lekakou, C.; Moudam, O.; Markoulidis, F.; Andrews, T.; Watts, J.; Reed, G., Carbon-based fibrous EDLC capacitors and supercapacitors. *Journal of Nanotechnology* **2011,** *2011*.
85. Muller, G. A.; Cook, J. B.; Kim, H.-S.; Tolbert, S. H.; Dunn, B., High performance pseudocapacitor based on 2D layered metal chalcogenide nanocrystals. *Nano letters* **2015,** *15* (3), 1911-1917.
86. Kim, B. K.; Chabot, V.; Yu, A., Carbon nanomaterials supported Ni (OH) 2/NiO hybrid flower structure for supercapacitor. *Electrochimica Acta* **2013,** *109*, 370-380.
87. Xu, M.-W.; Zhao, D.-D.; Bao, S.-J.; Li, H.-L., Mesoporous amorphous MnO2 as electrode material for supercapacitor. *Journal of Solid State Electrochemistry* **2007,** *11* (8), 1101-1107.
88. Guo, C. X.; Li, C. M., A self-assembled hierarchical nanostructure comprising carbon spheres and graphene nanosheets for enhanced supercapacitor performance. *Energy & Environmental Science* **2011,** *4* (11), 4504-4507.
89. Li, H.; Yu, M.; Wang, F.; Liu, P.; Liang, Y.; Xiao, J.; Wang, C.; Tong, Y.; Yang, G., Amorphous nickel hydroxide nanospheres with ultrahigh capacitance and

energy density as electrochemical pseudocapacitor materials. *Nature communications* **2013,** *4*, 1894.

90. Stoller, M. D.; Ruoff, R. S., Best practice methods for determining an electrode material's performance for ultracapacitors. *Energy & Environmental Science* **2010,** *3* (9), 1294-1301.
91. Show, Y.; Imaizumi, K., Decrease in equivalent series resistance of electric double-layer capacitor by addition of carbon nanotube into the activated carbon electrode. *Diamond and related materials* **2006,** *15* (11), 2086-2089.
92. Orazem, M. E.; Tribollet, B., *Electrochemical impedance spectroscopy*. John Wiley & Sons: 2011; Vol. 48.
93. Macdonald, J. R., Impedance spectroscopy. *Annals of biomedical engineering* **1992,** *20* (3), 289-305.
94. Taberna, P.; Simon, P.; Fauvarque, J.-F., Electrochemical characteristics and impedance spectroscopy studies of carbon-carbon supercapacitors. *Journal of The Electrochemical Society* **2003,** *150* (3), A292-A300.
95. Fletcher, S.; Black, V. J.; Kirkpatrick, I., A universal equivalent circuit for carbon-based supercapacitors. *Journal of Solid State Electrochemistry* **2014,** *18* (5), 1377-1387.
96. Zhou, J.; Lian, J.; Hou, L.; Zhang, J.; Gou, H.; Xia, M.; Zhao, Y.; Strobel, T. A.; Tao, L.; Gao, F., Ultrahigh volumetric capacitance and cyclic stability of fluorine and nitrogen co-doped carbon microspheres. *Nature communications* **2015,** *6*, 8503.

Chapter 3: Colloidal synthesis of $MoSe_2$ nanomaterials

3.1 Introduction

Transition metal dichalcogenide (TMDs) are fast becoming one of the most exciting materials,their interesting properties have put them in the forefront for use in various applications and technologies including energy storage and generation devices, field effect transistors and biosensors.[1-2] Thus far MoS_2 has been the most explored member of the TMDs but more attention is being directed to the synthesis and characterisation of various other TMDs such as $MoSe_2$. $MoSe_2$ has particularly emerged as one of the more interesting member of the TMDs, the material has been explored as a candidate to replace Pt as a counter electrode in dye sensitized solar cells and it has also been explored as an electrode in supercapacitors with relative success.[3-4] One critical factor that could determine whether the material can be used commercially for various devices is the ability to synthesize the material at large scale in a cost-effective manner.[5] The exfoliation methods (mechanical and chemical exfoliation) currently utilised to synthesize mono to few-layer TMDs are not yet suitable for large scale production. Another method being explored is Chemical vapour deposition (CVD) which is a bottom-up approach to the synthesis of the materials. This method has been used to synthesize high quality monolayer TMDs.[6] Unfortunately, it utilises high temperatures and is a very complicated synthetic method thus it is also unsuitable for the large-scale production of the material presently.[6] The colloidal synthetic methods are now being explored for the synthesis of the material; these are relatively simple methods that can potentially be used for large scale production of semiconductor nanomaterials materials.[7] Colloidal synthesis has been used to synthesize various layered semiconductor nanomaterials. Hyeon *et al.* have shown that a soft colloidal synthetic method can be used for the synthesis of ultrathin CdSe nanosheets.[8] This was done using an alkyl amine and oleic acid as the soft template. Colloidal synthesis has also been used by Berends *et al.* to synthesize multinary semiconductors such a copper indium sulphide (CIS).[9] They were able to synthesize triangular and hexagonal shaped nanosheets of CIS with a thickness of about 3 nm and lateral dimensions ranging from 20 to 1000 nm. Zhou *et al.* have synthesized MoS_2 and WS_2 using a colloidal synthesis method that allows for control of the lateral sizes and layer number.[10] They have been able to control the lateral sizes by varying the Mo:S ratio and the layer number using a multi-injection method. Sun et al have been

able to use a colloidal method to synthesize $MoSe_2$ nanoflowers.[11] In this work a colloidal synthetic method was developed for the synthesis of $MoSe_2$ nanomaterials. The effect of the reaction time on the structural, morphological and optical properties of the nanomaterials was investigated.

3.2 Materials and methods

3.2.1 Chemicals

Molybdenum hexacarbonyl (($Mo(CO)_6$), 98%, Sigma-Aldrich), selenourea (CH_4N_2Se, 98%, Sigma-Aldrich) and oleylamine (OAm, 70%, Sigma-Aldich) were used as received without purification.

3.2.2 Characterisation techniques

The structural properties were investigated using powder X-ray diffraction(PXRD) and Raman spectroscopy. The phase purity, crystallinity and preferred crystal orientation of the products were examined by using XRD on a Bruker MeasSrv (D2-205530)/D2-205530 diffractometer using secondary graphite monochromated CoKα radiation (λ 1.78897 Å) at 30 kV/30 mA. Measurements were taken using a glancing angle of incidence detector at an angle of 2°, for 2θ values over 10 - 90° in steps of 0.026° with a step time of 37 s and at a temperature of 25 °C. Raman spectroscopy (J-Y T64000 micro-Raman spectrometer, Horiba Jobin-Yvon, Ltd., Stanmore, UK) equipped with a liquid nitrogen cooled charge coupled device detector. All samples were measured after excitation with a laser wavelength of 514.5 nm. The optical properties were determined using a Varian Cary Eclipse (Cary 50) UV-vis absorption spectrophotometer. The sample morphologies were determined by the transmission electron microscopy (TEM) carried out on a FEI Technai T12 TEM microscopy operated at an acceleration voltage of 200 kV with a beam spot size of 20 - 100 nm in TEM mode. HRTEM images were obtained from a JEOL JEM-2100 microscopy with a LAB6 filament and an EDS detector, operated at 200 kV.

3.2.3 Synthesis of $MoSe_2$ nanomaterials

A three-neck round bottom flask was filled with 20 ml of oleylamine and degassed in N_2 for 20 minutes under nitrogen. The temperature was increased to 50 ˚C and 0.362 g (2.49 mmol) of selenourea was added to the reaction mixture and stirred for 10 min. Molybdenum hexacarbonyl (0.212 g (0.802 mmol)) was put in a vial and

dissolved in oleylamine. The reaction mixture with selenourea turns a black color at 50 ˚C as shown in Fig. 3.1 (1) followed by a dark orange color at ~ 220 ˚C shown in Fig. 3.1 (2). The introduction of molybdenum hexacarbonyl at ~ 250 ˚C saw the reaction mixture turn black immediately (3). The mixture then begins to vigorously bubble due to a build-up of pressure in the flask which could be due to the CO gas being produced. Fig. 3.1 shows the progression of the reaction. The reaction mixture was kept at 300-310 ˚C and aliquots were taken at 30, 60, 90 and 120 min.

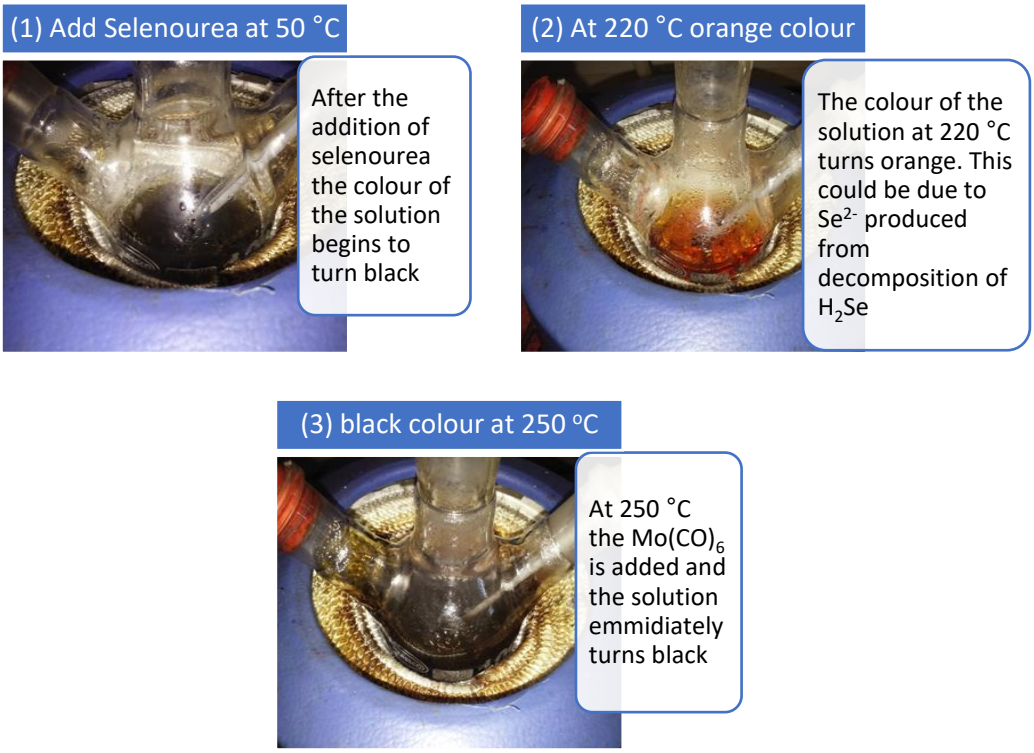

Figure 3.1: Progression of the reaction between selenourea and molybdenum hexacarbonyl.

It has been shown that thiourea decompose at ~ 180 ˚C to H_2S and a carboamide ($C(NH)_2$).[12] The selenourea seems to undergo the same decomposition producing H_2Se and the carboamiide, this is confirmed in Fig. 3.2 by the thermogravimetric analysis (TGA) of selenourea which suggests a decomposition at ~ 220 ˚C to H_2Se and the carboamide. The H_2Se then becomes the source of selenium. The H_2Se can the further decompose to form the monomer Se^{2-}. The dark orange colour observed in the reaction mixture is attributed to the presence of Se^{2-}.[13]

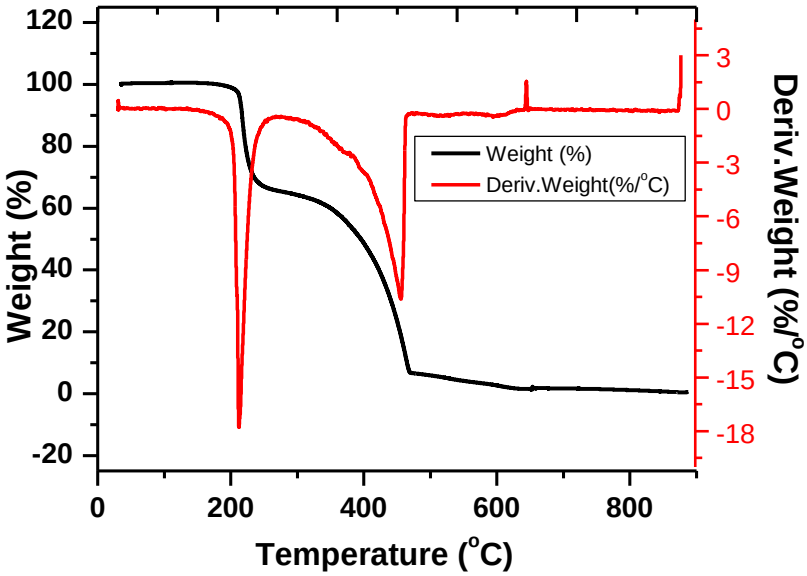

Figure 3.2: TGA of selenourea.

The $Mo(CO)_6$ which is the molybdenum source is introduced to the reaction mixture at ~ 250 °C. When the $Mo(CO)_6$ is introduced it undergoes a rapid decomposition, the decomposition process in this case is decarbonylation. The 6 carbonyl groups dissociate from the Mo atom which results in the release of the free Mo atom monomer.[14] The Mo would then react with the selenium in the reactions mixture to form $MoSe_2$. A schematic representation of the processes occurring during the reaction is represented in Scheme. 3.1.

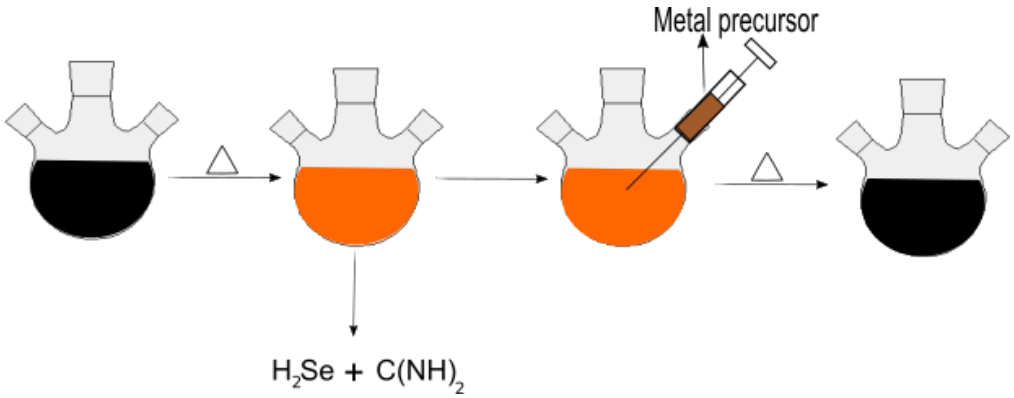

Scheme 3.1: Schematic representation of the reaction of selenourea and $Mo(CO)_6$ to produce $MoSe_2$ nanomaterials.

The proposed mechanism for the reaction is shown below.

$$2CH_4N_2Se \longrightarrow 2H_2Se + 2C(NH)_2 \quad (3.1)$$

$$Mo(CO)_6 + 2H_2Se \longrightarrow MoSe_2 + 6CO + 2H_2 \quad (3.2)$$

3.3 Results and discussion

Powder X-day diffraction (PXRD) was used to determine the composition, phase and crystallinity of the synthesized products. The powder diffraction patterns confirm the formation of hexagonal 2H phase $MoSe_2$ nanomaterials (JCPDS card no: 03-065-3999) as shown in Fig. 3.3. The broad nature of the peaks is characteristic of nanosized materials. The (002) peak observed at 10° and 20° is due to the stacking of the layers in the $MoSe_2$ nanostructure, thus the absence of the (002) in the diffraction pattern indicates the formation of monolayer nanosheets.[8,15] The appearance of the (002) peaks signifies that the nanosheet are multilayer. The (002) peak is not observed in the diffraction pattern for the 30 min aliquot which could be due to the formation of monolayer nanomaterials. The (002) peak begins to appear at 60 min, along with 3 unidentified peaks between 20-30°. These peaks could be due to impurities that creep up as the reaction progresses, especially since they disappear when the reaction reaches 90 min.

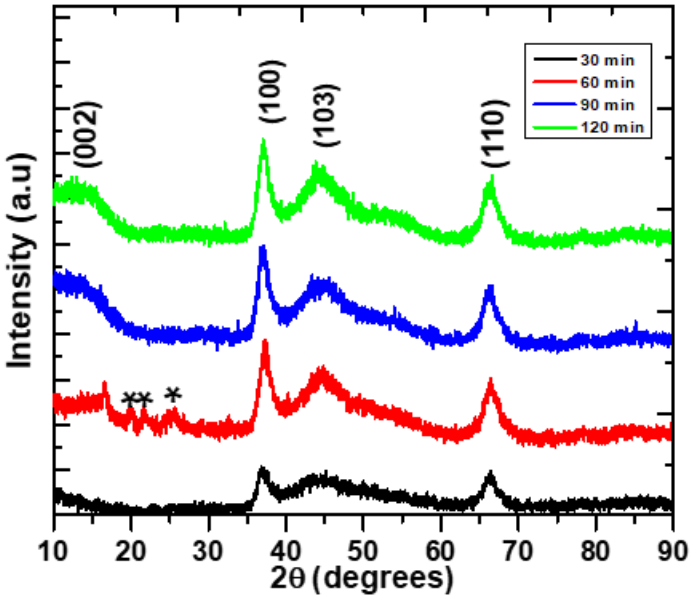

Figure 3.3: Powder diffraction patterns of $MoSe_2$ synthesized at 30, 60, 90 and 120 min. (*) impurities that appear and are phased at 90 min.

The crystallinity of the synthesized nanomaterials seems to improve with longer reaction times: The crystallinity of the material in the domain of the (103) peak increases as the reaction progresses. The (103) peak at 30 min is much broader and

less defined but it starts becoming sharper at 60 min. The (103) peaks also begins to show a shoulder peak at 50 ^{o} – 60 ^{o} at the 90 and 120 min aliquots which is identified as the (105) peak.

Raman spectroscopy is used primarily to confirm the formation of $MoSe_2$ nanomaterials and secondly the technique is used to estimate the number of layers on the nanosheets. The Raman spectrum of bulk $MoSe_2$ contains two characteristic peaks, the out of plane A_{1g} and the in plane E^1_{2g}.[16] In bulk $MoSe_2$ the A_{1g} is situated at ~ 242 cm^{-1} and the E^1_{2g} at ~ 286 cm^{-1}.[16] It has been shown that as the number of layers on the nanosheets decreases the A_{1g} red-shifts from the bulk.[16] The degree at which the peaks shift from the bulk can be used to estimate the number of layer on the nanosheets (e.g. to show whether the nanosheets are monolayer or multilayer). The Raman spectra of the product synthesized at 30, 60, 90 and 120 min all contain the A_{1g} and E^1_{2g} characteristic peaks as shown in Fig. 3.4 which confirms the formation of $MoSe_2$. The as synthesized products A_{1g} peak is situated at 237 cm^{-1} for the products synthesized at 30,60 and 90 and 120 min which is red-shifted from the bulk by 4 cm^{-1}.

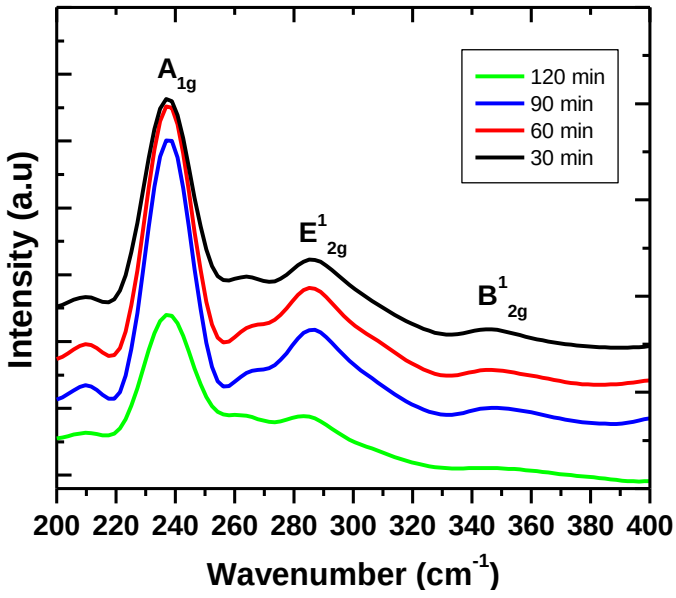

Figure 3.4: Raman spectra of the $MoSe_2$ synthesized at 30, 60, 90 and 120 min.

A shift to a wavenumber of 237 cm^{-1} for the A_{1g} has been found to indicate the formation of few-layer nanosheets.[17] The position of the A_{1g} (237 cm^{-1}) suggests few-layer nanosheets are formed at 60, 90 and 120 which is in agreement with the result in the

PXRD patterns which suggest that the samples collected at 60, 90 and 120 min should be multilayer as indicated by the appearance of the (002). Tonndorf *et al*. have shown that the A_{1g} undergoes a splitting for few-layer nanosheets with layers between 3-5 layers.[16] This splitting of the A_{1g} in the Raman spectra for 30, 60, 90 and 120 min samples is observed further confirming the formation of few-layer nanosheets. The E^1_{2g} of the as synthesized product is situated at 285 cm^{-1} for the samples collected at 30, 60,90 and 120 min which is has shifted from the bulk by 1 cm^{-1}. The position of the E^1_{2g} peak (285 cm^{-1}) is normally found in bilayer nanosheets.[16] In this case it suggests the nanosheets are not monolayer but few-layers. The out of plane B^1_{2g} can also be observed at ~350 cm^{-1}, this peak is not active for a bulk sample and it is not active for monolayer samples but appears for few-layer nanosheets.[16] The appearance of this peak in the 30 min Raman spectrum contradicts the observation made in the PXRD pattern which suggests that monolayer nanosheets have been formed due to the absence of the (002). The shift of the A_{1g} peak from the bulk to ~ 237 cm^{-1} also suggest few-layer nanosheets have been formed at 30 min.

The optical characterisation of the materials was done using UV-Vis absorption spectroscopy. The UV-Vis absorption spectra of the $MoSe_2$ nanosheets show three absorption peaks, the peaks are denoted A, B and C as shown in Fig. 3.5.

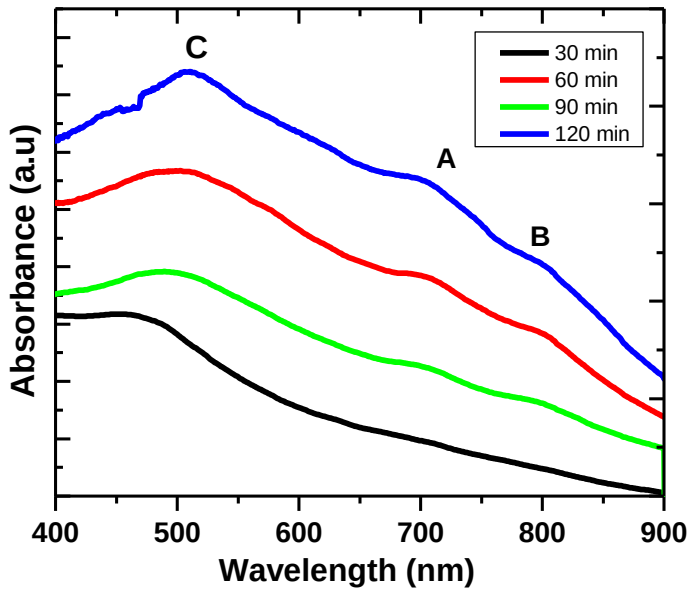

Figure 3.5: The UV-Vis absorption spectra of the as synthesized MoSe2 nanosheets at 30, 60, 90 and120 min.

The first peak at ~ 490 nm (C) is attributed to the optical transitions between the density of states peaks in the valence and conduction bands.[18] There are two exciton absorption peaks that are picked up at 705.6(1.8 eV) and 803.3(1.5 eV) which have been denoted as A and B respectively in agreement with what has been reported in literature.[19-20] The peaks are due to a direct electronic transition at the K-point and they are split due to spin-orbital coupling and coupling between the layers.[21] The band-gap in bulk $MoSe_2$ is ~ 1.1 eV and the band-gap in the as synthesized $MoSe_2$ nanosheets is 1.5 eV. Indicating a band-gap crossover. The band-gap crossover from indirect to direct and the blue-shifting of the band-gap is due to quantum confinement in the $MoSe_2$ nanosheets.[22] The A and B exciton absorption peaks in the 30 min however do not seem to be as prominent. There is no significant shift in the peaks from 60 to 90 min as the reaction progresses which suggests that the optical properties are not strongly dependant on the number of layers on the nanosheets formed between 60 and 120 min.

An initial look at the TEM images of the material synthesized at 30 min shows that the material initially forms a flocculate as shown in Fig. 3.6 (a).

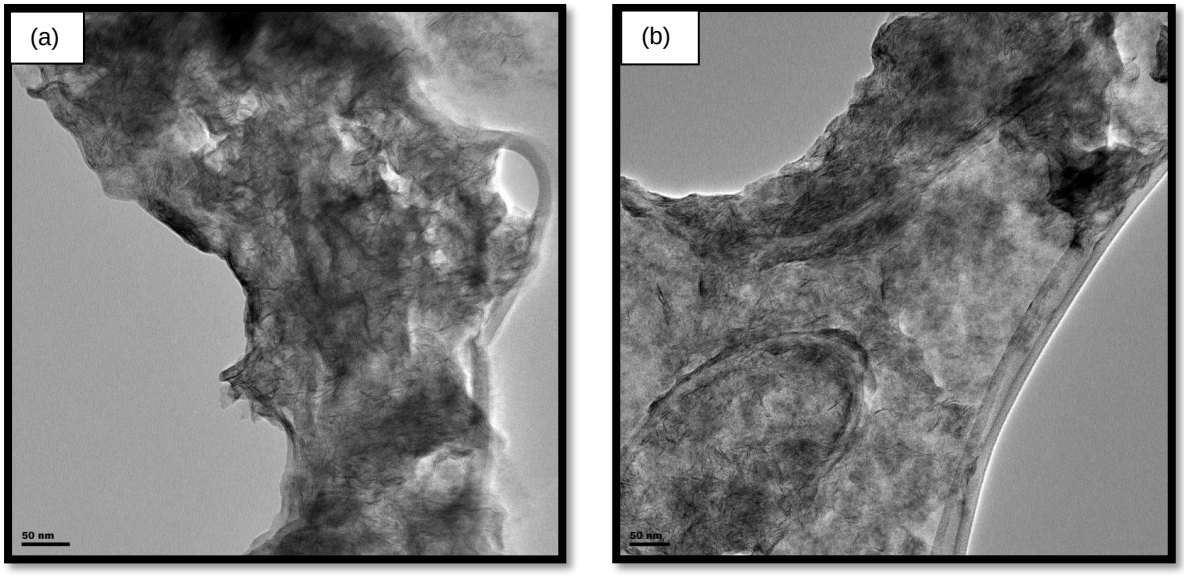

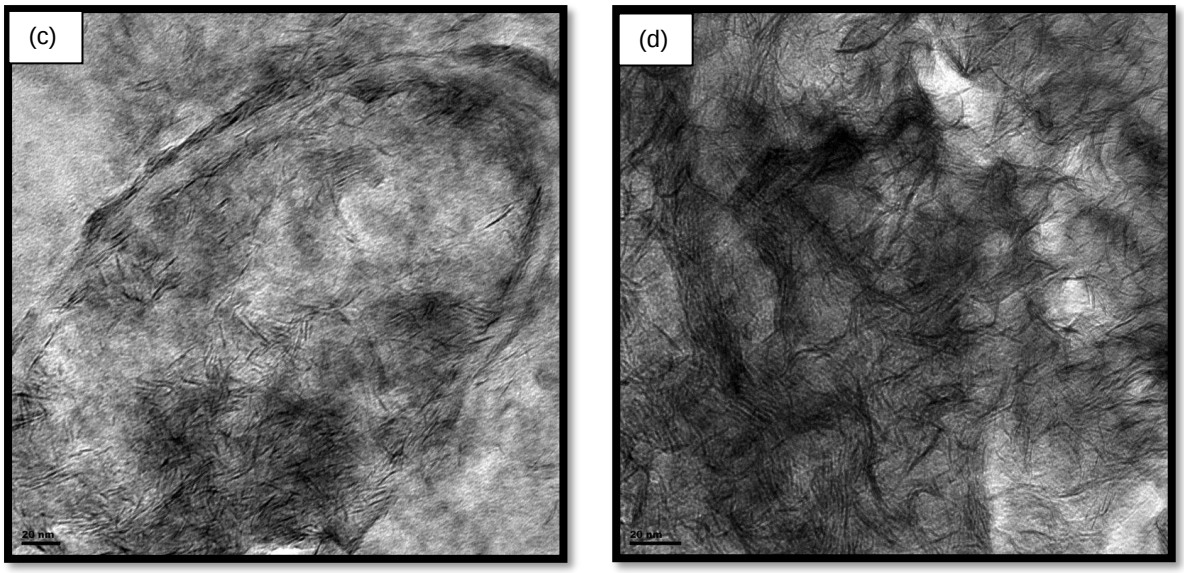

Figure 3.6: TEM images of the $MoSe_2$ nanosheets at the 30 min aliquot(a,b), (c) and (d) are HRTEM images of the sample at 30 min.

These flocculates have also been observed by Savjani *et al.* in the synthesis of MoS_2. The flocculates are known to have lateral dimensions ranging from hundreds to thousands of nanometres. The flocculates seem to mould and blanket the lacey carbon grids as shown in Fig. 3.6 (a, b).[24]These flocculate structures have also been observed by Gao *et al.* in the synthesis of MoS_2 using microwave assisted synthesis. They described the structure as a "reticulated network of amorphous materials where some tiny MoS_2-layered crystals appear".[24] A closer look at the HRTEM in Fig. 3.6 (c) indeed does shows that there are ultrathin nanosheets observed in the flocculates just as Gao *et al.* suggested. The image in Fig. 3.6 (d) shows that the nanosheets have agglomerated to form a network of the nanosheets that are folded in on each other; the nanosheets are randomly oriented and are also highly disordered. At 60 min the flocculate is no longer observed but hierarchical few-layer nanosheets begin to form Fig. 3.7 (a, b).

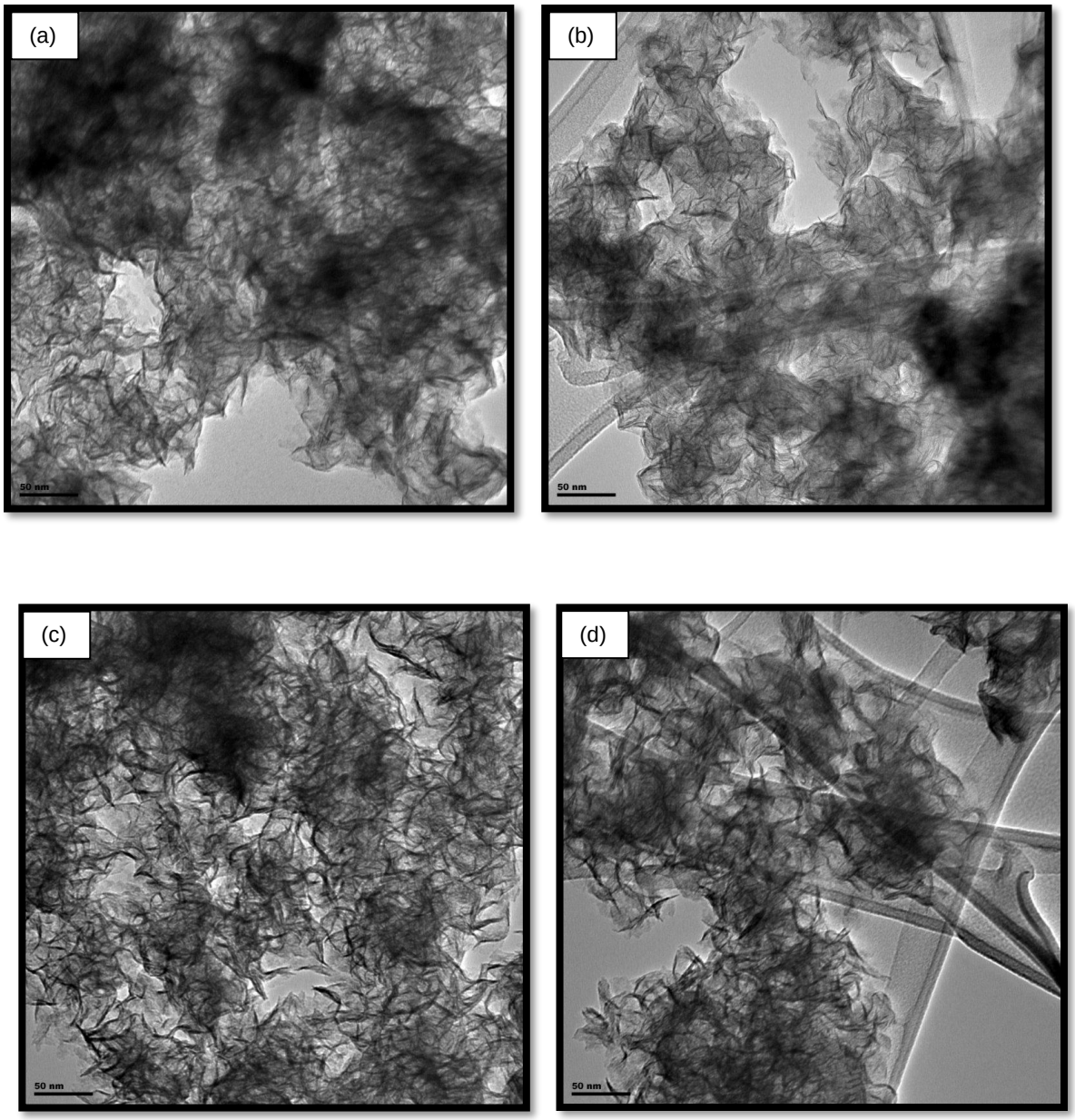

Figure 3.7: The TEM images of the $MoSe_2$ nanosheets: (a,b) are images of the material taken at 60 minutes,(c) images for the products taken at 90 mins and (d) for the product extracted after 120 min.

There is an interesting transition between 30 and 60 min that results in a change of the morphology of the nanosheets. At 30 min flocculates of the material with small ultrathin nanosheets in an oleylamine matrix can be observed. As the reaction continues to run for a longer period the flocculate is gradually phased out to form a network of densely packed hierarchical few-layer nanosheets beginning at 60 min as shown in Fig 3.7 (a, b). This transition continues from 60 to 90 and 120 min as shown in Fig. 3.7 (c, d). This transition suggests that the reaction had not run to completion

at 30 min, this could be due to the slow release of the Mo monomer as the $Mo(CO)_6$ decomposes. The amorphous flocculate which is made up of the monomer from the decomposed precursors is consumed as the reaction is run for longer time periods until the large area hierarchical few-layer nanosheets are formed, a schematic diagram of the process is depicted in Scheme 3.2.

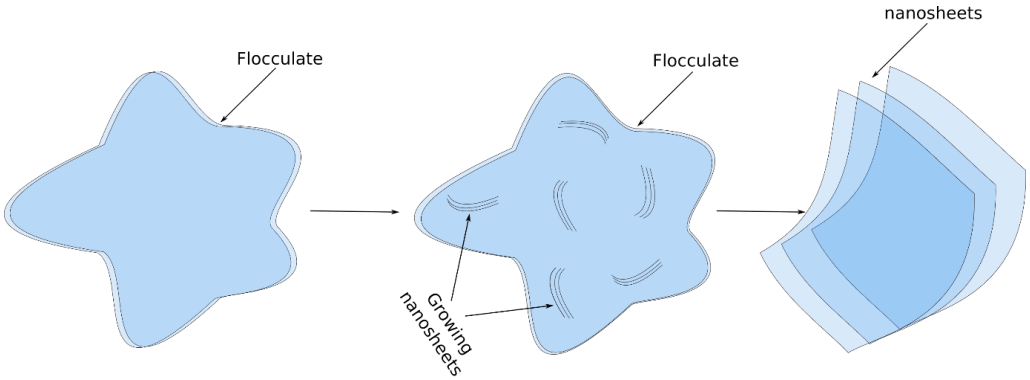

Scheme 3.2: The transition from flocculate material to few layer nanosheets.

The crystallinity and the optical properties of the material are improved as the flocculate is phased out and the few layer nanosheets form, this is shown in the PXRD (Fig. 3.3) and the UV-Vis absorption spectra (Fig. 3.5) of the products extracted at different time periods. This phenomenon was also observed by Gao *et al*. They were able to form few layer nanosheets from the flocculate by increasing the reaction temperature in their microwave synthesis reaction when synthesizing MoS_2 nanosheets. Gao *et al.* suggested that the few layer nanosheets are formed by consuming the amorphous material in the flocculates as suggested in the process described in this synthetic method.[18] However, in this work it has been proven that the few layer nanosheets form and grow from the flocculates at 300 ˚C just by increasing the reaction time from 30 to 60 min, which suggest that the temperature at which the reaction is run is suitable for the synthesis of the material but longer reaction times are needed for the reaction to run to completion.

The nanosheets tend to curl up to form standing edges, the d-spacing between the lattice fringes of these standing edges is ~ 0.65 nm. This is the interlayer distance in multilayer nanosheets corresponding to the d-spacing of the (002) peak. This is depicted in Fig. 3.8.[10]

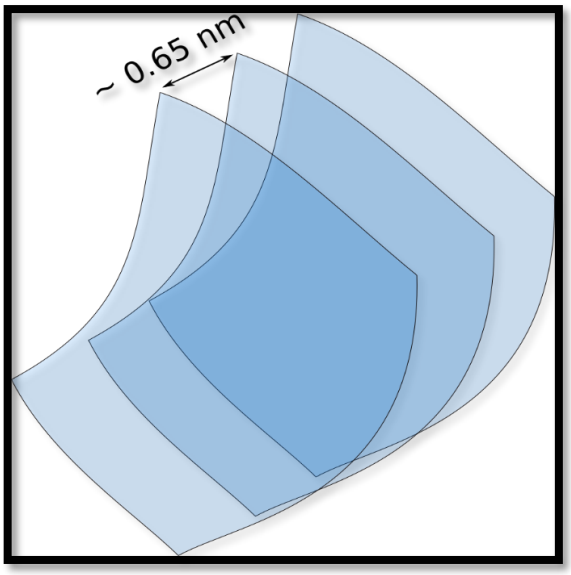

Figure 3.8: Few-layer nanosheets with standing edges showing the d-spacing between the nanosheets.

The HRTEM image displayed in Fig. 3.9(a, b, c and d) shows the d-spacing of the lattice fringes, a d-spacing of ~ 0.66 nm was measured for the lattice fringes of the nanosheets synthesized at 30,60,90 and 120 min respectively. Confirming the formation of multilayer nanosheets.

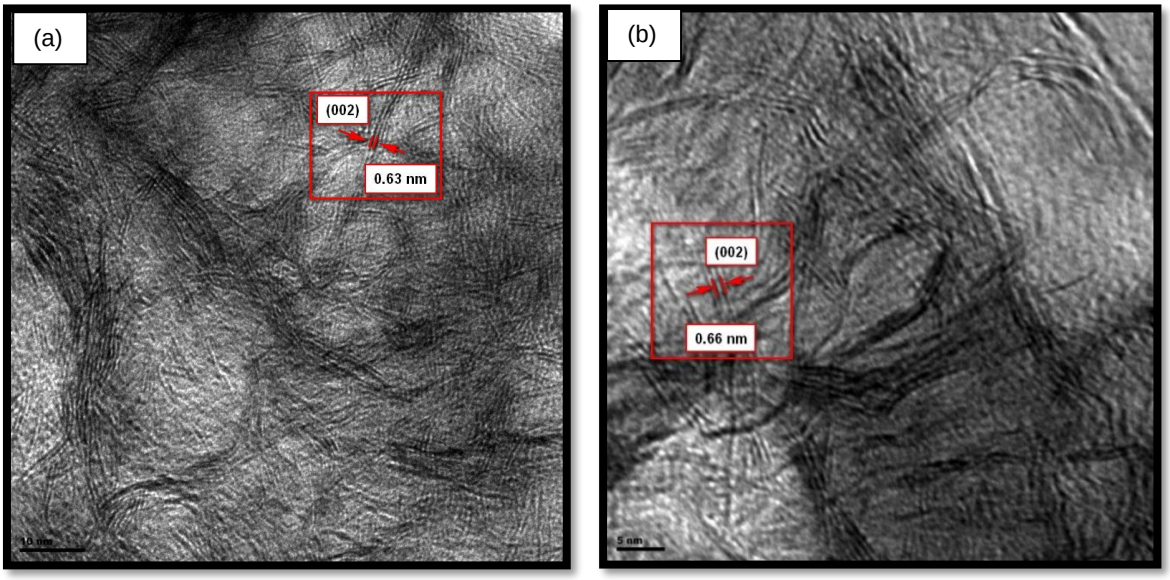

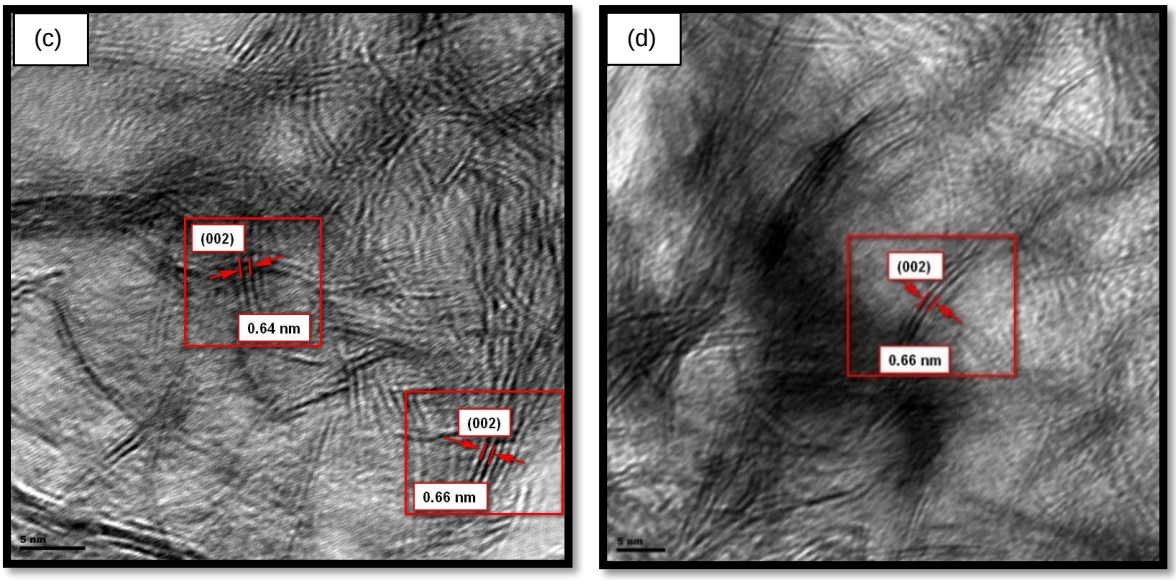

Figure 3.9: HRTEM images of nanosheets synthesized at 30,60, 90 and 120 min respectively, showing the interlayer spacing of the nanosheets.

Contrary to the analysis of the PXRD diffraction pattern the HRTEM analysis suggests that the nanosheets produced at 30 min are multilayer and not monolayer. This result is also confirmed by analysis of the Raman spectra of the 30 min sample.

3.4 Conclusion

In conclusion, a colloidal synthetic method has been developed for the synthesis of few layer hierarchical nanosheets of $MoSe_2$. The synthesis results in the formation of flocculates consisting of small ultrathin nanosheets at 30 min. At longer reaction times, the growth of the nanosheets in the flocculates results in the formation of the network of wrinkled hierarchical few-layer nanosheets. The crystallinity and the optical properties of the synthesized nanomaterials are improved by prolonging the reaction time. The red-shift of the A_{1g} peak in the Raman spectrum and the HRTEM analysis of the nanomaterials at 30 min shows that the nanosheets synthesized at 30 min are definitely multilayer contrary to what the PXRD analysis revealed. The samples extracted at 60, 90 and 120 min also form few-layer nanosheets. The optical properties of the material do not seem to be significantly affected by prolonging the reaction time from 60 to 120 min. The band-gap does not change from the samples extracted at 60 min to those extracted at 120 min.

3.5 References

1. Choi, W.; Choudhary, N.; Han, G. H.; Park, J.; Akinwande, D.; Lee, Y. H., Recent development of two-dimensional transition metal dichalcogenides and their applications. *Materials Today* **2017**, 20(3), 116-130.
2. Wang, T.; Zhu, H.; Zhuo, J.; Zhu, Z.; Papakonstantinou, P.; Lubarsky, G.; Lin, J.; Li, M., Biosensor based on ultrasmall MoS_2 nanoparticles for electrochemical detection of H_2O_2 released by cells at the nanomolar level. *Analytical chemistry* **2013,** *85* (21), 10289-10295.
3. Jin, Z.; Zhang, M.; Wang, M.; Feng, C.; Wang, Z.-S., Metal Selenides as Efficient Counter Electrodes for Dye-Sensitized Solar Cells. *Accounts of Chemical Research* **2017,** *50* (4), 895-904.
4. Balasingam, S. K.; Lee, J. S.; Jun, Y., Few-layered MoSe 2 nanosheets as an advanced electrode material for supercapacitors. *Dalton Transactions* **2015,** *44* (35), 15491-15498.
5. Charitidis, C. A.; Georgiou, P.; Koklioti, M. A.; Trompeta, A.-F.; Markakis, V., Manufacturing nanomaterials: from research to industry. *Manufacturing Review* **2014,** *1*(11), 1-19.
6. Li, X.; Zhu, H., Two-dimensional MoS_2: Properties, preparation, and applications. *Journal of Materiomics* **2015,** *1* (1), 33-44.
7. Strouse, G. F.; Gerbec, J. A.; Magana, D., Method for synthesis of colloidal nanoparticles. Google Patents: 2011.
8. Son, J. S.; Wen, X. D.; Joo, J.; Chae, J.; Baek, S. i.; Park, K.; Kim, J. H.; An, K.; Yu, J. H.; Kwon, S. G., Large-Scale Soft Colloidal Template Synthesis of 1.4 nm Thick CdSe Nanosheets. *Angewandte Chemie* **2009,** *121* (37), 6993-6996.
9. Berends, A. C.; Meeldijk, J. D.; van Huis, M. A.; de Mello Donegá, C., Formation of colloidal copper indium sulfide nanosheets by two-dimensional self-organization. *Chemistry of Materials* **2017**, 29, 10551-10560.
10. Zhou, M.; Zhang, Z.; Huang, K.; Shi, Z.; Xie, R.; Yang, W., Colloidal preparation and electrocatalytic hydrogen production of MoS 2 and WS 2 nanosheets with controllable lateral sizes and layer numbers. *Nanoscale* **2016,** *8* (33), 15262-15272.
11. Sun, D.; Feng, S.; Terrones, M.; Schaak, R. E., Formation and interlayer decoupling of colloidal MoSe2 nanoflowers. *Chemistry of Materials* **2015,** *27* (8), 3167-3175.

12. Wang, Z. D.; Yoshida, M.; George, B., Theoretical study on the thermal decomposition of thiourea. *Computational and Theoretical Chemistry* **2013,** *1017*, 91-98.
13. Liu, L.; Peng, Q.; Li, Y., Preparation of monodisperse Se colloid spheres and Se nanowires using Na_2SeSO_3 as precursor. *Nano Research* **2008,** *1* (5), 403-411.
14. Lee, J. S.; Boudart, M., In situ carburization of metallic molybdenum during catalytic reactions of carbon-containing gases. *Catalysis letters* **1993,** *20* (1), 97-106.
15. Jung, W.; Lee, S.; Yoo, D.; Jeong, S.; Miró, P.; Kuc, A.; Heine, T.; Cheon, J., Colloidal synthesis of single-layer MSe_2 (M= Mo, W) nanosheets via anisotropic solution-phase growth approach. *Journal of the American Chemical Society* **2015,** *137* (23), 7266-7269.
16. Tonndorf, P.; Schmidt, R.; Böttger, P.; Zhang, X.; Börner, J.; Liebig, A.; Albrecht, M.; Kloc, C.; Gordan, O.; Zahn, D. R., Photoluminescence emission and Raman response of monolayer MoS_2, $MoSe_2$, and WSe_2. *Optics express* **2013,** *21* (4), 4908-4916.
17. Mishra, A. K.; Lakshmi, K.; Huang, L., Eco-friendly synthesis of metal dichalcogenides nanosheets and their environmental remediation potential driven by visible light. *Scientific reports* **2015,** *5*(15718), 1-8.
18. Dong, N.; Li, Y.; Feng, Y.; Zhang, S.; Zhang, X.; Chang, C.; Fan, J.; Zhang, L.; Wang, J., Optical limiting and theoretical modelling of layered transition metal dichalcogenide nanosheets. *Scientific reports* **2015,** 5(14646), 1-10.
19. Hussain, S.; Patil, S. A.; Vikraman, D.; Liu, H.; Kim, H.-S.; Jung, J., High Performance $MoSe_2$/Mo Counter Electrodes Based-Dye-Sensitized Solar Cells. *Journal of The Electrochemical Society* **2017,** *164* (2), E11-E16.
20. Coehoorn, R.; Haas, C.; De Groot, R., Electronic structure of $MoSe_2$, MoS_2, and WSe_2. II. The nature of the optical band gaps. *Physical Review B* **1987,** *35* (12), 6203-6206.
21. Tongay, S.; Zhou, J.; Ataca, C.; Lo, K.; Matthews, T. S.; Li, J.; Grossman, J. C.; Wu, J., Thermally driven crossover from indirect toward direct bandgap in 2D semiconductors: $MoSe_2$ versus MoS_2. *Nano letters* **2012,** *12* (11), 5576-5580.
22. Savjani, N.; Lewis, E. A.; Bissett, M. A.; Brent, J. R.; Dryfe, R. A.; Haigh, S. J.; O'Brien, P., Synthesis of Lateral Size-Controlled Monolayer 1 H-MoS_2@

Oleylamine as Supercapacitor Electrodes. *Chemistry of Materials* **2016,** *28* (2), 657-664.

23. Gao, M.-R.; Chan, M. K.; Sun, Y., Edge-terminated molybdenum disulfide with a 9.4-Å interlayer spacing for electrochemical hydrogen production. *Nature communications* **2015,** *6*(7493), 1-8.
24. Altavilla, C.; Sarno, M.; Ciambelli, P., A Novel Wet Chemistry Approach for the Synthesis of Hybrid 2D Free-Floating Single or Multilayer Nanosheets of MS_2@ oleylamine (M= Mo, W). *Chemistry of Materials* **2011,** *23* (17), 3879-3885.

Chapter 4: Colloidal synthesis of $MoSe_2$ using various Mo precursors

4.1 Introduction

There are several parameters in the colloidal synthesis of nanomaterials that determine the structure, morphology and properties of the synthesized nanomaterials. Colloidal synthesis relies on chemical processes such as chemical reduction or thermal decomposition to break down precursors into the monomers needed to form the desired nanoparticles. How readily the precursors are broken down into the required monomers can affect various properties of the synthesized nanomaterials such as the size and morphology of the nanoparticles. An important parameter for colloidal synthesis of nanomaterials is therefore the choice of precursors.[1] These precursors are normally considered as complexes of a metal bound to some ligand. The reactivity of the monomer or how readily the precursor can be broken down to produce free monomer is determined by how strongly the ligands bind to the metal.[2] The use of highly reactive precursors can lead to high nucleation and growth rates that result in low yield of nanoparticles that have broad size distribution. The use of low reactivity monomer can lead to the same result going through a different pathway.[2] Moderately reactive monomer is desired because there is a balance in the rate of nucleation and growth after the burst nucleation step leading to a high yield of nanoparticles with a narrow size distribution. The nucleation and growth processes that are affected by the reactivity of the precursors have an effect on the structure, morphology and properties of the synthesized nanomaterials.[3] This has been shown in work by Sayed *et al.* who have been able to synthesize six different morphologies of iron oxide using the same synthesis procedure but with different Iron salts.[4] The morphologies range from spherical nanoparticles, rods, cubes and flowers. Barreto *et al.* have also shown that by using different Zn^{2+} precursors in the synthesis of ZnO one can control the size of the synthesized ZnO nanoparticles.[5] Rosendo *et al.* also shown that the morphology of CdSe nanoparticles can be controlled using different cadmium precursors. In this work the effect of changing the metal precursor from molybdenum hexacarbonyl ($Mo(CO)_6$) to molybdic acid(H_2MoO_3) was investigated.[6] There are two different precursors that were used which are $Mo(CO)_6$ and H_2MoO_4. The ligands that bind to the Mo monomer in molybdenum hexacarbonyl are carbonyl ligands (-CO) and the ligands in molybdic acid are oxygen(=O) and hydroxyl ligands (-OH).[7] Molybdenum

hexacarbonyl is known to have a relatively low decomposition temperature, the decomposition reaction is known to result in the decarbonylation of the Mo atom. Molybdic acid on the other hand is thought to undergo a dehydration at elevated temperatures which leads to the formation of MoO_3.[8] The low decomposition temperature of $Mo(CO)_6$ yielding the Mo atom monomer at low temperature suggest that $Mo(CO)_6$ would readily form the desired nanomaterials. H_2MoO_4 on the other hand decomposes to MoO_3 at high temperature may not readily form the desired nanomaterials. The difference in reactivity of the two precursors may lead to differences in the nucleation mechanism when the $MoSe_2$ nanomaterials are formed. The effect of using these two different precursors on the properties of the synthesized nanomaterials will be discussed.

4.2 Materials and methods

4.2.1 Chemicals

Molybdic acid ((H_2MoO_4), 85%, Sigma-Aldrich), selenourea (CH_4N_2Se, 98%, Sigma-Aldrich) and oleylamine (OAm, 70%, Sigma-Aldich) were used as received without purification.

4.2.2 Synthesis of $MoSe_2$ using $Mo(CO)_6$ ($MoSe_2$-$Mo(CO)_6$)

A three-neck round bottom flask was filled with 20 ml of oleylamine and the mixture was degassed for 20 minutes under N_2 using a Schlenk line. The temperature was increased to 50 ^oC and 0.362 g (0.249 mmol) of selenourea was added to the reaction mixture and stirred for 10 mins. Molybdenum hexacarbonyl (0.212 g (0.802 mmol)) was added once the reaction temperature reached 220 ^oC, the temperature was then increased until the desired temperature of 300 ^oC was reached. The reaction was allowed to continue for 90 mins, after which the product was collected and washed with toluene and ethanol by centrifugation.

4.2.3 Synthesis of $MoSe_2$ using H_2MoO_4 ($MoSe_2$-H_2MoO_4)

A three-neck round bottom flask was filled with 20 ml of oleylamine and the mixture was degassed for 20 minutes under N_2 using a Schlenk line. The temperature was increased to 50 ^oC and 0.378 g (3.07 mmol) of selenourea was added to the reaction mixture and stirred for 10 mins. Molybdic acid (0.230 g (1.42 mmol)) was added once

the reaction temperature reached 220 ^{o}C, the temperature was then increased until the desired temperature of 300 ^{o}C was reached. The reaction was allowed to continue for 90 mins, after which the product was collected and washed with toluene and ethanol by centrifugation.

4.2.4 Characterisation techniques

The structural properties were investigated using powder X-ray diffraction(PXRD) and Raman spectroscopy. The phase purity, crystallinity and preferred crystal orientation of the products were examined by using XRD on a Bruker MeasSrv (D2-205530)/D2-205530 diffractometer using secondary graphite monochromated CoKα radiation (λ 1.78897 Å) at 30 kV/30 mA. Measurements were taken using a glancing angle of incidence detector at an angle of 2°, for 2θ values over 10 - 90° in steps of 0.026° with a step time of 37 s and at a temperature of 25 °C. Raman spectroscopy (J-Y T64000 micro-Raman spectrometer, Horiba Jobin-Yvon, Ltd., Stanmore, UK) equipped with a liquid nitrogen cooled charge coupled device detector. All samples were measured after excitation with a laser wavelength of 514.5 nm. The optical properties were determined using a Varian Cary Eclipse (Cary 50) UV-vis absorption spectrophotometer.The sample sizes and morphologies were determined by the transmission electron microscopy (TEM) carried out on a FEI Technai T12 TEM microscopy operated at an acceleration voltage of 200 kV with a beam spot size of 20 - 100 nm in TEM mode. HRTEM images were obtained from a JEOL JEM-2100 microscopy with a LAB6 filament and an EDS detector, operated at 200 kV.

4.3 Results and discussion

The composition, phase and crystallinity of the synthesized nanostructures were determined using powder X-ray diffraction. The diffraction patterns of the nanostructures synthesized using the two precursors are shown in Fig. 4.1. The diffraction patterns of $MoSe_2$ using the two molybdenum precursors confirm the formation of 2H hexagonal $MoSe_2$ nanomaterials (JCPDS. The (002) peak arises due to the stacking of the layers in multilayer nanosheets.[9] The appearance of the (002) peak in both diffraction patterns suggests the formation of multilayer $MoSe_2$ nanosheets.[10]

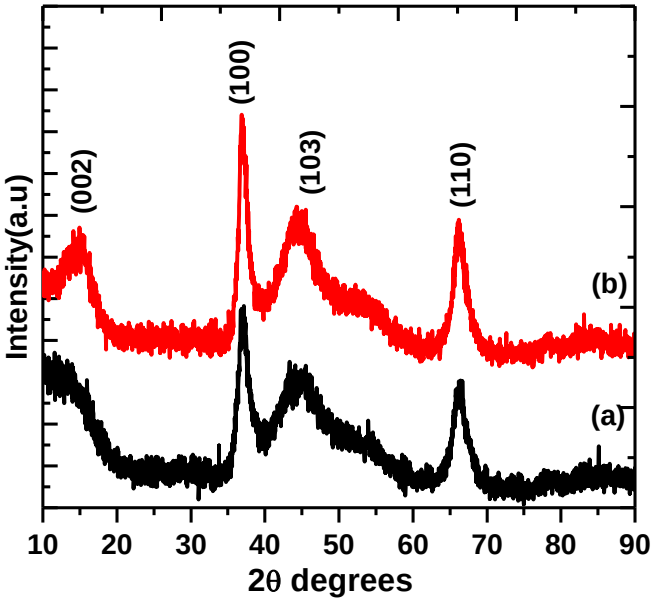

Figure 4.1: Powder pattern of $MoSe_2$; (a) synthesized from using $Mo(CO)_6$ as the molybdenum precursor and (b) synthesized H_2MoO_4 as the molybdenum precursor.

The nature of the of the nanomaterials synthesized using $Mo(CO)_6$ at 90 min have been found to be few-layer nanosheets in a previous study (chapter 3), this has also been reported by Gao et al who synthesized a nanonetwork of $MoSe_2$ few-layer nanosheets using $Mo(CO)_6$ using oleylamine as the surfactant. The appearance of the (002) peak in the diffraction pattern for the $MoSe_2$-H_2MoO_4 nanostructures also suggests that multilayer nanosheets of the material have been formed.[10] This means that the change in precursor does not significantly change the layer number on the nanosheets; the nanosheets do not change to be monolayer and do not seem to change to the bulk counterpart either. The composition and the phase of the materials also seem to be unaffected by the change in the metal precursor. Raman spectroscopy is used to further confirm the formation of $MoSe_2$ nanomaterials and to also approximate the number layers on the nanosheets formed.

The Raman spectrum of $MoSe_2$ has two main characteristic peaks which are the out of plane A_{1g} and the in plane E^1_{2g}, the mono or few-layer nanomaterials are identified by the red-shift of the A_{1g} and the blue-shift of the E^1_{2g} from the bulk material.[11] The Raman Spectra of $MoSe_2$-$Mo(CO)_6$ and $MoSe_2$-H_2MoO_4 are shown in Fig. 4.2.

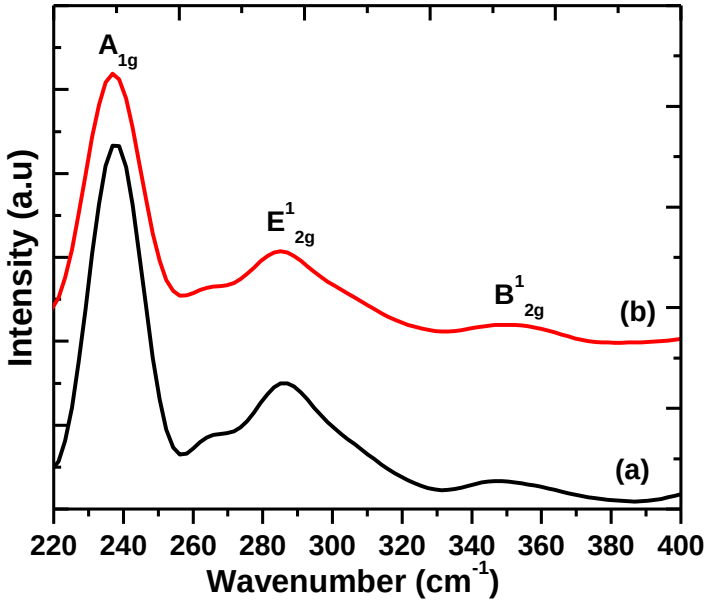

Figure 4.2: Raman spectra of (a) $MoSe_2$-$Mo(CO)_6$ and (b) $MoSe_2$-H_2MoO_4 nanomaterials.

The appearance of the characteristic out of plane A_{1g} and in plane E^1_{2g} bands in the Raman spectrum Fig. 4.2 confirm the formation of $MoSe_2$. The A_{1g} appears at ~242 cm^{-1} in the bulk and the E^1_{2g} appears at ~286 cm^{-1}.[11] The Raman spectrum of $MoSe_2$-H_2MoO_4 shows the A_{1g} has red shifted from the bulk to 237 cm^{-1}. This position is normally associated with the formation few-layer nanosheets.[12] The A_{1g} for $MoSe_2$-$Mo(CO)_6$ has red-shifted from the bulk to 237 cm^{-1} as well. The E^1_{2g} has shifted to 285 cm^{-1}, this is particular shift has been observed for bi-layer nanosheets of $MoSe_2$.[11] There is one other characteristic peak observed in the Raman spectra, the B^1_{2g}.This peak only appears for few-layer nanosheets with a layer number between 2-5 layers. The appearance of the B^1_{2g} peak at ~ 350 cm^{-1} suggests that the nanosheets are actually few-layer, the peak does not appear for bulk or monolayer nanosheets.[11] This confirms the result found in the PXRD analysis that few-layer nanosheets have been formed using both the metal precursors. This confirms that regardless of the precursor used few-layer nanosheets are formed.

The UV-Vis spectrum of mono or few-layer nanosheets has been reported to show two exciton absorption peaks which are normally denoted A and B. The peaks are normally found at around 700 and 800 nm for A and B respectively.[13] There is another peak normally found at ~ 400 nm which is due to with optical transitions between the density

of states peaks in the valance and conduction bands.[13] The UV-Vis absorption spectrum of the synthesized materials from both precursors has two absorption bands as shown in Fig. 4.3. The bands are at 714.1 and 801.3 nm for $MoSe_2$-$Mo(CO)_6$, for $MoSe_2$-H_2MoO_4 the exciton absorption peaks are found at 727.2 and 812.4 nm. The band-gap of the material is taken from the absorption peak with the longest wavelength. The band-gap of $MoSe_2$-$Mo(CO)_6$ is ~ 1.55 eV and from $MoSe_2$-H_2MoO_4 the band-gap is ~ 1.53 eV. The blue-shift of the band-gap from ~ 1.09 eV in the bulk is confirmation of the formation of few-layer nanosheets.[14] This result is already confirmed by PXRD and Raman analysis.

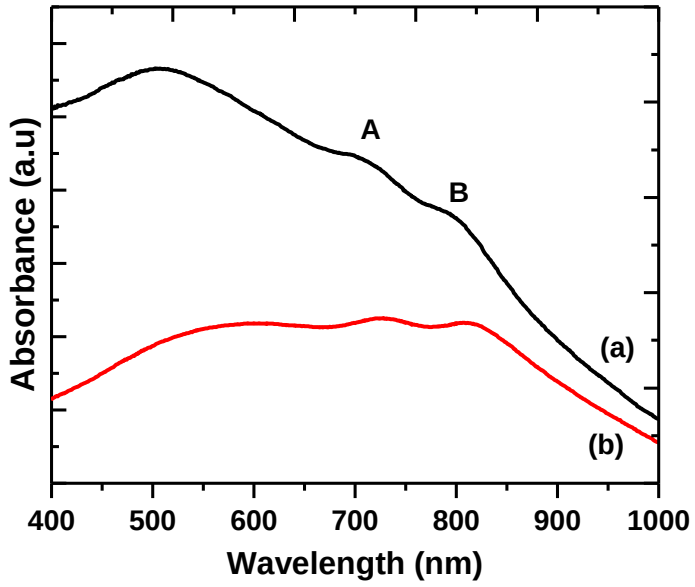

Figure 4.3: UV-Vis absorption spectra of $MoSe_2$ nanomaterials: (a) The UV-Vis absorption spectrum of the $MoSe_2$ nanomaterials($MoSe_2$-$Mo(CO)_6$) synthesized using $Mo(CO)_6$ and (b) The UV-Vis absorption spectrum of $MoSe_2$ nanomaterials($MoSe_2$-H_2MoO_4) synthesized using H_2MoO_4.

As the nanosheets of both precursor have a band-gap of 1.5 eV this suggests that the change in metal precursor does not significantly change the optical properties of the nanomaterials.

Two electron microscopy methods namely: Scanning electron microscopy (SEM) and transmission electron microscopy (TEM) have been used to investigate the change in morphology of the materials as the metal precursor in changed from $Mo(CO)_6$ to

H_2MoO_4. The SEM micrographs show the major structural differences in the nanosheets synthesized using the two precursors. The micrographs of $MoSe_2$-$Mo(CO)_6$ shown in Fig. 4.4(b) show nanosheet like structures that seem to have a corrugated architecture. The micrographs of the $MoSe_2$-H_2MoO_3 shown in Fig. 4.4(a) show discrete nanosheets with a flower like morphology that seem to have agglomerated and oriented themselves in different directions.

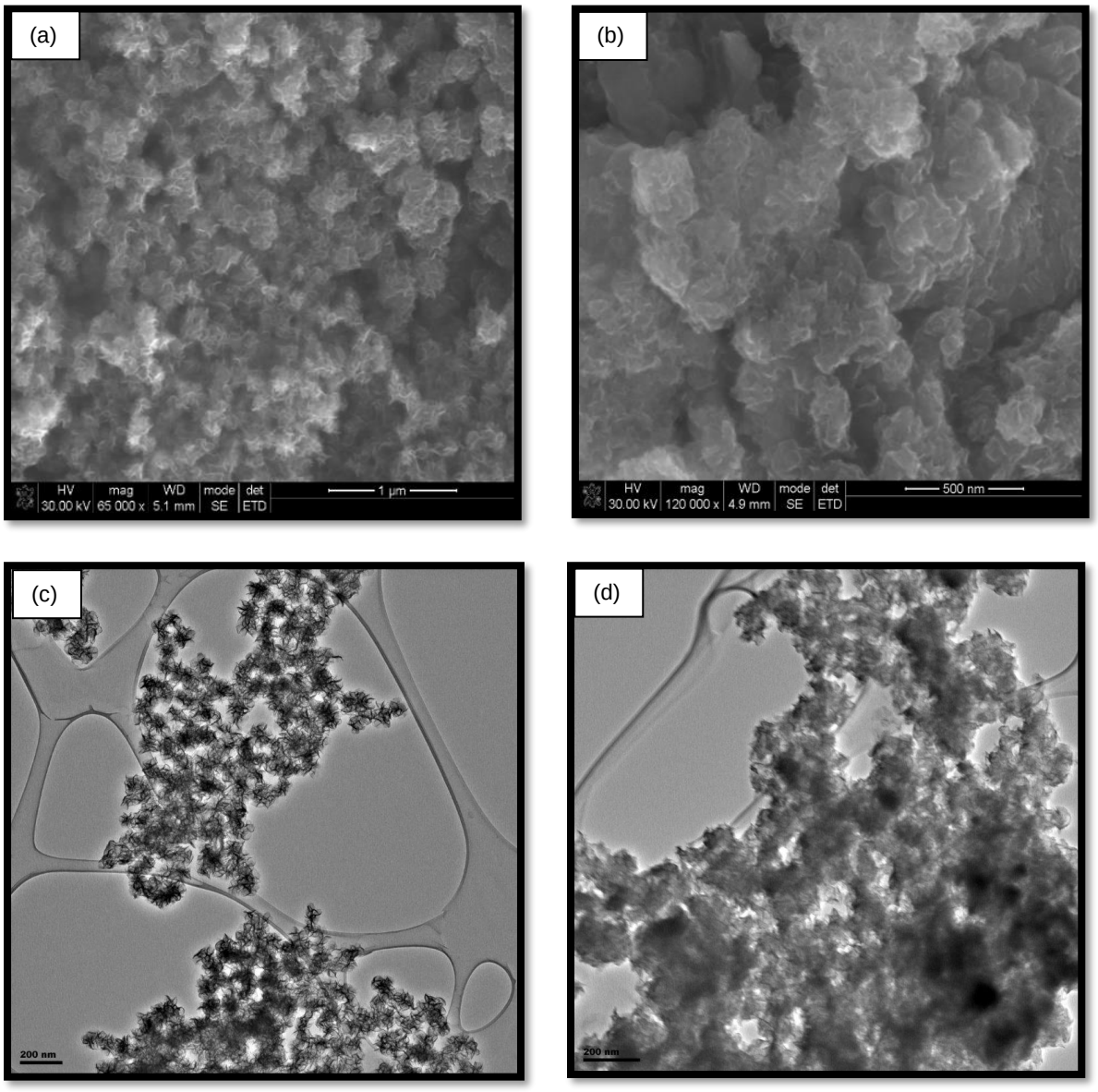

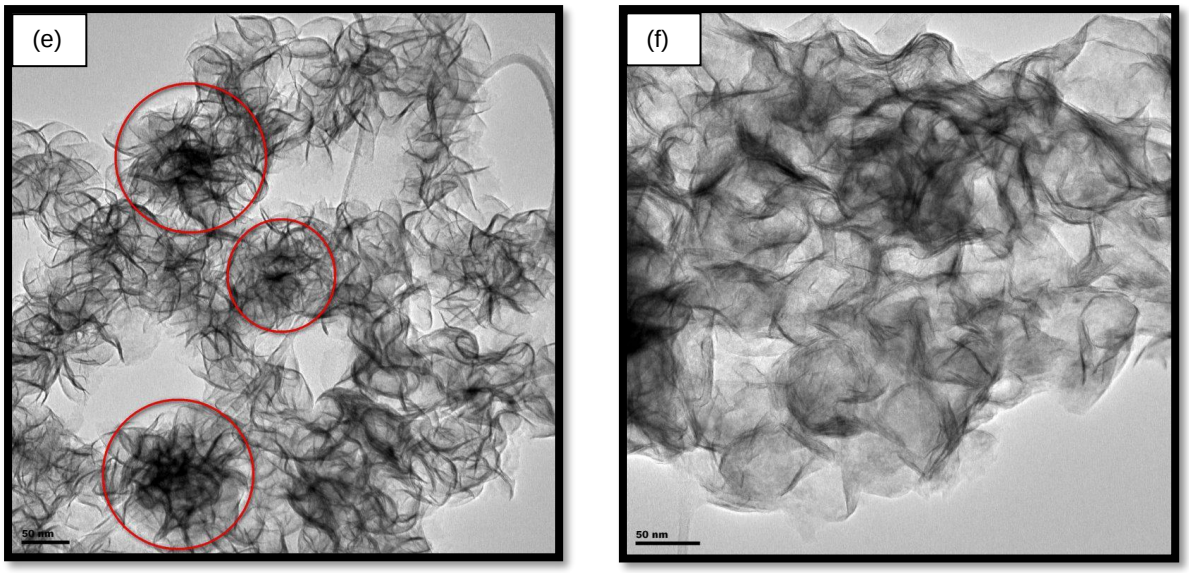

Figure 4.4: (a) and (d) are the SEM images of the $MoSe_2$ nanosheets synthesized from H_2MoO_4 and $Mo(CO)_6$ respectively. (c) and (e) are the TEM images of the $MoSe_2$ nanosheets synthesized from H_2MoO_4. (d) and (f) are the TEM images of the $MoSe_2$ nanosheets synthesized from $Mo(CO)_6$.

The TEM images of the nanosheets produced from $Mo(CO)_6$ show the formation of wrinkled large area few-layer nanosheets as shown in Fig. 4.4(f), the few-layer nanosheets grow from a flocculate that is formed from starting materials as shown in Fig. 4.4(d). The $MoSe_2$ nanomaterials formed using H_2MoO_4 seem to favour the formation of a flower like morphology as shown in Fig. 4.4(c). The nanomaterials with a flower like morphology seem to contain a central core as shown in Fig. 4.4(e) by the red circles. The nanosheets that are formed using $Mo(CO)_6$ seems to have large lateral dimensions which are dictated by the large lateral dimensions of the flocculate material they grow from.[15] The nanoflowers on the other hand seem to be formed by small lateral dimension nanosheets that grow from the dense central core randomly in all direction resembling a blooming flower. The $Mo(CO)_6$ which has been discussed in length in the previous work (chapter 3) undergoes decarbonylation when introduced into the reaction mixture at 250 ^oC. A flocculate is formed after the introduction of the $Mo(CO)_6$ and few-layer nanosheets grow from the flocculate as the reaction progresses.[15] The formation of the flocculate seems to affect the morphology of the synthesized nanomaterials. The flocculate is known to have large lateral dimensions up to a thousand nanometres. The nanosheets that grow from this flocculate seem to form what Gao *et al.* described as a nanonetwork of few-layer $MoSe_2$ nanosheets.

Gao et al also used $Mo(CO)_6$ as the metal precursor with oleylamine as the surfactant. They were able to study the initial stages of the reaction between the $Mo(CO)_6$ and a selenium precursor in oleylamine.[16] They show in their TEM images the formation of the flocculate. They show that the $Mo(CO)_6$ decomposes to Mo atoms at 200 ^oC, the introduction of the selenium precursor forms the flocculate. The nanonetwork of the $MoSe_2$ few-layer nanosheets they describe is formed from the flocculate. The use of H_2MoO_4 on the other hand had not been studied in the synthesis of $MoSe_2$ nanomaterials. The formation of nanoflowers has been shown by Sun *et al.* to result from the formation of a central core. The nanosheets grow randomly outward from this central core in a fashion closely resembling a blooming flower.[16] The growth of the nanoflowers in this study using H_2MoO_4 is thought to undergo the same process. The slight difference in the morphology of the nanomaterials using the two different metal precursors could be due to the difference in the formation pathway. The use of $Mo(CO)_6$ resulting in the network of overlapping few-layer nanosheets through the formation of the flocculate and the use of H_2MoO_4 resulting in the formation of nanoflowers through the formation of the central core. To further investigate the morphology of the $MoSe_2$-H_2MoO_4 at the initial stages SEM images of a sample taken 10 min into the reaction were obtained as shown in Fig. 4.5 (a) and (b).

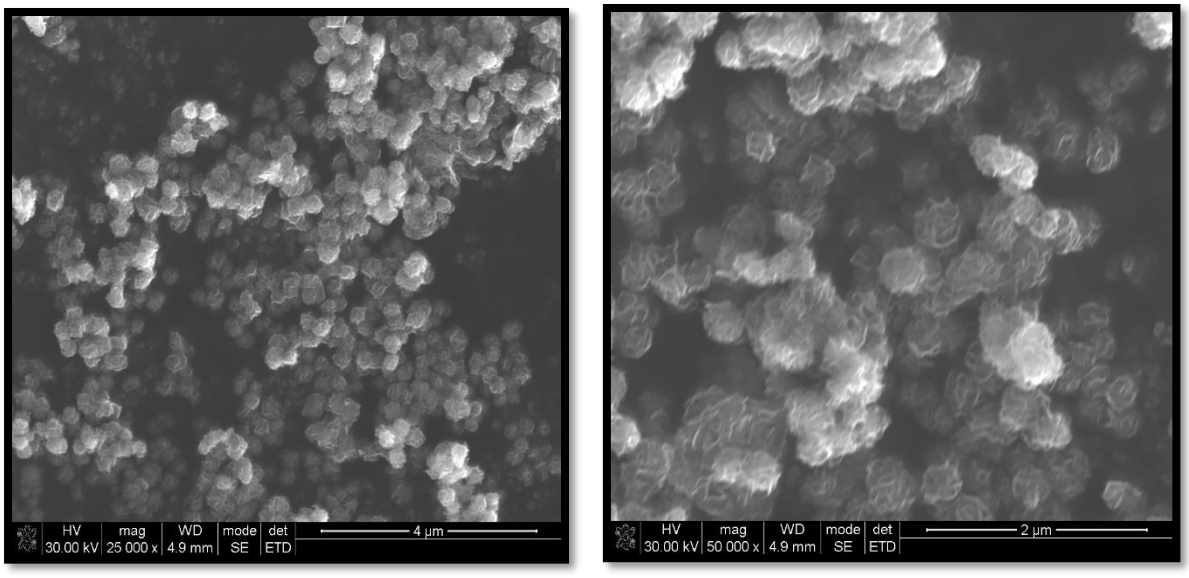

Figure 4.5: The SEM images (a) and (b) show the morphology of the $MoSe_2$-H_2MoO_4 nanomaterials at the initial stages of the reaction (reaction after 10 min).

H_2MoO_4 has been known to undergo a dehydration to form MoO_3. Investigation of the product obtained by heating molybdic acid in oleylamine at 300 ^oC yielded a PXRD pattern that was characteristic of an amorphous material as shown in Fig. A4.1.[8] MoO_3 is a crystalline material thus the product could not be MoO_3, MoO_2 was also ruled out as it is also a crystalline material.[17] The product was found to be a mixture of MoO_4^{2-} and the oleylamine surfactant, this was confirmed by FTIR shown in Fig. A4.2.[18]The FTIR spectra shows the characteristic antisymmetric stretching vibration of Mo-O-Mo in MoO_4^{2-} at 827 cm^{-1}.[18] The anion has been shown to react to react with S^{2-} in the synthesis of MoS_2 to form the intermediate MoS_4^{2-} which converts to the MoS_2 as the Mo(VI) is reduced to Mo(IV).[19-20] As the properties of Se and S are similar it is possible that the same phenomenon occurs in the formation of $MoSe_2$. The MoO_4^{2-} may readily react with the Se^{2-} to form the $MoSe_4^{2-}$ which would then convert to $MoSe_2$ upon the reduction of Mo(VI) to Mo(VI). This rapid formation of the central core then results in the formation of the nanoflowers with the nanosheets growing outwardly simulating the behaviour of a blooming flower.

4.4 Conclusion

The study shows that $MoSe_2$ can be synthesized using molybdic acid, the phase and crystallinity of the $MoSe_2$ nanomaterials is not altered by the change in the metal precursor. The band-gap of the material is also not significantly affected as the band-gap of the nanomaterials synthesized using both metal precursors is ~ 1.5 eV. The effect of changing the metal precursor however does affect the morphology of the synthesized nanomaterial because of a difference in the reaction pathway or mechanism. The synthesis of the $MoSe_2$ using $Mo(CO)_6$ results in the formation of large area few-layer nanosheets through the formation of a flocculate in the initial stages of the reaction. On the other hand, the use of H_2MoO_4 as the metal precursor results in the formation of $MoSe_2$ nanomaterials with a flower like morphology due to the formation of a central core at the initial stages of the reaction.[21] The use of H_2MoO_4 may be more for favourable for the synthesis of $MoSe_2$ because it results in nanoflowers which have been shown to be a desirable morphology for supercapacitor electrodes.

4.5 References

1. Frenette, L. C.; Krauss, T. D., Uncovering active precursors in colloidal quantum dot synthesis. *Nature communications* **2017,** *8* (1), 2082, 1-8.
2. van Embden, J.; Chesman, A. S.; Jasieniak, J. J., The heat-up synthesis of colloidal nanocrystals. *Chemistry of Materials* **2015,** *27* (7), 2246-2285.
3. Harris, D. K.; Bawendi, M. G., Improved precursor chemistry for the synthesis of iii–v quantum dots. *Journal of the American Chemical Society* **2012,** *134* (50), 20211-20213.
4. Sayed, F. N.; Polshettiwar, V., Facile and sustainable synthesis of shaped iron oxide nanoparticles: effect of iron precursor salts on the shapes of iron oxides. *Scientific reports* **2015,** *5*(9733), 1-14.
5. Jangir, L. K.; Kumari, Y.; Kumar, A.; Kumar, M.; Awasthi, K., Investigation of luminescence and structural properties of ZnO nanoparticles, synthesized with different precursors. *Materials Chemistry Frontiers* **2017**, *1*, 1413-1421
6. Arellano, J. S.; Rosendo, E.; Romano, R.; Nieto, G.; Diaz, T.; García, G.; Juárez, H.; Pacio, M.; Galeazzi, R.; Morales, C., Synthesis and characterization of CdSe nanoparticles with cadmium precursor variation in colloidal synthesis. *Advanced Materials Research* **2014,** *976*, 52-58.
7. Duphil, D.; Bastide, S.; Lévy-Clément, C., Chemical synthesis of molybdenum disulfide nanoparticles in an organic solution. *Journal of Materials Chemistry* **2002,** *12* (8), 2430-2432.
8. Mittal, V., *Encapsulation nanotechnologies*. John Wiley & Sons: 2013.
9. Guo, W.; Chen, Y.; Wang, L.; Xu, J.; Zeng, D.; Peng, D.-L., Colloidal synthesis of $MoSe_2$ nanonetworks and nanoflowers with efficient electrocatalytic hydrogen-evolution activity. *Electrochimica Acta* **2017,** *231*, 69-76.
10. Sun, D.; Feng, S.; Terrones, M.; Schaak, R. E., Formation and interlayer decoupling of colloidal MoSe2 nanoflowers. *Chemistry of Materials* **2015,** *27* (8), 3167-3175.
11. Tonndorf, P.; Schmidt, R.; Böttger, P.; Zhang, X.; Börner, J.; Liebig, A.; Albrecht, M.; Kloc, C.; Gordan, O.; Zahn, D. R., Photoluminescence emission and Raman response of monolayer MoS_2, $MoSe_2$, and WSe_2. *Optics express* **2013,** *21* (4), 4908-4916.
12. Niu, L.; Li, K.; Zhen, H.; Chui, Y. S.; Zhang, W.; Yan, F.; Zheng, Z., Salt-Assisted High-Throughput Synthesis of Single-and Few-Layer Transition Metal

Dichalcogenides and Their Application in Organic Solar Cells. *Small* **2014,** *10* (22), 4651-4657.

13. Dong, N.; Li, Y.; Feng, Y.; Zhang, S.; Zhang, X.; Chang, C.; Fan, J.; Zhang, L.; Wang, J., Optical limiting and theoretical modelling of layered transition metal dichalcogenide nanosheets. *Scientific reports* **2015,** *5*(14646), 1-10.
14. Tongay, S.; Zhou, J.; Ataca, C.; Lo, K.; Matthews, T. S.; Li, J.; Grossman, J. C.; Wu, J., Thermally driven crossover from indirect toward direct bandgap in 2D semiconductors: $MoSe_2$ versus MoS_2. *Nano letters* **2012,** *12* (11), 5576-5580.
15. Savjani, N.; Lewis, E. A.; Bissett, M. A.; Brent, J. R.; Dryfe, R. A.; Haigh, S. J.; O'Brien, P., Synthesis of Lateral Size-Controlled Monolayer 1 H-MoS_2@ Oleylamine as Supercapacitor Electrodes. *Chemistry of Materials* **2016,** *28* (2), 657-664.
16. Guo, W.; Chen, Y.; Wang, L.; Xu, J.; Zeng, D.; Peng, D.-L., Colloidal synthesis of $MoSe_2$ nanonetworks and nanoflowers with efficient electrocatalytic hydrogen-evolution activity. *Electrochimica Acta* **2017,** *231*, 69-76.
17. Chen, D.; Liu, M.; Yin, L.; Li, T.; Yang, Z.; Li, X.; Fan, B.; Wang, H.; Zhang, R.; Li, Z., Single-crystalline MoO_3 nanoplates: topochemical synthesis and enhanced ethanol-sensing performance. *Journal of Materials Chemistry* **2011,** *21* (25), 9332-9342.
18. Yu, X.; Wang, J.; Zhang, M.; Yang, P.; Yang, L.; Cao, D.; Li, J., One-step synthesis of lamellar molybdate pillared hydrotalcite and its application for AZ31 Mg alloy protection. *Solid State Sciences* **2009,** *11* (2), 376-381.
19. Ghosh, S.; Srivastava, C.; Nath, S.; Celis, J.-P., Simple formation of nanostructured molybdenum disulfide thin films by electrodeposition. *International Journal of Electrochemistry* **2013,** *2013*(138419), 1-8.
20. Zhang, H. Synthesis of Highly Active Unsupported Molybdenum Sulfide Catalysts for Hydrosulfurization and Hydrodeoxygenation. University of New Brunswick, **2014**.
21. Cheng, M.; Fan, H.; Xu, Y.; Wang, R.; Zhang, X., Hollow Co_2P nanoflowers assembled from nanorods for ultralong cycle-life supercapacitors. *Nanoscale* **2017,** *9* (37), 14162-14171.

Chapter 5: The effect of a co-surfactant to oleylamine in the colloidal synthesis of $MoSe_2$ nanomaterials.

5.1 Introduction

The colloidal synthesis of nanoparticles is normally conducted in organic solvents that perform various functions. The solvents are normally long-chain hydrocarbons such as oleylamine (OAm), oleic acid (OA) and 1-octadacene (ODE). These solvents have head groups such as amines or carboxyl groups which are able to preferentially bind on the surface of the nanoparticles.[1-3]This allows the solvents to stabilize the nanoparticles and prevent them from agglomerating, to control the size and morphology of the nanoparticles and also to protect the surface of the nanoparticles from oxidation.[4-5]These solvents which are at times called capping agents or surfactants are also used in the synthesis of semiconductor nanomaterials in colloidal synthesis.[6]They are able to bind to the surface of the nanoparticles through chemisorption, electrostatic interaction and hydrophobic interaction. The choice of surfactant is one of the most important parameters one must consider in the colloidal synthesis of nanomaterials.[7-9] This is due to the ability of these surfactants to control the size and morphology of the nanoparticles.[10]The surfactants can control the morphology by the preferential binding of the surfactant on a certain facet of the nanocrystal during growth that causes the nanocrystal to grow in a particular way. This preferential growth can lead to control of the morphology of the nanoparticles. The use of different surfactants to control the morphology of layered nanomaterials has been explored extensively. Cara *et al.* has shown that in the synthesis of iron oxide nanoparticles the use of oleic acid results in the formation of hematite nanoplatelets while the use of oleylamine in the synthesis results in the formation of spherical magnetite nanoparticles.[11] Debroye *et al.* have shown that one can control the morphology of organolead iodide perovskite nanocrystal from nanorods to nanoplatelets by using oleylamine alone or a mixture of oleylamine and oleic acid respectively.[12] The transition metal dichalcogenides (TMDs) such as MoS_2 and $MoSe_2$ are naturally layered materials. In the colloidal synthesis of these materials they seem to conform to the Wulf construction and form either monolayer or few-layer nanosheets.[12-13]There are few attempts that have been made to synthesize these nanomaterials using oleylamine as a solvent/surfactant.[13-14] These attempts resulted

in the formation of few-layer nanosheets. Jung *et al.* have synthesized WSe_2 and $MoSe_2$ mono and few-layer nanosheets, they have studied the effects of using various surfactants on the structure of these materials.[15] Jung *et al.* have reported that the amine head group in oleylamine binds to the edge site of the nanosheets restricting growth along the lateral dimensions of the nanosheets Fig 5.1(a). They have shown that oleylamine can be used to control the lateral dimensions of these materials.

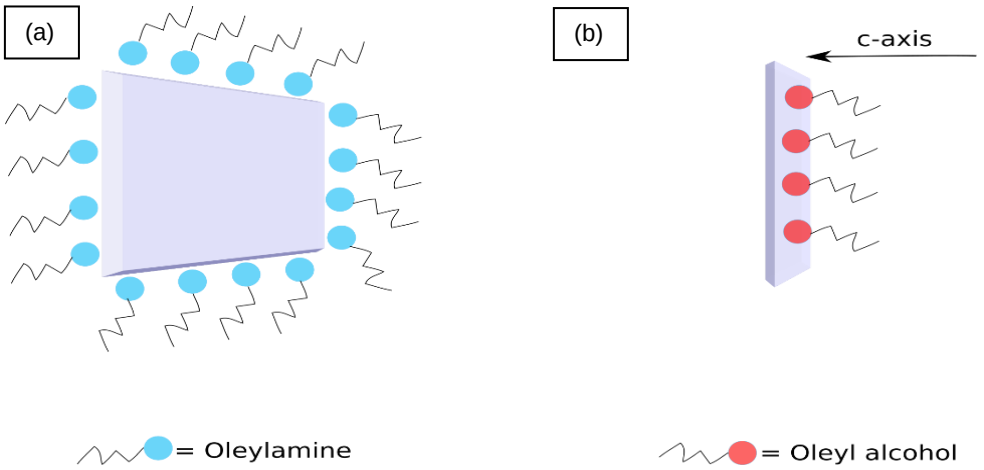

Figure 5.1: Binding of the head groups of the surfactants on the facets of the nanomaterials: (a) oleylamine binds on the edge facets and (b) oleyl alcohol binds on the basal plane.

The great challenge in the synthesis of these nanomaterials however is the control of the thickness of the nanosheets. The properties of these nanomaterials are dependent on the number of layers or the thickness of the nanosheets.[16] Controlling the vertical growth of the nanosheets along the c-axis and therefore the thickness can affect the properties of the material. Jung *et al.* have found that the use of oleyl alcohol can control the vertical growth of the nanosheets and therefore control the thickness of the nanosheets Fig. 5.1(b). The functional group on the oleyl alcohol (hydroxyl group) have been found to bind strongly to the basal plane of the nanomaterials therefore restricting vertical growth. The thickness of the nanosheets could therefore be controlled using the right surfactant. This work focuses on the synthesis of $MoSe_2$ nanomaterials using oleylamine in conjunction with a co-surfactant. The previous work on the synthesis of these materials (Chapter 4) using oleylamine as a surfactant have resulted in the formation nanoflowers compromised of small lateral dimension few-layer nanosheets.

In this study the use of oleic acid which contains a carboxyl head group (Fig. 5.2) was used as a co-surfactant in order to control the growth of the nanosheets along the c-axis thereby controlling the thickness of the nanosheets. Considering how the properties of these nanomaterials are dependent on the thickness of the nanosheets, the ability to control the thickness of the nanosheets using the right surfactant is crucial. This study will also determine whether it is possible to simultaneously control the lateral dimensions and the thickness of the nanosheets using oleylamine as the surfactant and oleic acid as the co-surfactant. Considering that this is a study of how the head groups of surfactants affects the growth of the $MoSe_2$. 1-octadacene(ODE) which is a common surfactant that does not contain an amine or carboxyl group. ODE was also used in this study to investigate whether a surfactant with no particular head group can influence the growth of the nanomaterials. The structures of the surfactants with their different head groups is shown in Fig. 5.2.

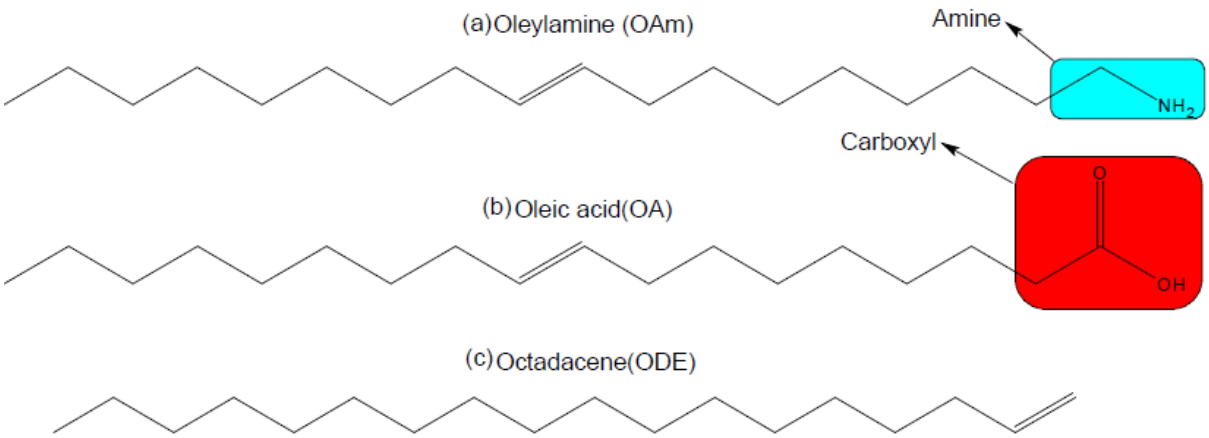

Fig 5.2: Structures of the surfactant used in synthesis of $MoSe_2$ nanomaterials (a) oleyamine(OAm), (b) oleic acid(OA) and octadecene(ODE).

In the mixture of oleylamine and oleic acid it is suspected that the amine group in oleylamine will bind on the edge sites of the nanosheets and the oleic acid will bind on the basal plane of the nanosheets through the carboxyl head group thus restricting growth along the c-axis. This should affect the thickness of the nanosheets compared to when oleylamine alone is used. The use of 1-octadacene on the other hand should not change the morphology and the thickness of the synthesized nanosheets because 1-octadacene is not expected to bind to the nanomaterials at all.

The ratio of surfactants used was taken from the work by Harris *et al.*[17] on the analysis of the interaction of oleylamine and oleic acid on the synthesis of Iron oxide nanoparticles using molecular dynamics. They found that the interaction between olaylamine and oleic acid plays an important role in the synthesis of the nanoparticles. They also found that the acid-base complex formation between the surfactants could affect some of the properties of the synthesized nanomaterials. One of the optimal OAm/OA ratios they determined to be effective in giving well defined monodisperse particles was 2:1.[17] This ratio was used in the synthesis of $MoSe_2$ using oleylamine and oleic acid. It was also used for the synthesis of $MoSe_2$ using oleyamine and 1-octadacene, with the ratio being 2:1 in OAm/ODE.

The capping of these surfactants on the surface of the nanoparticles can be studied using nuclear magnetic resonance(NMR). NMR is powerful technique normally used to determine the content and purity of organic samples, the technique has been used to determine the structure of unknown organic compounds.[18] The technique has been shown to be very useful in investigating the capping of such organic compounds as trioctylphosphine, oleic acid and 1-octadacene on the surface of various semiconductor nanocrystals. Hens *et al.* have used *In-situ* ^{1}H NMR to investigate the capping of trioctylphosphine oxide(TOPO) on InP quantum dots.[19]They have shown that the use of 1D ^{1}H NMR and diffusion ordered spectroscopy(DOSY) can be used to identify spectral features that arise from molecules adsorbed on the surface of nanoparticles.[19] In other words, it is possible to determine whether the organic molecules have indeed capped the nanoparticles using NMR spectroscopy. They have shown that it is also possible to quantify the average number of molecules per nanoparticle using ^{1}H-^{13}C HSQC spectroscopic data.[20] Fritzinger *et al.* have been able to identify molecules that interact with the nanoparticle surface using transfer NOE spectroscopy. This technique was used to extract information from NMR data in systems where free and bound ligands are in exchange equilibrium and the rate of exchange between the free and bound sates is fast. This was done using ZnO and CdTe quantum dots that were capped with octaylamine and dodecylamine respectively. Fritzinger *et al.* have also used NMR techniques to investigate the capping of oleic acid on CdSe quantum dots.[21] They have found in this work that the oleic acid capped nanoparticles were not in a system where the free and bound ligands were in an exchange equilibrium. However, the addition of excess free ligand forces

this exchange process to occur because the exchange process involves proton transfer from a free oleic acid molecule to a bound oleate. This study will demonstrate how NMR can be used to study the adsorption of these various surfactants on the $MoSe_2$ nanomaterials. NMR techniques will be used to determine whether the oleylamine has indeed capped the nanomaterials in $MoSe_2$ nanomaterials. The techniques will also be used to determine which of the surfactants actually bind on the surface of the nanoparticles, the oleylamine or the co-surfactants. This will give an idea on how the binding of the different surfactants on the surface of the nanomaterials affects their properties.

5.2 Materials and methods

5.2.1 Chemicals

Molybdic acid ((H_2MoO_4), 85%, Sigma-Aldrich), selenourea (CH_4N_2Se, 98%, Sigma-Aldrich), 1-octadacene (ODE, 90%, Sigma-Aldrich), oleylamine (OAm, 70%, Sigma-Aldich) and oleic acid (OA, 90%, Sigma-Aldrich) were used as received without purification.

5.2.2 Synthesis of $MoSe_2$ nanomaterials with oleylamine ($MoSe_2$-OAm)

A three-neck round bottom flask was filled with 20 ml of olelylamine, the mixture was degassed for 20 minutes under nitrogen. The temperature was increased to 50 ^oC and ~0.4 g (~ 3.0 mmmol) of selenourea was added to the reaction mixture and stirred for 10 minutes. Molybdic acid (~ 0.2 g (~ 1.5 mmol)) was added once the reaction temperature reached 220 ^oC, the temperature was then increased until the desired temperature of 300 ^oC was reached. The reaction was allowed to continue for 90 mins, after which the product was collected and washed with toluene and ethanol by centrifugation.

5.2.3 Synthesis of $MoSe_2$ nanomaterials with oleylamine and 1-octadace ($MoSe_2$-OAm/ODE)

A three-neck round bottom flask was filled with 10 ml of oleylamine and 5 ml of ODE, the mixture was degassed for 20 minutes under nitrogen. The temperature was increased to 50 ^oC and ~ 0.4 g (~3.0 mmol) of selenourea was added to the reaction mixture and stirred for 10 minutes. Molybdic acid (~ 0.2 g (0.15 mmol)) was added

once the reaction temperature reached 220 ^{o}C, the temperature was then increased until the desired temperature of 300 ^{o}C was reached. The reaction was allowed to continue for 90 mins, after which the product was collected and washed with toluene and ethanol by centrifugation.

5.2.4 Synthesis of $MoSe_2$ nanomaterials with oleyamine and oleic acid ($MoSe_2$-OAm/OA)

A three-neck round bottom flask was filled with 10 ml of oleylamine and 5 ml of OA, the mixture was degassed for 20 minutes under nitrogen. The temperature was increased to 50 ^{o}C and ~ 0.4 g (3.0 mmol) of selenourea was added to the reaction mixture and stirred for 10 minutes. Molybdic acid (~ 0.2 g (0.15 mmol)) was added once the reaction temperature reached 220 ^{o}C, the temperature was then increased until the desired temperature of 300 ^{o}C was reached. The reaction was run for 90 mins, after which the product was collected and washed with toluene and ethanol by centrifugation.

5.2.5 Characterisation techniques

The structural properties were investigated using powder X-ray diffraction(PXRD) and Raman spectroscopy. The phase purity, crystallinity and preferred crystal orientation of the products were examined by using XRD on a Bruker MeasSrv (D2-205530)/D2-205530 diffractometer using secondary graphite monochromated CoKα radiation (λ 1.78897 Å) at 30 kV/30 mA. Measurements were taken using a glancing angle of incidence detector at an angle of 2°, for 2θ values over 10 - 90° in steps of 0.026° with a step time of 37 s and at a temperature of 25 °C. Raman spectroscopy (J-Y T64000 micro-Raman spectrometer, Horiba Jobin-Yvon, Ltd., Stanmore, UK) equipped with a liquid nitrogen cooled charge coupled device detector. All samples were measured after excitation with a laser wavelength of 514.5 nm. The NMR data was obtained using a 500 MHz Bruker avance III, the samples were collected using $CDCl_3$ as a solvent at 300K. The optical properties were determined using a Varian Cary Eclipse (Cary 50) UV-vis absorption spectrophotometer. The sample sizes and morphologies were determined by the transmission electron microscopy (TEM) carried out on a FEI Technai T12 TEM microscopy operated at an acceleration voltage of 200 kV with a beam spot size of 20 - 100 nm in TEM mode.

5.3 Results and discussion

The composition, phase and crystallinity of the materials were determined using powder X-ray diffraction. The powder diffraction patterns of $MoSe_2$-OAm, $MoSe_2$-OAm/ODE and $MoSe_2$-OAm/OA shown in Fig. 5.3 confirm the formation of $MoSe_2$ in the 2H hexagonal phase (JCPDS card no: 03-065-3999). The broad nature of the diffraction peaks is characteristic of nanostructured materials.

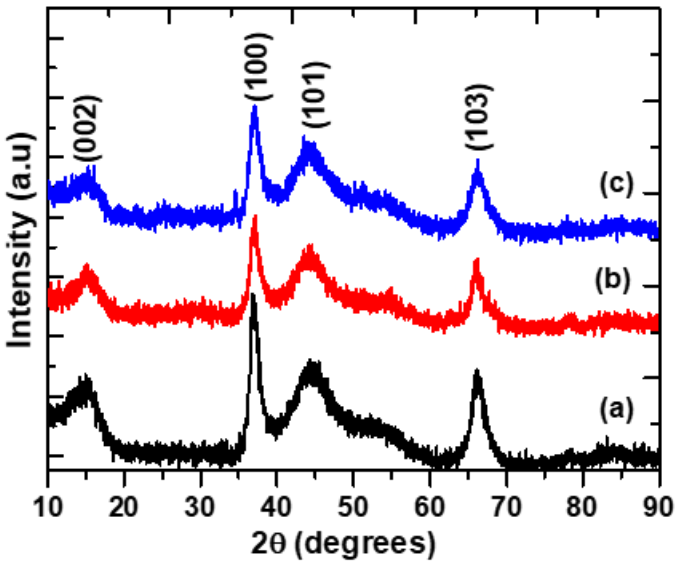

Figure 5.3: Powder X-ray diffraction patterns of the synthesized products $MoSe_2$-OAm, $MoSe_2$-OAm/ODE and $MoSe_2$-OAm/OA.

The (002) peak observed at ~ 14 ^{o} is due to the diffraction along the c-axis of the nanocrystal caused by stacking of the layers in the nanosheets, the appearance of this diffraction peak indicates that multilayer nanosheets have been formed.[22] The thickness of the nanosheets can be approximated using the Debye-Sherrer equation. This can be done using the FWHM (full width at half maximum) of the (002) peaks which represents the interplanar spacing between the layers in the c-axis. The Debye-Sherrer equation can thus be used to approximate the crystallite size of the nanosheets along the c-axis which would be the thickness of the nanosheets.[22] The thickness of the $MoSe_2$-OAm nanosheets was determined using the Debye-Scherrer equation to be 3.82 nm, the thickness of the $MoSe_2$-OAm/ODE was found to be 3.63 nm and the thickness of the $MoSe_2$-OAm/OA nanosheets was 2.65 nm. The single layer thickness of the $MoSe_2$ nanosheets is ~0.70 nm. The number of layers in the

$MoSe_2$-OAm were found to be ~ 5-6 layers, along with the $MoSe_2$-OAm/ODE nanosheets.[22] The number of layers in the $MoSe_2$-OAm/OA nanosheets was determined to be ~ 4 layers. The addition of oleic acid as the co-surfactant does have a slight influence on thickness of the $MoSe_2$ nanosheets. This slight difference is also mirrored in the UV-Vis absorption spectra of the material.

The Raman spectrum of $MoSe_2$ is known to have two characteristic peaks, the out of plane A_{1g} and the in plane E^1_{2g}. The position of the A_{1g} and the E^1_{2g} are 242 cm^{-1} and 286 cm^{-1} for the bulk sample.[23] The A_{1g} is known to red-shift from its bulk position for monolayer or few-layer $MoSe_2$ nanomaterials. The E^1_{2g} has been known to blue shift from the bulk for mono or few-layer $MoSe_2$ nanomaterials. The degree at which the peaks shift from their bulk positions can be used to estimate the number of layers on the nanosheets. The Raman spectra of $MoSe_2$-OAm, $MoSe_2$-OAm/ODE and $MoSe_2$-OAm/OA are shown in Fig. 5.4.

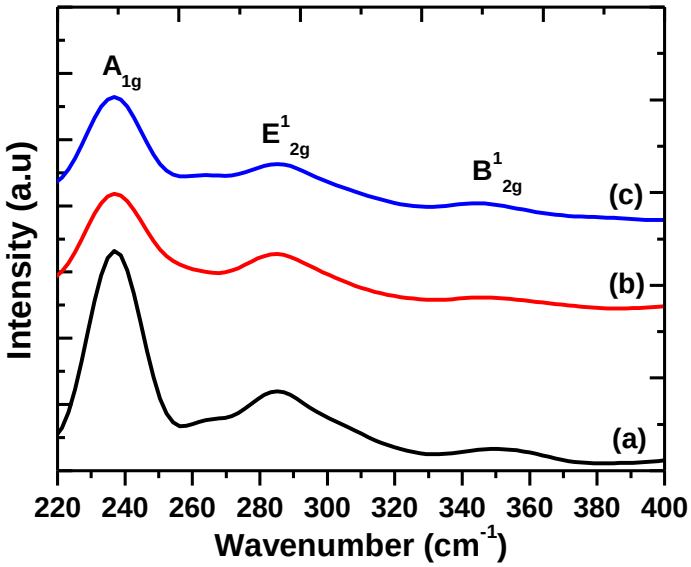

Figure 5.4: The Raman spectra of $MoSe_2$-OAm, $MoSe_2$-OAm/ODE and $MoSe_2$-OAm/OA, the characteristic peaks A_{1g}, E^1_{2g} and B^1_{2g} are shown in the spectra.

The characteristic A_{1g} and E^1_{2g} peaks are observed in the spectra of the $MoSe_2$-OAm, $MoSe_2$-OAm/ODE and $MoSe_2$-OAm/OA samples. The A_{1g} is at 237 cm^{-1} which has red-shifted from the bulk, the new position of the A_{1g} is associated with few-layer nanosheets.[24] The E^1_{2g} peak is situated at 285.7 cm^{-1},the position of the E^1_{2g} in the

Raman spectra indicates that bi-layer nanosheets have been formed.[22] The appearance of the B^1_{2g} at 350 cm^{-1} which does not appear for monolayer or bulk layer nanosheets indicates that the nanosheets are few layered with a layer number between 2 – 5 layers This result is consistent with the information obtained from the PXRD analysis. The appearance of the (002) diffraction peak as previously mentioned confirms the formation of multilayer nanosheets, this along with the analysis of the Raman spectra confirms the formation of few layer nanosheets. This suggests that the nanosheets formed are certainly not bulk but are not monolayer nanosheets either which is consistent with the results from the Debye-Sherrer calculations which suggest that the nanosheets are between 4 – 6 layers thick. However, comparison of the shifts in the characteristic peaks of the $MoSe_2$-OAm and the shifts of the characteristic peaks of the $MoSe_2$-OAm/ODE and $MoSe_2$-OAm-OA shows no significant differences in the peak shifts. This is surprising as one would expect the shifts in the Raman peaks of the $MoSe_2$-OAm/OA to be larger due to the difference in the number of layer in the nanosheets of this sample and the others. In this case the Raman analysis can help determine whether the nanomaterials synthesized using colloidal synthesis resemble their bulk counterpart but cannot accurately determine number of layers in the few-layer nanosheets.

The UV-Vis absorption spectra of $MoSe_2$ has been shown to have two characteristic exciton absorption peaks around 800 and 700 nm which are referred to as A and B respectively.[25] The UV-Vis Absorption spectra of the $MoSe_2$-OAm, $MoSe_2$-OAm/ODE and $MoSe_2$-OAm/OA are shown in Fig. 5.5.

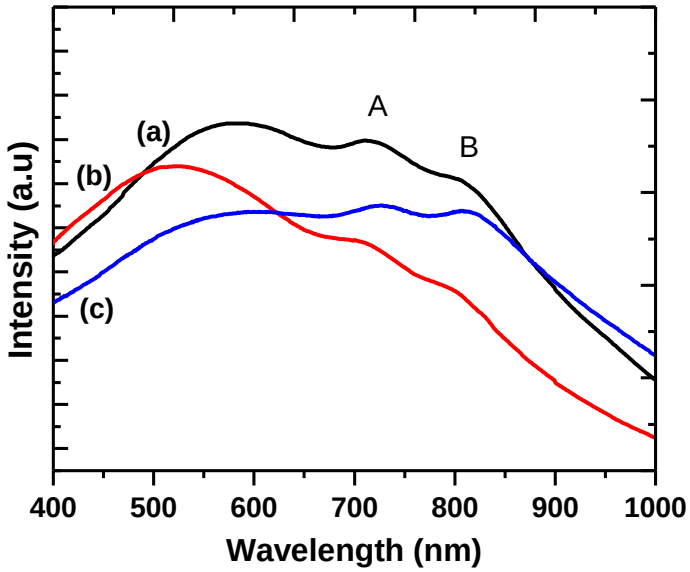

Figure 5.5: UV-vis absorption spectra of the (a) $MoSe_2$-OAm, (b) $MoSe_2$-OAm/ODE and (c) $MoSe_2$-OAm/OA. The excitonic absorption peaks A and B are denoted in the spectra.

The peak at around 400 nm is associated with optical transitions between the density of states peaks in the valence and conduction bands.[26] The exciton absorption peaks A and B for $MoSe_2$-OAm are observed at 720.9 nm and 817.7 nm respectively. The exciton absorption peaks A and B of the absorption spectrum of the $MoSe_2$-OAm/ODE nanomaterials are situated at 708.5 and 800.9 nm respectively and for the $MoSe_2$-OAm/OA nanomaterials the exciton absorption peaks were found to be at 718.6 and 813.8 nm for A and B respectively. The band-gap of the $MoSe_2$ nanomaterials has blue shifted from the bulk. The bulk band-gap is reported in literature as 1.09 eV.[27] The band-gap for $MoSe_2$-OAm and $MoSe_2$-OAm/ODE has blue-shifted to 1.52 eV. The band-gap for $MoSe_2$-OAm/OA has blue-shifted to 1.55 eV. The blue-shift is due to quantum confinement effects that arise when the number of layers on the $MoSe_2$ transition from the bulk to mono or few-layer nanosheets.[28] This confirms that the nanosheets are few-layer as already confirmed by PXRD and Raman spectroscopy analysis. The quantum confinement effect is more pronounced in the $MoSe_2$-OAm/OA as the band-gap is slightly more blue-shifted from the bulk compared to $MoSe_2$-OAm and $MoSe_2$-OAm/ODE. This is due to the smaller number of layers in the $MoSe_2$-OAm/OA compared to the other two samples.

While oleylamine can only bind to the surface of the nanomaterials using the amine head group oleic acid has three binding modes by which to attach itself to the surface of the nanoparticles. Oleic acid can bind in a monodentate, bridged or chelating fashion on the surface of the nanoparticles. Statistically not considering electron affinity but only the binding modes oleic acid is much more likely to bind to Mo^{4+} on the nanoparticle surface.[17] The FTIR spectra of pure oleylamine, pure oleic acid and $MoSe_2$-OAm/OA are shown in Fig. 5.6. Pure oleylamine and oleic acid have the symmetric and asymmetric CH_2 stretches at 2841 and 2931 cm^{-1} respectively.[29]For pure oleic acid the strong peak observed at 1708 cm^{-1} corresponds to the characteristic C=O stretching vibrational mode.[29]

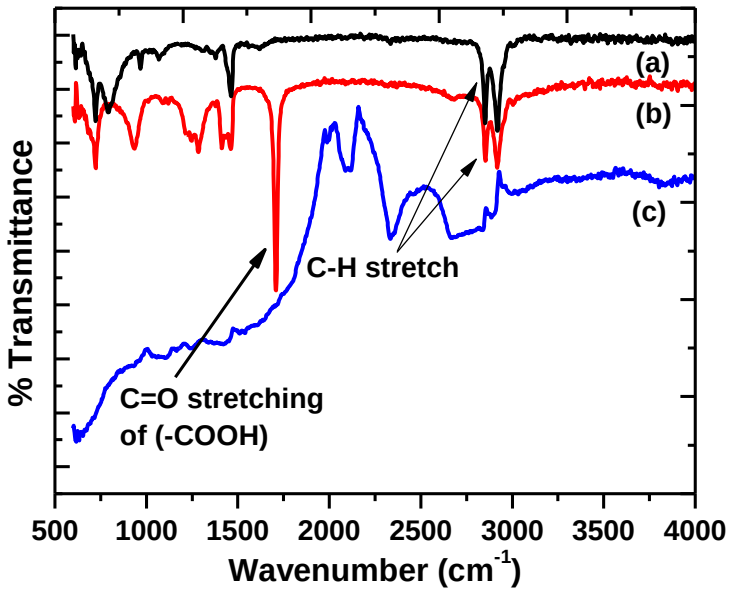

Figure 5.6: FTIR spectra of the pure oleylamine (a), pure oleic acid (b) and the $MoSe_2$-OAm/OA nanomaterials (c).

The 1708 cm^{-1} peak which corresponds to the C=O in oleic acid has disappeared in the FTIR spectrum of $MoSe_2$-OAm/OA indicating that oleic acid has adsorbed on the surface of the nanomaterials as a carboxylate.[17,19] Unfortunately, there is no way to prove definitively whether the oleylamine has also adsorbed on the surface of the nanomaterials using FTIR. It has been shown that there are no spectral features in the FTIR of nanoparticles that shows whether oleylamine has adsorbed on the surface of the nanoparticles.[30] This has been shown even in synthesis of nanoparticles where

oleylamine alone has been used. The 1-octadacene on the hand was not expected to adsorb on the surface of the nanoparticles as the surfactant has no head group that can bind on the surface of the $MoSe_2$ nanomaterials.

The use of FTIR spectrometry was insufficient to determine whether the $MoSe_2$ nanoparticles were indeed capped with oleylamine molecules nor was it sufficient conclude that oleic acid had capped on the $MoSe_2$-OAm/OA nanoparticles instead of oleylamine. Nuclear magnetic resonance(NMR) was used to determine whether oleylamine had indeed capped on the $MoSe_2$-OAm nanoparticles. It was also used to determine whether oleylamine or the co-surfactants had capped on the $MoSe_2$-OAm/ODE and $MoSe_2$-OAm/OA.

1D ^{1}H NMR was used to obtain the ^{1}H NMR spectrum of free oleylamine which means oleylamine that is not bound to the nanoparticles. The ^{1}H NMR spectrum of oleylamine is shown in Fig A5.1 with the assigned resonance peaks for the respective protons. This spectrum will then be compared to that of the capped nanoparticles. There are certain differences in the spectrum of the capped nanoparticles to that of the free surfactant that are used to determine whether the surfactant has capped on the nanoparticles.[21]Firstly the ^{1}H NMR spectra for the capped nanoparticles should contain the main resonance peaks of the surfactant to show that the surfactant is indeed present in the nanoparticle dispersion.[21] Secondly a broadening and slight shifting of the resonance peaks is normally observed for the ^{1}H spectrum of the nanoparticle dispersion compared to the resonance peaks of the free surfactant to show that the surfactant has indeed adsorbed on the surface of the nanoparticles.[19,21] The ^{1}H NMR spectrum of free oleylamine is shown in Fig. 5.7(a), the ^{1}H NMR spectra of the $MoSe_2$-OAm particles are shown in Fig. 5.7(b).

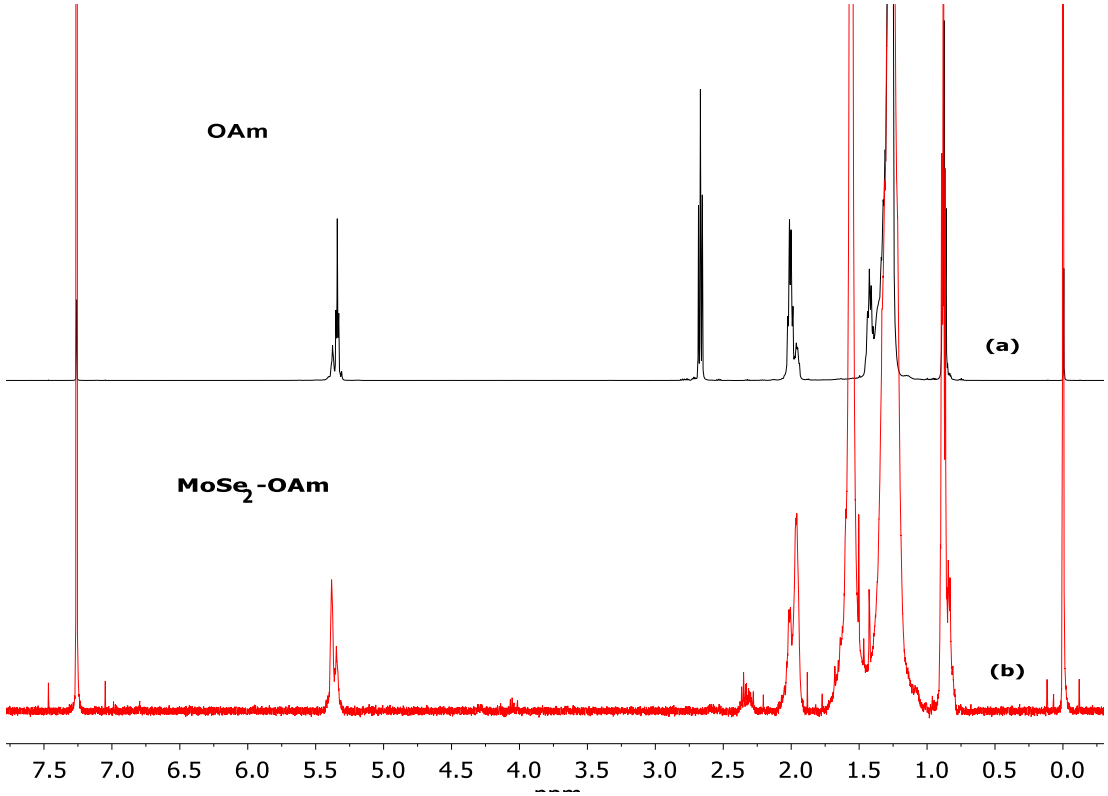

Figure 5.7: The ^{1}H NMR spectra of (a) the free oleylamine(OAm) and (b) $MoSe_2$-OAm.

The ^{1}H NMR spectrum of $MoSe_2$-OAm contains the same features as those found in free oleylamine. This confirms that oleylamine is present in the nanoparticle dispersion. However, the resonance peaks for the $MoSe_2$-OAm that also appear in free oleylamine appear to be much broader and slightly shifted compared to the resonance peaks found in free oleylamine. The broadening and slight shift of the resonance peaks is expected for OAm that is bound to the nanoparticles.[31] The effect can also be observed in the shift and broadening of the signal from the protons adjacent to the amine group (-C**H**$_2$-NH$_2$). The signal seems to shift from between 2.75 – 3.0 ppm to 2.25 ppm – 2.5 ppm. The peak also seems to drop in intensity and broadens. This effect can be clearly seen in the alkene proton resonance peaks between 5.30 and 5.42 ppm as shown in Fig. 5.8.

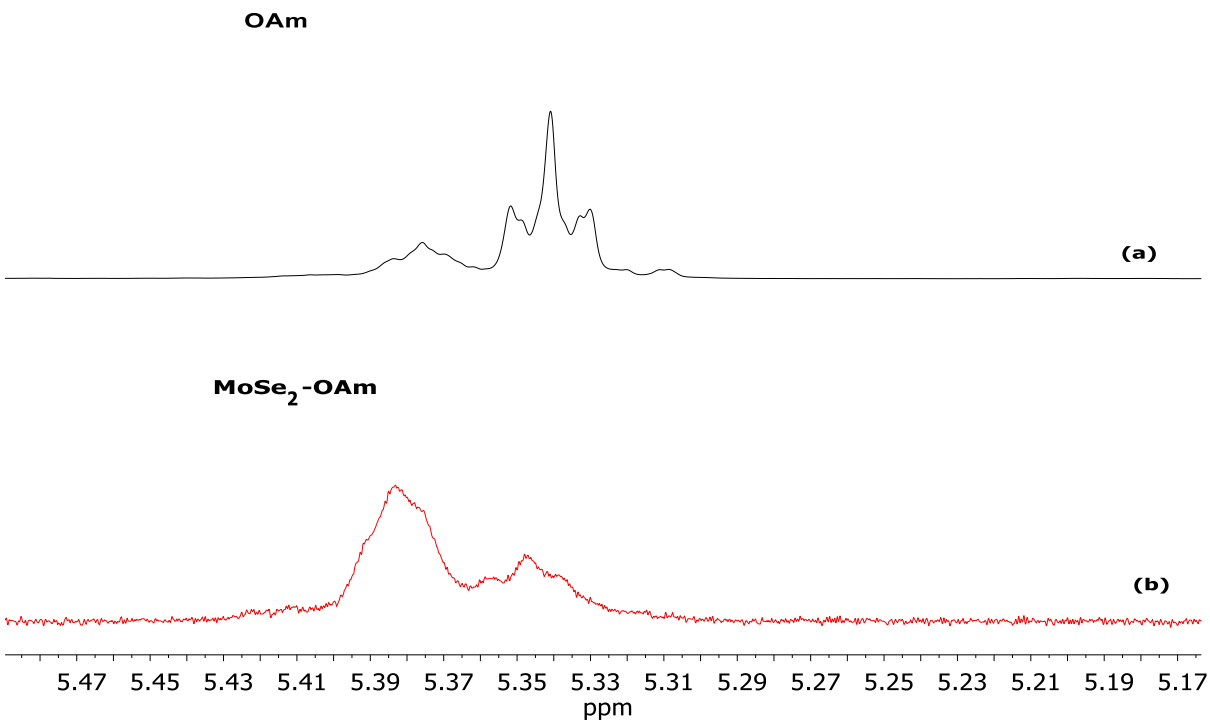

Figure 5.8: ^{1}H NMR spectra showing the resonance peaks of the alkene protons for (a) free oleylamine (b) olylamine bound to nanoparticles in $MoSe_2$-OAm.

The resonance of the peak at ~ 5.34 ppm has slightly shifted in the $MoSe_2$-OAm from the free oleylamine and the peak has broadened significantly compared to the sharp peak from the free oleylamine. The peak at ~ 5.39 ppm has also significantly broadened and slightly shifted compared to the peak in free oleylamine.

^{1}D DOSY (Diffusion ordered NMR spectroscopy) technique allows one to measure the diffusion coefficient of these molecules in a chosen solvent. The diffusion coefficient of the capped nanoparticles can be compared to that of the free oleylamine. The diffusion coefficient of the capped nanoparticles is expected to be lower than that of the free oleylamine because the diffusion coefficient is inversely proportional to the weight/size of the molecule.[32] The capped nanoparticles have a higher mass than the free oleylamine, so they are expected to have a lower diffusion coefficient.[19-21] The DOSY spectrum of the free oleylamine is shown in Fig. A5.4. The bottom axis shows the chemical shifts of the olleylamine resonance peaks and the right axis shows the diffusion constant for the resonance peaks. The DOSY spectrum clearly shows the

resonance peaks of oleylamine giving rise to the same diffusion coefficient. The diffusion coefficient for free oleylamine was determined to be 15.6 x 10^{-10} m^2/s. The DOSY spectrum of $MoSe_2$-OAm is shown in Fig. A5.6. The DOSY of the $MoSe_2$-OAm also clearly shows the resonance peaks giving rise to the same diffusion coefficient. The diffusion coefficient was determined to be 11.9 x 10^{-10} m^2/s. As expected the diffusion coefficient of the $MoSe_2$-OAm is slower than that of free olelylamine which further confirms that the oleylamine has indeed capped onto the nanoparticles.[21]

The main objective of using NMR to characterize $MoSe_2$-OAm/ODE is to determine whether it is oleylamine that is capping the nanoparticles or 1-octadacene. Oleylamine should adsorb on the nanoparticles through the amine head group and 1-octadacene is not expected to adsorb the nanoparticles at all. The ^1H NMR spectrum of free 1-octadacene with the assigned resonance peaks is shown I Fig. A5.2. The ^1H NMR spectrum of free oleylamine, free 1-octadecene and $MoSe_2$-OAm/ODE is shown in Fig. 5.9.

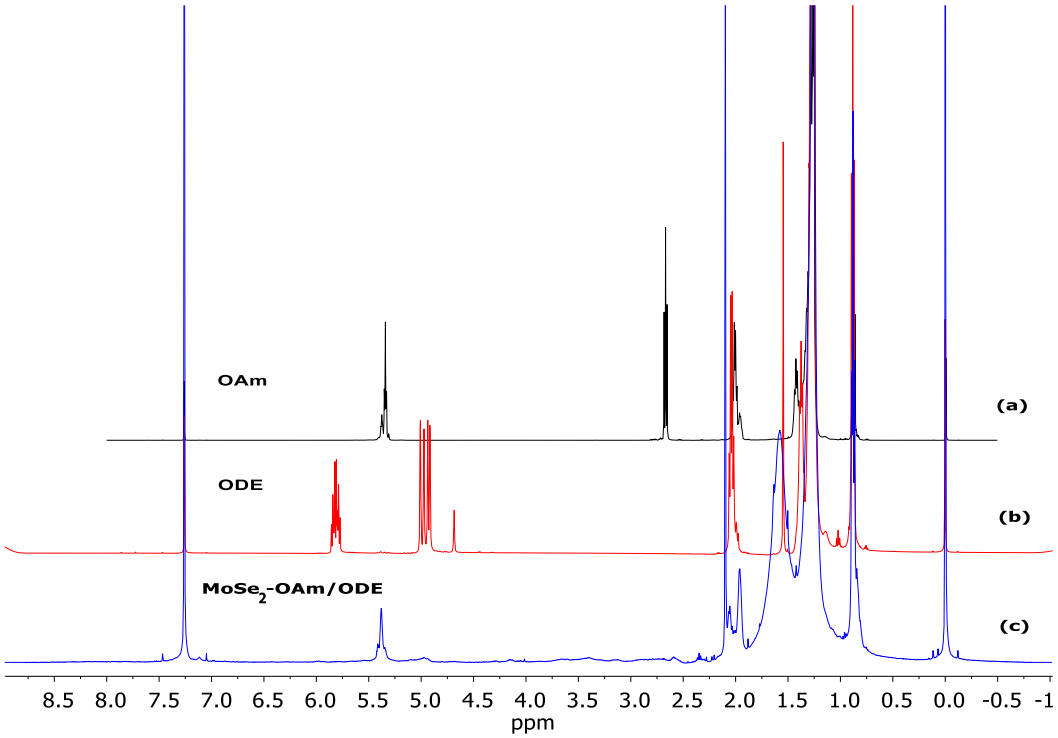

Figure 5.9: ^1H NMR spectra of (a) free oleyamine(black), (b) free 1-octadacene(red) and (c) $MoSe_2$-OAm/ODE nanomaterials in $CDCl_3$.

The ^1H NMR spectra shows that the spectrum of the $MoSe_2$-OAm/ODE does not show the characteristic resonance peaks observed in the spectrum of pure oleylamine

1-octadacene. However, the spectrum does contain the resonance peaks found in the spectrum of free oleylamine. In fact, the ^{1}H NMR spectrum of $MoSe_2$-OAm/ODE is identical to that of free oleylamine except that the resonance peaks of the $MoSe_2$-OAm/ODE nanoparticles have broadened and slightly shifted compared to the peaks in the spectrum of free oleylamine.[33] Again, this can clearly be shown in the resonance peaks of the alkene protons found between 5.30 ppm and 5.42 ppm. The resonance peaks are observed in the spectrum of free oleylamine and $MoSe_2$-OAm/ODE but not in the free 1-octadacene spectrum as shown in Fig. 5.9(b). The resonance peaks in the spectrum of $MoSe_2$-OAm/ODE have as expected for bound oleylamine broadened in slightly shifted compared to the peaks in the spectrum of free oleylamine as shown in Fig. 5.10(a) and (c).[31] This shows not only that oleylamine has indeed capped on the nanoparticles but that as expected 1-octadacene has not capped on the nanoparticles.

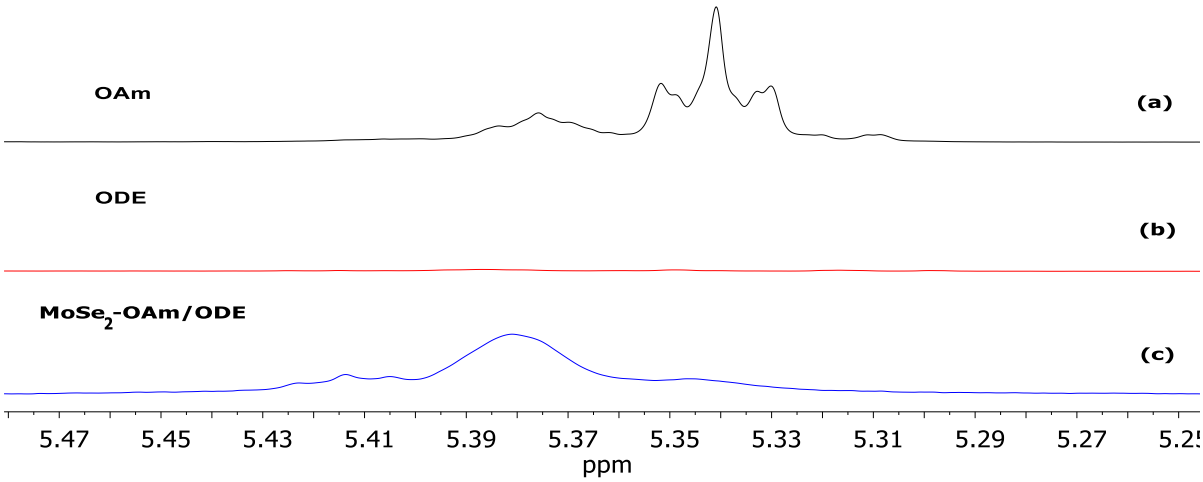

Figure 5.10: ^{1}H NMR resonance peaks of the alkene protons in (a) oleylamine and (b) 1-octadacene and (c) $MoSe_2$-OAm/ODE.

The DOSY spectrum of the $MoSe_2$-OAm/ODE as shown in Fig. A5.7 again shows that the resonance peaks all give rise to the same diffusion coefficient, the diffusion coefficient was found to be 9.0 x 10^{-10} m^2/s. The diffusion coefficient of ODE was determined to be 17.0 x 10^{-10} m^2/s from the DOSY spectrum of 1-octadacene shown in Fig. A5.5. The diffusion coefficient of $MoSe_2$-OAm/ODE is lower than that of free oleylamie and ODE which confirms that the nanoparticles are capped. The ^{1}H NMR analysis confirms that the nanoparticles as capped with oleylamine.

The NMR characterisation of $MoSe_2$-OAm/OA was a lot more complicated than that of $MoSe_2$-OAm/ODE because oleic acid has a carboxyl head group that can bind to the surface of the nanoparticles. Oleic acid has more binding modes than oleylamine; oleic acid can bind in a monodentate, bridged or chelating form. The FTIR spectrum of the $MoSe_2$-OAm/OA nanomaterials shows that oleic acid has bound to the nanoparticles. NMR techniques can help to confirm that the nanoparticles have indeed been capped by surfactant and to determine whether oleic acid has capped the nanoparticles instead of oleylamine. This will prove to be difficult for the ^{1}H NMR because the two molecules have a rather similar structure. The ^{1}H NMR spectrum of free oleic acid is shown in Fig. A5.3.

The ^{1}H NMR spectra of free oleylamine, free oleic acid and the $MoSe_2$-OAm/OA nanoparticles is shown in Fig 5.11.

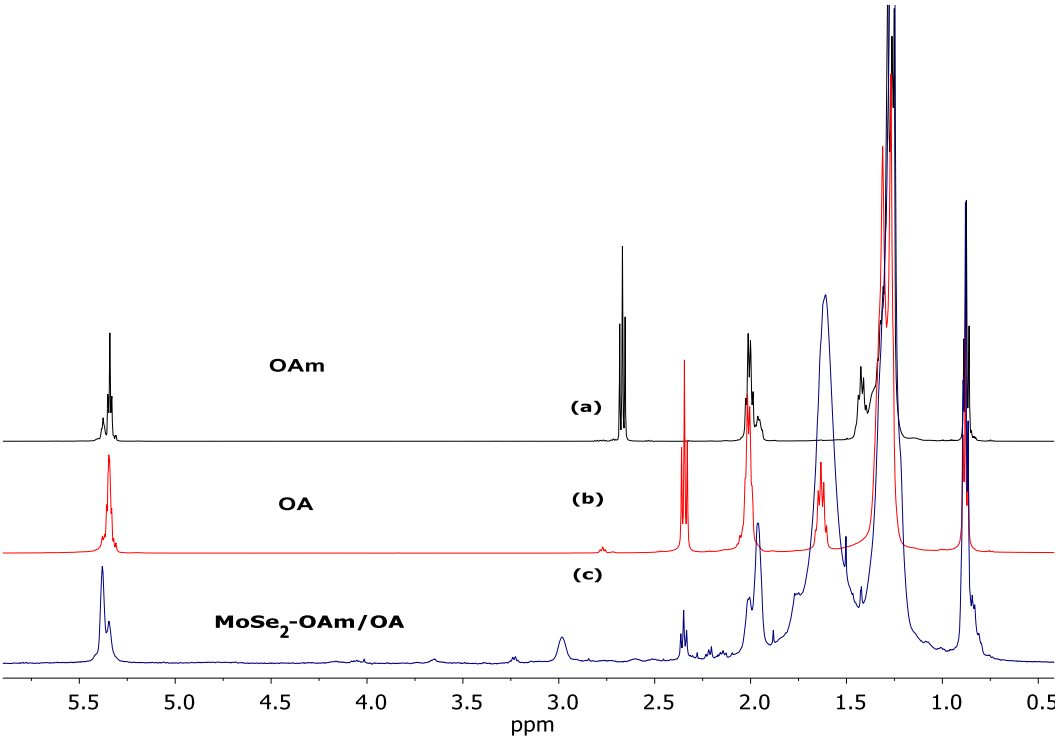

Figure 5.11: ^{1}H NMR spectra of (a) pure oleylamine(black), (b) pure oleic acid(red) and (c) $MoSe_2$-OAm/OA(blue).

The ^{1}H NMR spectra of $MoSe_2$-OAm/OA has the resonance peaks observed in both free oleylamine and oleic acid. As observed in the peaks between 0.5 and 2.0 ppm the peaks for $MoSe_2$-OAm/OA have broadened and slightly shifted from the free surfactants.[21] The spectrum also contains a peak at 3.0 ppm that does not appear in

the spectrum for free oleylamine and oleic acid. This can be clearly seen in the characteristic alkene protons resonance peaks between 5.30 and 5.42 ppm as shown in Fig. 5.12.

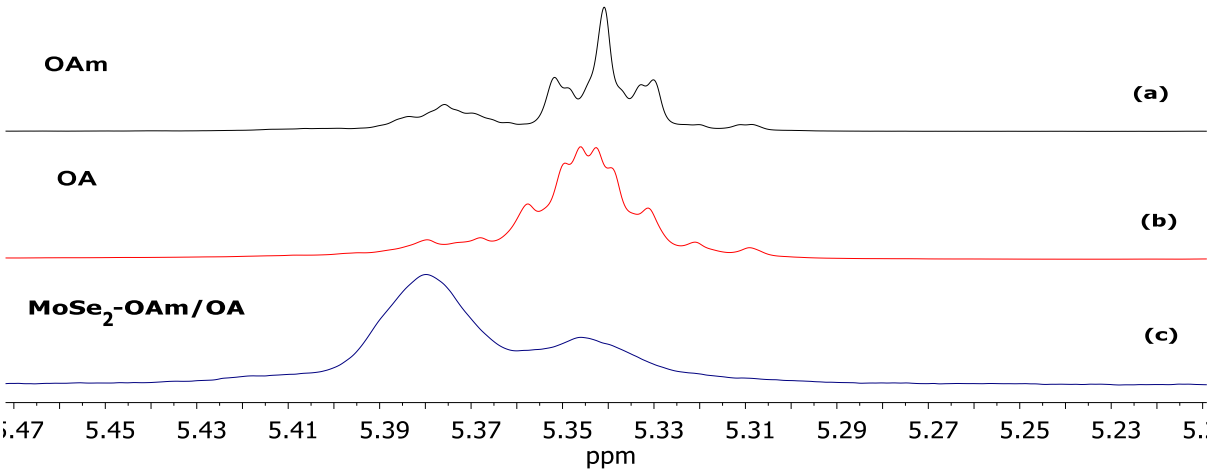

Figure 5.12: The resonance peaks for the alkene protons in (a) oleylamine, (b) oleic acid and (c) $MoSe_2$-OAm/OA nanoparticles in $CDCl_3$.

The alkene proton peaks in $MoSe_2$-OAm/OA have clearly broadened and shifted compared to the free surfactants. This proves that the nanoparticles have been capped by at least one of the surfactants. The challenge is the difficulty in determining whether oleylamine, oleic acid or both of these surfactants have capped on the nanoparticles. Fortunately, there is a marker found in oleic acid that is not found in oleylamine. In the ^1H NMR spectra of free oleic acid there is a resonance peak between 2.20 and 2.30 ppm that corresponds to the protons adjacent to the carboxyl group (-C**H**$_2$-C=O) Fig 13(b).[33]

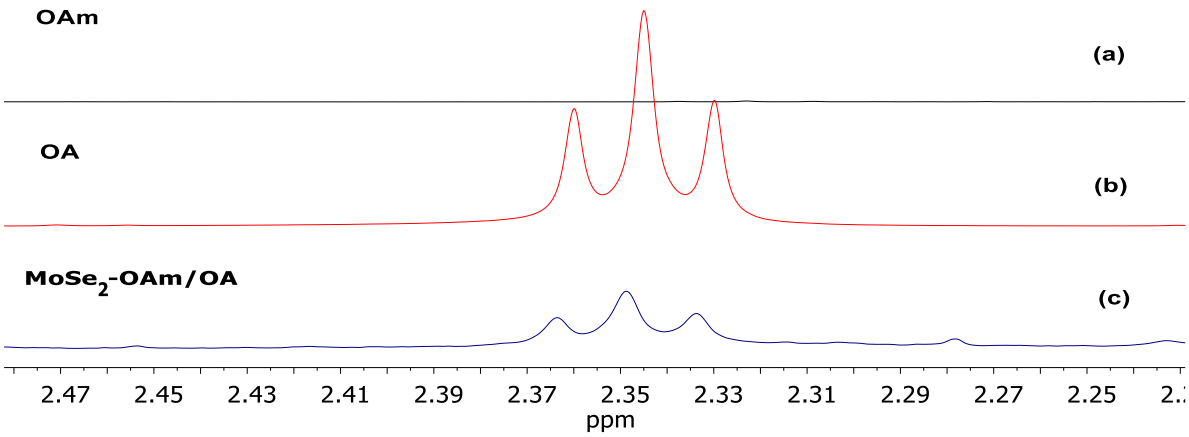

Figure 5.13: ^{1}H NMR spectrum of pure oleylamine, pure oleic acid and $MoSe_2$-OAm/OA showing the (-CH_2-C=O) resonance peak at 2.33-2.37 ppm for pure oleic acid and $MoSe_2$-OAm/OA.

This is a feature that does not exist in oleylamine as seen in Fig. 5.13(a) but this feature can be observed in the ^{1}H NMR spectrum of the $MoSe_2$-OAm/OA as shown in Fig. 5.13(c). This confirms the result found in the FTIR analysis that oleic acid does indeed bind on the nanoparticles. At this point it is not possible to say with certainty that oleylamine binds on the surface of the nanoparticles simultaneously with oleic acid.

The TEM images of the $MoSe_2$-OAm, $MoSe_2$-OAm/ODE and $MoSe_2$-OAm/OA are shown in Fig. 5.14. The use of oleylamine alone in the synthesis of $MoSe_2$-OAm results in the formation of nanoflowers as previously reported in chapter 4 and shown in Fig. 5.14(a,b). The nanoflowers form due to the formation of a central core during the initial stages of the reaction, the nanosheets grow from this core to form a morphology resembling a blooming flower.

(i) $MoSe_2$-OAm

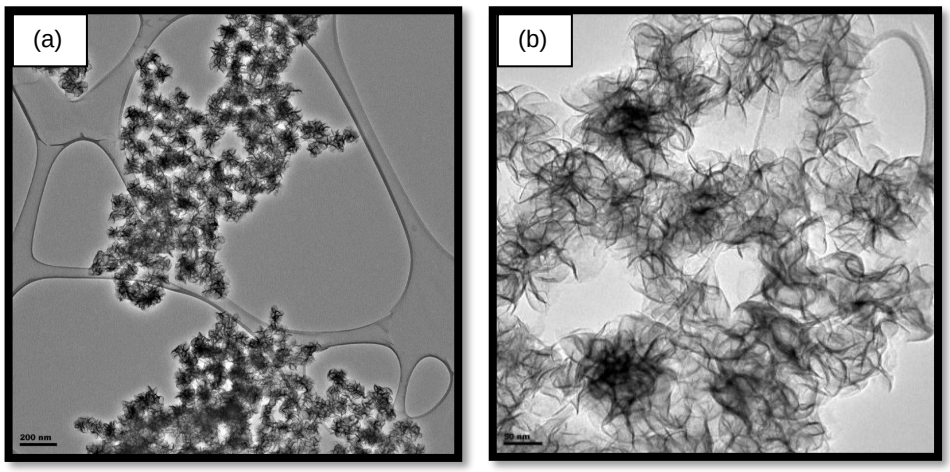

(ii) $MoSe_2$-OAm/ODE

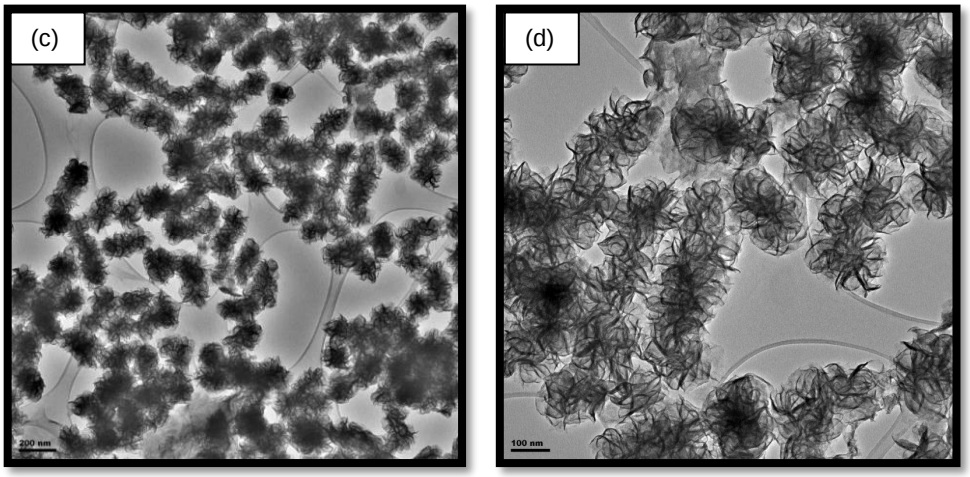

(iii) $MoSe_2$-OAm/OA

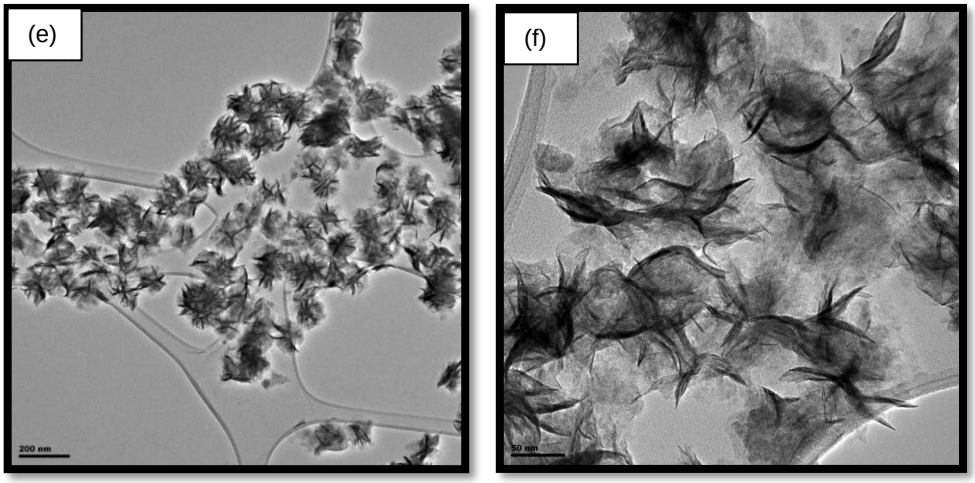

Figure 5.14: TEM images showing: (i) the nanoflowers formed in $MoSe_2$-OAm, (ii) the nanoflowers formed in $MoSe_2$-OAm/ODE and (iii) cluster of wrinkled overlapping nanosheets in $MoSe_2$-OAm/OA.

The nature of the nanoflowers of the synthesized using oleylamine alone do not seem to be significantly influenced by the introduction of 1-octadecene. The $MoSe_2$-OAm/ODE nanomaterials also show a nanoflower morphology as shown in Fig. 5.14(c). The only observable difference from the nanoflowers in $MoSe_2$-OAm and the nanoflowers in $MoSe_2$-OAm/ODE is seen in Fig. 5.14(d); the number of nanosheets that overlap to form the nanoflower in $MoSe_2$-OAm/ODE is larger leading to a darker central core. This can be easily explained using the analogy of a flower in bloom, the nanoflowers in $MoSe_2$-OAm/ODE can be viewed as having more petals than those in $MoSe_2$-OAm. The individual nanoflowers seem to agglomerate with other nanoflowers to form a network of the flower like nanostructures as shown in Fig. 5.14(d). At first glance the $MoSe_2$-OAm/OA nanostructures also seem to have a nanoflower morphology as shown in Fig. 5.14(e). A closer look shows that the $MoSe_2$-OAm/OA nanostructures are an aggregate of small lateral dimension wrinkled few-layer nanosheets as shown in Fig. 5.14(f). The nanosheets seem to form separately and then overlap to form a cluster of overlapping few-layer nanosheets. The nanosheets do not grow from a central core to form nanoflowers like in $MoSe_2$-OAm and $MoSe_2$-OAm/ODE. Fig. 5.15(a) and (b) illustrates the morphology of the nanoflowers from $MoSe_2$-OAm and $MoSe_2$-OAm/ODE as well as the overlapping few-layer nanosheets from$MoSe_2$-OAm/OA respectively.

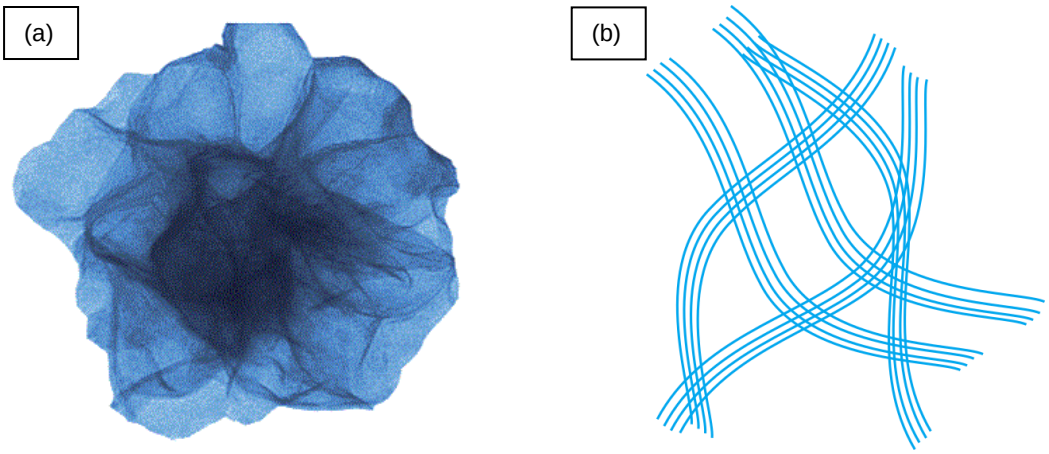

Figure 5.15: (a) $MoSe_2$ nanoflower synthesized using oleylamine ($MoSe_2$-OAm) and oleylamine in conjunction with 1-octadecene ($MoSe_2$-OAm/ODE), (b) an aggregate of individual overlapping few-layer nanosheets synthesized using oleylamine in conjunction with oleic acid ($MoSe_2$-OAm/OA).

The difference in the morphology of the nanostructures could be due to a difference in their mechanism of formation; these mechanisms are determined by the influence of the co-surfactant ODE and OA on the synthesis of the nanomaterials. The use of ODE does not change the morphology of the nanomaterials compared to the use of oleylamine alone, the formation of the nanoflowers seems to form by initially forming a dense central core at which point the nanosheets begin to grow outward as small lateral dimension nanosheets that fold in on each other to form something similar to a blooming flower from this central core. The introduction of ODE seems to increase the reactivity of the Se precursor which results in more nanosheets being formed from the central core. ODE has been known to form an intermediate with the Se monomer (Se-CHCHCH) that increases the reactivity of the monomer in colloidal synthesis, the increased reactivity of the monomer could result in more nanosheets being formed in each cluster of nanoflowers compared to the nanosheets formed using oleylamine alone, this result pertaining to the formation of nanoflowers and the effect of ODE are similar to results obtained by Sun *et al.*.[34] The use of OA in conjunction with oleylamine however gives the opposite result. The use of oleic acid seems to result in the formation of individual few-layer nanosheets that then agglomerate to form the clusters of overlapping few-layer nanosheets as observed in Fig. 517(f). This result is similar to the results found by Gao *et al.* when utilising the same surfactant combination.[35] This suggests that the surfactant affecting the morphology of the nanosheets is the oleic acid because the use of oleylamine alone in the synthesis forms nanoflowers. This can only be true if oleic acid was binding to the surface of the nanosheets instead of oleylamine. It has been proven by Harris *et al.* that oleic acid has a higher probability of binding to the metal in the reaction mixture compared to oleylamine.[17] This is due to the higher number of binding modes of oleic acid compared to oleylamine.[12]

5.4 Conclusion

In this study it is shown that the introduction of a co-surfactant in the synthesis of $MoSe_2$ nanomaterials does have an effect on the structure, optical properties and morphology of the nanomaterials. The introduction of oleic acid as suspected reduced the thickness of the nanosheets and therefore reduced the number of layers on the nanosheets. This slightly affected the optical properties of the nanomaterials as the samples containing oleic acid had a slightly larger blue-shift to the band-gap from the bulk compared to the other samples. The use of oleic acid also slightly affects the

morphology of the nanomaterials, they result in the formation of clusters overlapping few-layer nanosheets different from the nanoflowers obtained when oleylamine alone is used. The use of NMR spectroscopy was able to prove that oleic acid does indeed adsorb on the surface of the nanoparticles in the Oam/OA mixture. This confirms that the differences in the $MoSe_2$-OAm/OA nanoparticles compared to $MoSe_2$-OAm are due to the introduction of oleic acid in the synthesis of $MoSe_2$-OAm/OA. The use of 1-octadacene did not seem to affect the structure and optical properties of the nanomaterials which was to be expected as this surfactant does not contain a head group that can bind to the facts of the nanomaterials.

5.5 References

1. Lenart, V. M.; Gómez, S. L.; Calatayud, M. P.; Goya, G. R., Size and shape control of magnetite nanoparticles with a nonselective binding surfactants. *arXiv preprint arXiv:1402.1134* **2014**.
2. Calatayud, D. G.; Rodriguez, M.; Jardiel, T., Controlling the morphology of TiO 2 nanocrystals with different capping agents. *Boletín de la Sociedad Española de Cerámica y Vidrio* **2015,** *54* (4), 159-165.
3. Wang, N.; Wang, X.; Yang, L.; Chen, H., Morphology and size control of nanocalcium carbonate crystallised in reverse micelle system with cationic surfactant cetyltrimethylammonium bromide. *Micro & Nano Letters* **2013,** *8* (2), 94-98.
4. Nejo, A. O. Synthesis of organically capped and water-soluble metal sulfide semiconductor nanoparticles. University of Zululand, **2013**.
5. Mourdikoudis, S.; Liz-Marzán, L. M., Oleylamine in nanoparticle synthesis. *Chemistry of Materials* **2013,** *25* (9), 1465-1476.
6. Sperling, R. A.; Parak, W., Surface modification, functionalization and bioconjugation of colloidal inorganic nanoparticles. *Philosophical Transactions of the Royal Society of London A: Mathematical, Physical and Engineering Sciences* **2010,** *368* (1915), 1333-1383.
7. Zou, Y.; Li, D.; Yang, D., Shape and phase control of CdS nanocrystals using cationic surfactant in noninjection synthesis. *Nanoscale research letters* **2011,** *6* (1), 374.

8. DasariAyodhya, M.; Kumari, A. S.; Mangatayaru, K. G.; Veerabhadram, G., Synthesis, Characterization of ZnS nanoparticles by Coprecipitation method using various capping agents-Photocatalytic activity and Kinetic study.
9. Onwudiwe, D. C.; Hrubaru, M.; Ebenso, E. E., Synthesis, structural and optical properties of TOPO and HDA capped cadmium sulphide nanocrystals, and the effect of capping ligand concentration. *Journal of Nanomaterials* **2015,** *2015* (143632), 1-9.
10. Bakshi, M. S., How surfactants control crystal growth of nanomaterials. *Crystal Growth & Design* **2015,** *16* (2), 1104-1133.
11. Cara, C.; Musinu, A.; Mameli, V.; Ardu, A.; Niznansky, D.; Bursik, J.; Scorciapino, M. A.; Manzo, G.; Cannas, C., Dialkylamide as Both Capping Agent and Surfactant in a Direct Solvothermal Synthesis of Magnetite and Titania Nanoparticles. *Crystal Growth & Design* **2015,** *15* (5), 2364-2372.
12. Debroye, E.; Yuan, H.; Bladt, E.; Baekelant, W.; Van der Auweraer, M.; Hofkens, J.; Bals, S.; Roeffaers, M. B., Facile Morphology-Controlled Synthesis of Organolead Iodide Perovskite Nanocrystals Using Binary Capping Agents. *ChemNanoMat* **2017,** *3* (4), 223-227.
13. Zhou, X.; Jiang, J.; Ding, T.; Zhang, J.; Pan, B.; Zuo, J.; Yang, Q., Fast colloidal synthesis of scalable Mo-rich hierarchical ultrathin $MoSe_{2-x}$ nanosheets for high-performance hydrogen evolution. *Nanoscale* **2014,** *6* (19), 11046-11051.
14. Savjani, N.; Lewis, E. A.; Bissett, M. A.; Brent, J. R.; Dryfe, R. A.; Haigh, S. J.; O'Brien, P., Synthesis of Lateral Size-Controlled Monolayer 1 H-MoS_2@ Oleylamine as Supercapacitor Electrodes. *Chemistry of Materials* **2016,** *28* (2), 657-664.
15. Jung, W.; Lee, S.; Yoo, D.; Jeong, S.; Miró, P.; Kuc, A.; Heine, T.; Cheon, J., Colloidal synthesis of single-layer MSe_2 (M= Mo, W) nanosheets via anisotropic solution-phase growth approach. *Journal of the American Chemical Society* **2015,** *137* (23), 7266-7269.
16. Zhang, X.; Qiao, X.-F.; Shi, W.; Wu, J.-B.; Jiang, D.-S.; Tan, P.-H., Phonon and Raman scattering of two-dimensional transition metal dichalcogenides from monolayer, multilayer to bulk material. *Chemical Society Reviews* **2015,** *44* (9), 2757-2785.

17. Harris, R. A.; Shumbula, P. M.; van der Walt, H. t., Analysis of the interaction of surfactants oleic acid and oleylamine with iron oxide nanoparticles through molecular mechanics modeling. *Langmuir* **2015,** *31* (13), 3934-3943.
18. Soulsby, D.; Wallner, A. S., Introduction to NMR Spectroscopy in the Undergraduate Curriculum. In *NMR Spectroscopy in the Undergraduate Curriculum: First Year and Organic Chemistry Courses Volume 2*, ACS Publications, **2016,** 1-10.
19. Hens, Z.; Moreels, I.; Martins, J. C., In situ 1H NMR study on the trioctylphosphine oxide capping of colloidal InP nanocrystals. *ChemPhysChem* **2005,** *6* (12), 2578-2584.
20. Fritzinger, B.; Moreels, I.; Lommens, P.; Koole, R.; Hens, Z.; Martins, J. C., In situ observation of rapid ligand exchange in colloidal nanocrystal suspensions using transfer NOE nuclear magnetic resonance spectroscopy. *Journal of the American Chemical Society* **2009,** *131* (8), 3024-3032.
21. Fritzinger, B.; Capek, R. K.; Lambert, K.; Martins, J. C.; Hens, Z., Utilizing self-exchange to address the binding of carboxylic acid ligands to CdSe quantum dots. *Journal of the American Chemical Society* **2010,** *132* (29), 10195-10201.
22. . Zhou, M.; Zhang, Z.; Huang, K.; Shi, Z.; Xie, R.; Yang, W., Colloidal preparation and electrocatalytic hydrogen production of MoS_2 and WS_2 nanosheets with controllable lateral sizes and layer numbers. *Nanoscale* **2016,** *8* (33), 15262-15272.
23. Tonndorf, P.; Schmidt, R.; Böttger, P.; Zhang, X.; Börner, J.; Liebig, A.; Albrecht, M.; Kloc, C.; Gordan, O.; Zahn, D. R., Photoluminescence emission and Raman response of monolayer MoS_2, $MoSe_2$, and WSe_2. *Optics express* **2013,** *21* (4), 4908-4916.
24. Niu, L.; Li, K.; Zhen, H.; Chui, Y. S.; Zhang, W.; Yan, F.; Zheng, Z., Salt-Assisted High-Throughput Synthesis of Single-and Few-Layer Transition Metal Dichalcogenides and Their Application in Organic Solar Cells. *Small* **2014,** *10* (22), 4651-4657.
25. Dong, N.; Li, Y.; Feng, Y.; Zhang, S.; Zhang, X.; Chang, C.; Fan, J.; Zhang, L.; Wang, J., Optical limiting and theoretical modelling of layered transition metal dichalcogenide nanosheets. *Scientific reports* **2015,** *5*(14646), 1-10.

26. Mishra, A. K.; Lakshmi, K.; Huang, L., Eco-friendly synthesis of metal dichalcogenides nanosheets and their environmental remediation potential driven by visible light. *Scientific reports* **2015,** *5*, 15718.
27. Tongay, S.; Zhou, J.; Ataca, C.; Lo, K.; Matthews, T. S.; Li, J.; Grossman, J. C.; Wu, J., Thermally driven crossover from indirect toward direct bandgap in 2D semiconductors: $MoSe_2$ versus MoS_2. *Nano letters* **2012,** *12* (11), 5576-5580.
28. Zhang, Y.; Chang, T.-R.; Zhou, B.; Cui, Y.-T.; Yan, H.; Liu, Z.; Schmitt, F.; Lee, J.; Moore, R.; Chen, Y., Direct observation of the transition from indirect to direct bandgap in atomically thin epitaxial $MoSe_2$. *Nature nanotechnology* **2014,** *9* (2), 111-115.
29. Devaraj, M.; Saravanan, R.; Deivasigamani, R.; Gupta, V. K.; Gracia, F.; Jayadevan, S., Fabrication of novel shape Cu and Cu/Cu_2O nanoparticles modified electrode for the determination of dopamine and paracetamol. *Journal of Molecular Liquids* **2016,** *221*, 930-941.
30. Smolensky, E. D.; Park, H. Y. E.; Berquó, T. S.; Pierre, V. C., Surface functionalization of magnetic iron oxide nanoparticles for MRI applications–effect of anchoring group and ligand exchange protocol. *Contrast media & molecular imaging* **2011,** *6* (4), 189-199.
31. Georgiadou, V.; Kokotidou, C.; Le Droumaguet, B.; Carbonnier, B.; Choli-Papadopoulou, T.; Dendrinou-Samara, C., Oleylamine as a beneficial agent for the synthesis of $CoFe_2O_4$ nanoparticles with potential biomedical uses. *Dalton Transactions* **2014,** *43* (17), 6377-6388.
32. Johnson Jr, C. S., Diffusion ordered nuclear magnetic resonance spectroscopy: principles and applications. *Progress in Nuclear Magnetic Resonance Spectroscopy* **1999,** *34* (3-4), 203-256.
33. Lee, C.; Kwak, H.; Choi, E.; Hong, T.; Yoon, H.; Lee, Y.; Baik, K.; Uhm, H., Traces of isotopic reactive species produced from a non-thermal plasma jet in bio-molecules. *New Journal of Physics* **2015,** *17* (11), 113031.
34. Sun, D.; Feng, S.; Terrones, M.; Schaak, R. E., Formation and interlayer decoupling of colloidal $MoSe_2$ nanoflowers. *Chemistry of Materials* **2015,** *27* (8), 3167-3175.
35. Guo, W.; Chen, Y.; Wang, L.; Xu, J.; Zeng, D.; Peng, D.-L., Colloidal synthesis of $MoSe_2$ nanonetworks and nanoflowers with efficient electrocatalytic hydrogen-evolution activity. *Electrochimica Acta* **2017,** *231*, 69-76.

Chapter 6: Investigating the electrochemical properties of $MoSe_2$ few-layer nanosheets and nanoflowers for supercapacitor electrode applications.

6.1 Introduction

The importance of the stability of the electric grid on the economy has been made evident by the recent load-shedding situation in South Africa. Strategies to relieve stress on the electric grid caused by the growing demand for electricity are becoming increasingly important. The use of electric energy storage technologies (EES) can alleviate stress on the electric grid by storing energy when there is a surplus and quickly release that energy when the grid is under stress due to high demand.[1]One such energy storage technology is the supercapacitor. Supercapacitors are energy storage devices; the devices consist of two high surface area electrodes that are separated by a dielectric in an electrolyte.[1] Supercapacitor have the advantage of a high-power density and stability but suffer from a low energy density.[2-3] Activated carbon and other forms of carbon have been used as electrodes in supercapacitors.[4-5]In an effort to improve the energy density of the devices materials with a higher surface area are being explored, such as graphene.[4-5] Transition metal dichalcogenides (TMDs) such as MoS_2 nanomaterials are also being explored as alternatives to the use of activated carbon.[6] TMDs have a high surface to volume ratio (high surface area), the materials are highly stable and the layered nature of the material suggest the materials can achieve a high capacity.[7-8]MoS_2 has been a member of the TMDs that has been explored quite extensively as an electrode in supercapacitor.[9-10] $MoSe_2$ has not received as much attention but has been identified as excellent candidate for use as an electrode material in supercapacitor.[11] The material has been reported to have a higher intrinsic electrical conductivity than MoS_2 because selenium has more metallic character than sulfur. The material has also been reported to have a higher inter-layer distance which could help accommodate electrolyte ions.[12] The aim of this work was to firstly use novel colloidal synthetic techniques to synthesize $MoSe_2$ nanomaterials and secondly to test the suitability of these materials for use as electrodes in supercapacitors.

The synthesis of the materials was done in previous work (chapter 5). The materials were successfully synthesized using colloidal synthesis. Two different morphologies of the nanomaterials were synthesized namely (i) overlapping wrinkled few-layer

nanosheets and (ii) nanoflowers. The $MoSe_2$ nanomaterials were tested using various electrochemical tests namely cyclic voltammetry, galvanostatic charge-discharge and impedance spectroscopy. It has been reported that the 3D interconnected nature of the nanosheets in the nanoflower help to achieve a higher surface area and macropores which result in fast electrolyte transport and therefore better effective electrochemical utilization.[13-14] The electrochemical performance of the overlapping winkled nanosheets are compared to the performance of the nanoflowers to determine whether this is true for the $MoSe_2$ nanomaterials as well. The performance of the nanomaterials was also compared to the performance of $MoSe_2$ nanomaterials using other synthesis techniques.

6.2 Materials and methods

6.2.1 Chemicals

Molybdic acid ((H_2MoO_4), 85%, Sigma-Aldrich), selenourea (CH_4N_2Se, 98%, Sigma-Aldrich), 1-octadacene (ODE, 90%, Sigma-Aldrich), oleylamine (OAm, 70%, Sigma-Aldich) and oleic acid (OA, 90%, Sigma-Aldrich) were used as received without purification.

6.2.2 Synthesis of $MoSe_2$ nanomaterials

There are two different morphologies of the $MoSe_2$ nanomaterials that will be utilised. The two different morphologies were obtained by using two different co-surfactants with oleylamine in the synthetic procedure. The use of octadecene(ODE) as surfactant results in the formation of a nanoflower morphology for the $MoSe_2$ nanomaterials, this sample is named $MoSe_2$-OAm/ODE. The second sample is for the synthesis of randomly oriented overlapping wrinkled few-layer nanosheets, the co-surfactant used in this synthesis is oleic acid(OA).

Synthesis of $MoSe_2$ wrinkled few layer nanosheets($MoSe_2$-OAm/OA)

A three-neck round bottom flask was filled with 10 ml of oleylamine and 5 ml of oleic acid(OA), the mixture was degassed for 20 minutes under nitrogen. The temperature was increased to 50 ^oC and ~ 0.4 g (0.3 mmol) of selenourea was added to the reaction mixture and stirred for 10 mins. Molybdic acid (~ 0.2 g (0.15 mmol)) was added once the reaction temperature reached 220 ^oC, the temperature was then increased until

the desired temperature of 300 ^{o}C was reached. The reaction was run for 90 min, after which the product was collected and washed with toluene and ethanol by centrifugation.

Synthesis of $MoSe_2$ nanoflowers($MoSe_2$-OAm/ODE)

A three-neck round bottom flask was filled with 10 ml of oleylamine and 5 ml octadecene(ODE), the mixture was degassed for 20 minutes under nitrogen. The temperature was increased to 50 ^{o}C and ~ 0.4 g (3.0 mmol) of selenourea was added to the reaction mixture and stirred for 10 mins. Molybdic acid (~ 0.2 g (0.15 mmol)) was added once the reaction temperature reached 220 ^{o}C, the temperature was then increased until the desired temperature of 300 ^{o}C was reached. The reaction was run for 90 mins, after which the product was collected and washed with toluene and ethanol by centrifugation.

6.2.3 Preparation of electrodes and electrochemical measurements

The electrochemical measurements were performed in a three-electrode system. A Ag/AgCl electrode was used as the reference electrode, platinum wire was used as the auxiliary electrode and the working electrode was a modified glassy carbon electrode. The glassy carbon electrode was polished with alumina paste and sonicated in 1M H_2SO_4 for 30 mins. The ink or fresh dispersion of the sample was prepared by dispersing 5.0 mg of the $MoSe_2$ nanomaterials with carbon black in N-methyl pyrrolidinone (NMP). The dispersion was ultrasonicated for 25 mins before a micropipette was used to drop cast 10 µl of the dispersion onto the glassy carbon. This means that the loading of the sample on the glassy carbon electrode is ~ 0.1 mg, the electrode was dried for 20 mins and then left to cool. A blank measurement was initially made, this is to say electrochemical measurements were conducted on the dispersion without the sample being added in order to evaluate the effect of the carbon black and the solvent on the signal obtained.

6.2.4 Characterisation techniques

The phase purity, crystallinity and preferred crystal orientation of the products were examined by using XRD on a Bruker MeasSrv (D2-205530)/D2-205530 diffractometer using secondary graphite monochromated CoKα radiation (λ 1.78897 Å) at 30 kV/30 mA. Measurements were taken using a glancing angle of incidence detector at an

angle of 2°, for 2θ values over 10 - 90° in steps of 0.026° with a step time of 37 s and at a temperature of 25 °C. The sample sizes and morphologies were determined by the transmission electron microscopy (TEM) carried out on a FEI Technai T12 TEM microscopy operated at an acceleration voltage of 200 kV with a beam spot size of 20 - 100 nm in TEM mode. The measurements were carried out on a BASi epsilon E2(1231) in 1 M Na_2SO_4. The cyclic voltammetry measurements were performed at the range 0 – 600 mV at various scan rates (10-100 mV), the galvanostatic charge-discharge experiments were performed at the potential range 0 – 600 mV and the current densities applied were 1,2,3,4 and 5 Ag^{-1}. The impedance spectroscopy measurements were performed on a Autolab PGSTAT302N at a frequency range 0.1-10^5 Hz and at an amplitude of 5 mV. The total surface area and pore volume of the nanomaterials were ascertained using a Micromeritics TriStar Surface Area and Porosity Analyzer (Micromeritics Instrument Corp., Norcross, GA, USA).

6.3 Results and discussion

6.3.1 Structural characterization

The Powder X-ray diffraction (PXRD) was used to confirm the synthesis of $MoSe_2$ and to also determine the phase and composition of the nanomaterials. The PXRD confirms the formation of 2H hexagonal $MoSe_2$ nanomaterials (JCPDS card no: 03-065-3999). The (002) peak which appears at ~ 14° is a diffraction peak caused by the stacking of layers in the nanosheets and the absence of the peak suggests the formation of monolayer nanosheets.[15] The powder diffraction patterns for both the $MoSe_2$-OAm/OA and $MoSe_2$-OAm/ODE show the appearance of the (002) peak which suggests that multilayer nanosheets of the material has been formed as shown in Fig. 6.1.[15]

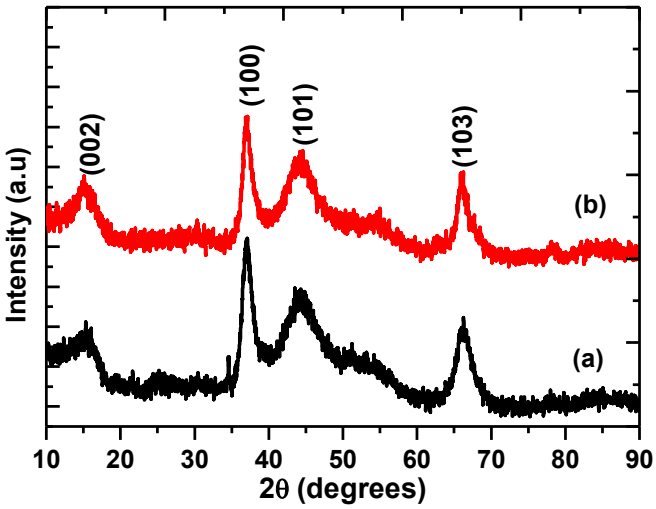

Figure 6.1: PXRD patterns of the synthesized nanomaterials: (a)$MoSe_2$-OAm/OA and (b) $MoSe_2$-OAm/ODE samples.

The thickness of the nanosheets can be approximated using the Debye-Sherrer equation. This can be done using the FWHM (full width at half maximum) of the (002) peaks which represents the interplanar spacing between the layers in the c-axis. The Debye-Sherrer equation can thus be used to approximate the crystallite size of the nanosheets along the c-axis which would be the thickness of the nanosheet.[16] The single layer thickness of the $MoSe_2$ nanosheets is ~0.65 nm.The number of layers in the $MoSe_2$-OAm/OA nanosheets was determined to be ~ 4 layers.[16] The number of layers in the $MoSe_2$-OAm/ODE was found to be ~ 5-6 layers. The higher number of layers for the $MoSe_2$-OAm/ODE could give it an advantage because it could allow for more electrolyte ions to intercalate between the layers leading to a higher capacitance.

Raman spectroscopy was used to identify whether the nanomaterial or the bulk material has been synthesized and to approximate the number of layers on the nanosheets. The Raman spectrum of $MoSe_2$ has two characteristic vibrational modes namely the out of plane A_{1g} at ~ 242 cm^{-1} and the in plane E^1_{2g} at ~ 286 cm^{-1}.[17] The A_{1g} peak red-shift from its position in the bulk as the number of layers is decreased and the E^1_{2g} has been known to blue-shift from its position in the bulk. How far the peaks shift can be used to approximate the number of layers on the nanosheets.[17]

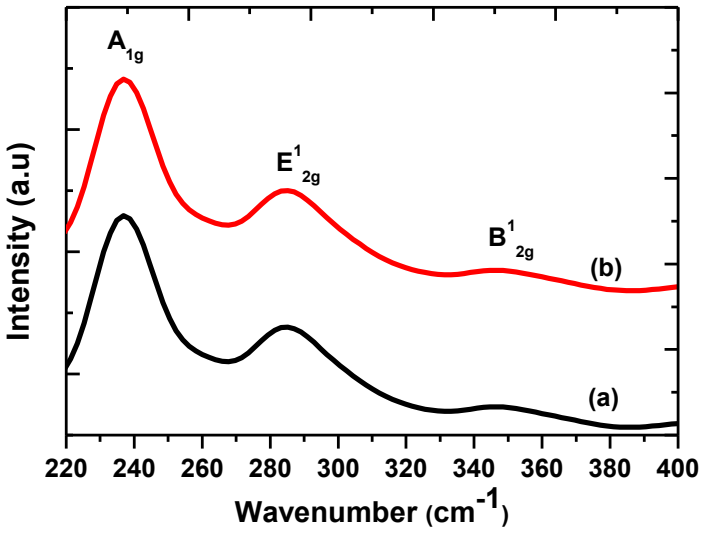

Figure 6.2: Raman spectra of the synthesized nanomaterials (a) $MoSe_2$-OAm/OA and (b) $MoSe_2$-OAm/ODE.

The Raman spectra also confirms the formation of $MoSe_2$ nanomaterials due to the appearance of the two characteristic peaks the A_{1g} and the E^1_{2g} peaks as show in Fig. 6.2. The red-shifting of the A_{1g} peak from the bulk is observed for both the nanosheets and the nanoflowers. The A_{1g} has red-shifted to 237 cm^{-1} for $MoSe_2$-OAm/OA and $MoSe_2$-OAm/ODE. This position for the A_{1g} has been found to suggest the formation of few-layer nanosheets.[18] The E^1_{2g} of the Raman spectrum of the nanosheets was found to be ~259 cm^{-1} which is associated with bi-layer nanosheets.[18] The appearance of the B^1_{2g} at ~ 350 cm^{-1} in the Raman spectra confirms that nanosheets are few-layer as the peak only appears for few-layer samples.[17] The PXRD confirms the formation of few-layer nanosheets because of the appearance pf the (002) peak, this along with the findings in the Raman spectra shows that few layer nanosheets have been formed. Unfortunately, the Raman spectra could not be used to confirm the difference in layer number between the $MoSe_2$-OAm/OA and the $MoSe_2$-OAm/ODE.

The TEM images of the $MoSe_2$-OAm/OA and $MoSe_2$-OAm/ODE are shown in Fig. 6.3.

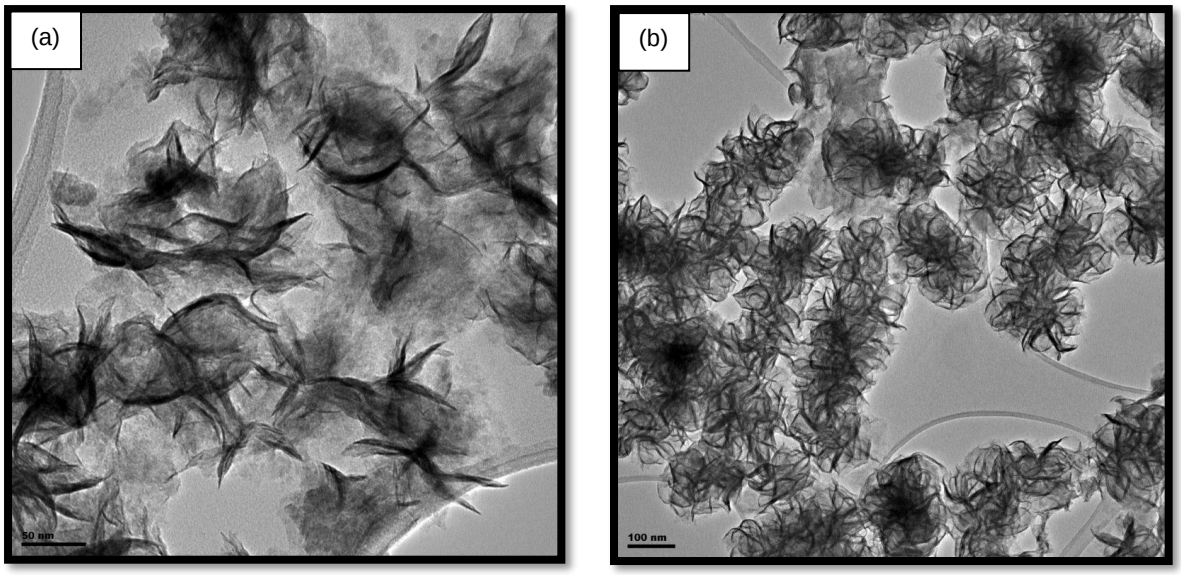

Figure 6.3: The TEM images of and (a) $MoSe_2$-OAm/OA sample and (b) The $MoSe_2$-OAm/ODE sample.

[19]The use of oleylamine and oleic acid results in the formation of small lateral dimension wrinkled few-layer nanosheets that have overlapped on top of each other. The nanosheets seem to grow individual and then agglomerate to form the structures shown in Fig. 6.3(a). The nanosheets do not grow from a central core to form nanoflowers like in $MoSe_2$-OAm/ODE. The use of oleylamine and 1-octadacene in the synthesis of $MoSe_2$-OAm/ODE on the other hand results in the formation of nanoflowers as shown in Fig. 6.3(b). The nanoflowers form due to the formation of a central core during the initial stages of the reaction, the nanosheets grow from this core to form a morphology resembling a blooming flower.[16] The effect of this slight difference in morphology on the electrochemical properties of the material was studies. As previously mentioned the nanoflowers are expected to have improved capacitance because of their morphology.

The Brunauer- Emmett-Teller(BET) surface area analysis was used to determine the surface area and the pore volume of the $MoSe_2$-OAm/ODE and $MoSe_2$-OAm/OA samples. Table 6.1 shows the values for the surface area and the pore volumes of the samples.

Table 6.1: The surface area and pore volume of the $MoSe_2$-OAm/ODE nanoflowers and the $MoSe_2$-OAm/OA nanosheets.

	$MoSe_2$-OAm/OA	$MoSe_2$-OAm/ODE
Surface area (m^2/g)	32.1599	38.3630
Pore Volume (cm^3/g)	0.198992	0.327217

The surface area and pore volume of the $MoSe_2$-OAm/ODE nanoflowers is higher than that of the $MoSe_2$-OAm/OA nanosheets. This is expected as the nanoflowers as mentioned have a 3D interconnected network of nanosheets that help them achieve a higher surface area than the $MoSe_2$-OAm/OA sample.[13] The pore volume of the nanoflowers is also higher which would result in the electrolyte ions easily diffusing into the inner surface of the material or intercalating in between the layers.

6.3.2 Electrochemical characterisation

Cyclic voltammetry was conducted to evaluate the capacitative performance of the nanomaterials. The shape of the CV curves determines whether Electric double layer capacitance(EDLC) behaviour or pseudocapacitative behaviour is observed in the nanomaterial. Rectangular shaped CV curves show typical EDLC behaviour while redox peaks in the CV curves shows pseudocapacitative behaviour.[20-21] The cyclic voltammetry measurements were conducted in 1 M Na_2SO_4 at the potential range 0 – 0.6 V, the measurements were also done at the scan rates 10, 25, 50, 75 and 100 mVs^{-1}. The CV curves for $MoSe_2$-OAm/OA and $MoSe_2$-OAm/ODE are shown in Fig. 6.4(a) and (b) respectively. Fig. 6.4(c) shows the CV curves of the two samples and the blank sample at a scan rate of 100 mVs^{-1}.

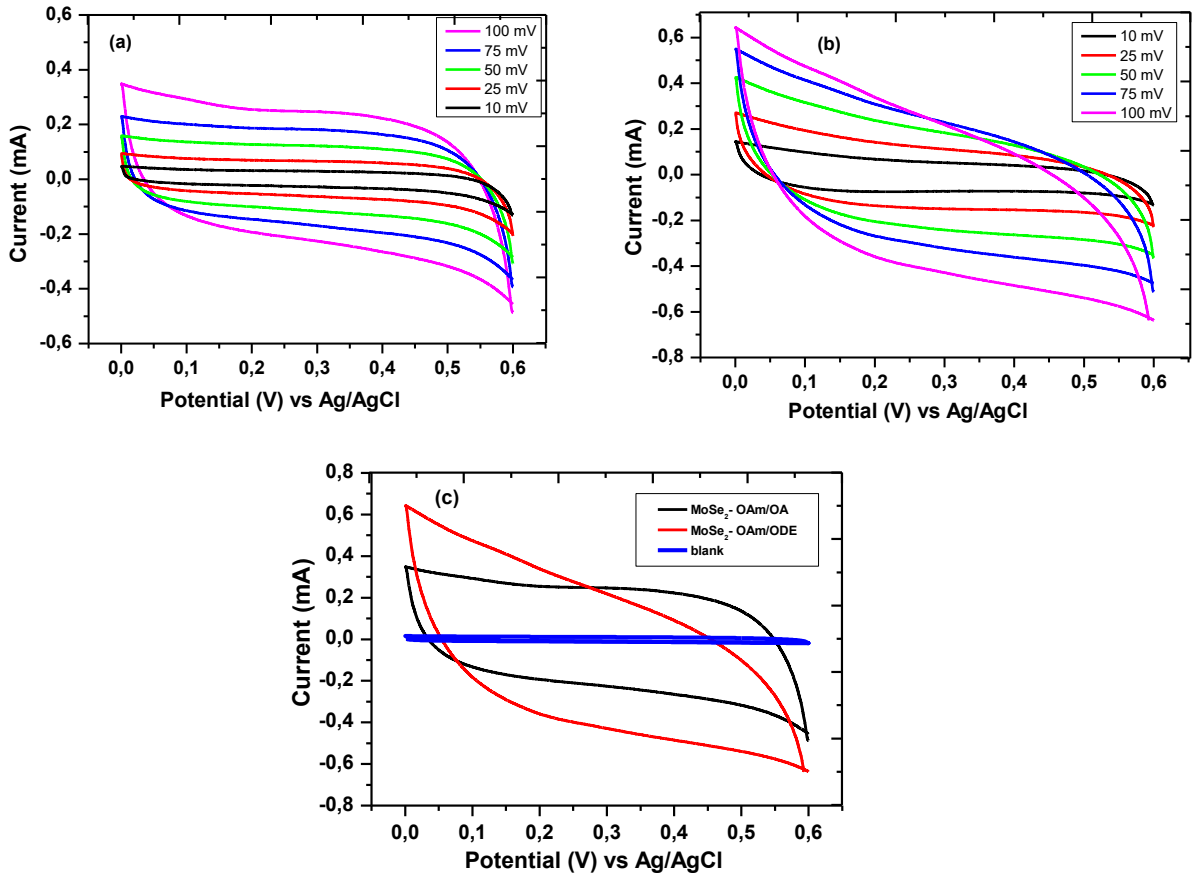

Figure 6.4: Cyclic voltammograms of (a) $MoSe_2$-OAm/OA nanosheets, (b) the $MoSe_2$-OAm/ODE nanoflowers at the scan rates 10, 25, 50, 75 and 100 mV and (c) is a plot of the cyclic voltammogram of the blank sample and the CV curves of the $MoSe_2$-OAm/OA nanosheets and the $MoSe_2$-OAm/ODE nanoflowers at a scan rate of 100 mV^{-1}.

The CV curves show near symmetrical rectangular loops at all scan rates as shown in Fig. 6.4(a) and (b), this suggests that the material is dominated by EDLC behaviour. The current response increases as the scan-rate is increased, this is expected as the $I \propto \sqrt{\nu}$. The current response of the blank sample as shown in Fig. 6.4(c) relative to that of the two other sample is negligible, this confirms that the current response of the samples containing the nanomaterials is largely due to the nanomaterials themselves. The CV curves obtained from $MoSe_2$-OAm/ODE begin to distort to some degree from the rectangular shapes at higher scan rates as observed in the CV curve at 100 mVs^{-1} in Fig. 6.4(c), this particular deviation is not observed in the CV curves of the $MoSe_2$-OAm/OA sample. This deviation has been reported to be due to the

intercalation of the metal ion in this case Na^+ in between the layers of the nanoflowers, this is a phenomenon that has been observed in the CV curves of various layered nanomaterials.[21] The effect of the intercalation of Na^+ seems to be more pronounced in the nanoflowers which could be due to the ability of the nanoflowers to accommodate for more Na^+ ions than the nanosheets. The galvanostatic charge-discharge curves were conducted to also evaluate the capacitative performance of the nanomaterials. The technique allows for the evaluation of the rate of the charge and discharge. The capacitance of the nanomaterials can be determined using the discharge step of a charge-discharge cycle.[22] The measurements were conducted at a potential range of 0 - 0.6 V at various current densities namely 1, 2, 3, 4 and 5 Ag^{-1} as shown in Fig. 6.5(a) and (b) For $MoSe_2$-OAm/OA and $MoSe_2$-OAm/ODE respectively.

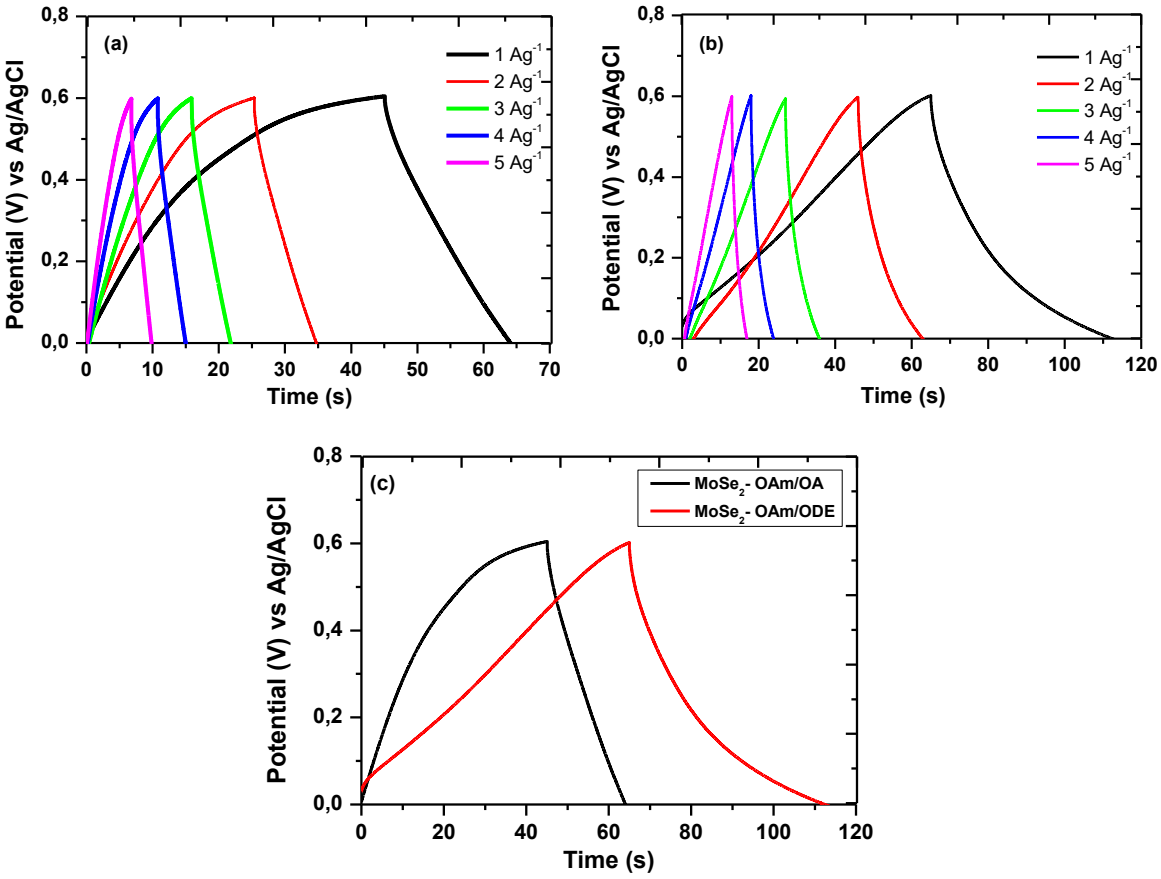

Figure 6.5: Charge-discharge cycles of (a) $MoSe_2$-OAm/OA nanosheets and (b) the $MoSe_2$-OAm/ODE nanoflowers and (c) is the charge-discharge cycle of both samples at 1 Ag^{-1}.

The discharge curves were used to determine the specific capacitance of the $MoSe_2$ nanomaterials with a nanosheet and nanoflower morphology.[16-17]The GCD curves show the expected nearly triangular symmetrical shape for $MoSe_2$-OAm/OA and the $MoSe_2$-OAm/ODE at the current densities 1, 2, 3, 4 and 5 Ag^{-1} as shown in Fig. 6.5(a) and (b) respectively.[16-17] At the beginning of the discharge step the curve show a pronounced potential or IR(internal resistance) drop as expected for capacitative behaviour in the nanomaterials.[20] The discharge curves were used to determine the specific capacitance of the $MoSe_2$ nanomaterials. The following equation was used to calculate the specific capacitance from the discharge curves:

$$C = \frac{I\,\Delta t}{m\Delta V} \tag{6.1}$$

Where *I* is the applied current, Δt is the time taken to discharge, m is the mass of the sample and ΔV is the potential range.

The specific capacitance the $MoSe_2$-OAm/OA was determined to be 30 Fg^{-1} for the nanosheets and 81 Fg^{-1} for the $MoSe_2$-ODE nanoflowers at 1 Ag^{-1}. The nanoflowers as expected show a greater capacitance compared to the wrinkled few-layer nanosheets. This again is attributed to the advantages of having a flower like morphology compared to the usual wrinkled few-layer nanosheets. The nanoflowers have been shown to have a higher surface area than the nanosheets. This along with a higher pore volume ensures the $MoSe_2$-OAm/ODE nanoflowers have better charge storage capabilities than the $MoSe_2$-OAm/OA nanosheets.[22]The specific capacitance obtained is comparable to the specific capacitance obtained by Balasingam *et al.* which was found to be 41.5 Fg^{-1} at a current density of 0.1 Ag^{-1} for $MoSe_2$ nanosheets synthesized using a hydrothermal method.[22] However, Jia et al were able to obtain a specific capacitance of 272 Fg^{-1} from $MoSe_2$ microspheres synthesized using a solvothermal method without the use of surfactants.[23] The $MoSe_2$ nanomaterials synthesized by Jia *et al.* were found to show pseudocapacitative behaviour which has been known to result in higher specific capacitance values when compared with materials showing only EDLC behaviour. It should also be noted that these nanomaterials were synthesized without the use of surfactants. The relationship

between the specific capacitance and the current density of the $MoSe_2$ samples is shown in Fig. 6.6. The capacitance of the material decreases as the current density is increased, the capacitance decreases by 80 % from 1 to 5 Ag^{-1} for the $MoSe_2$-OAn/OA samples and by 32% for the $MoSe_2$-OAm/ODE sample.

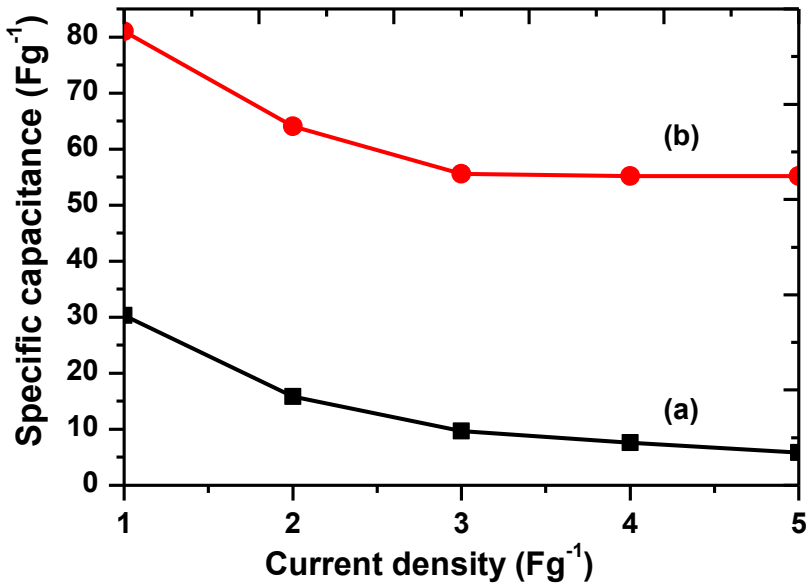

Figure 6.6: The capacitance retention of the nanomaterials at various current densities of the $MoSe_2$-OAm/OA nanosheets (a) and the $MoSe_2$-OAm/ODE nanoflowers (b).

The capacity retention of the $MoSe_2$-OAm/ODE nanoflowers is comparable to that reported by Balasingam *et al.* which was 63%.[20]The decrease of the capacitance of the material as the current densities is increased is due to an increase in the internal resistance of the electrode.[22] It could also be due to insufficient time available for electrolyte ions to diffuse into the inner electrode surface, the capacitance would then be reduced as the electrolyte ions only interact with the surface of the electrode.[22] The capacitance retention at higher current densities of the $MoSe_2$-OAm/ODE nanoflowers is shown to be superior to that of the $MoSe_2$-OAm/OA nanosheets. The 3D interconnected network of the nanoflowers allows for faster diffusion of the electrolyte ions so the ions are able to diffuse much faster into inner electrode surface so the capacitance retention should be higher than that of the nanosheets. Impedance

spectroscopy gives information about the internal resistance of the electrode material as well as the resistance between the electrode material and the electrolyte.[24] It also gives insight into the carrier transport properties of the system. Nyquist plots of the nanomaterials shown in Fig. 6.6 were obtained at an amplitude of 5 mV and a frequency range between 0.1 to 10^5 Hz.

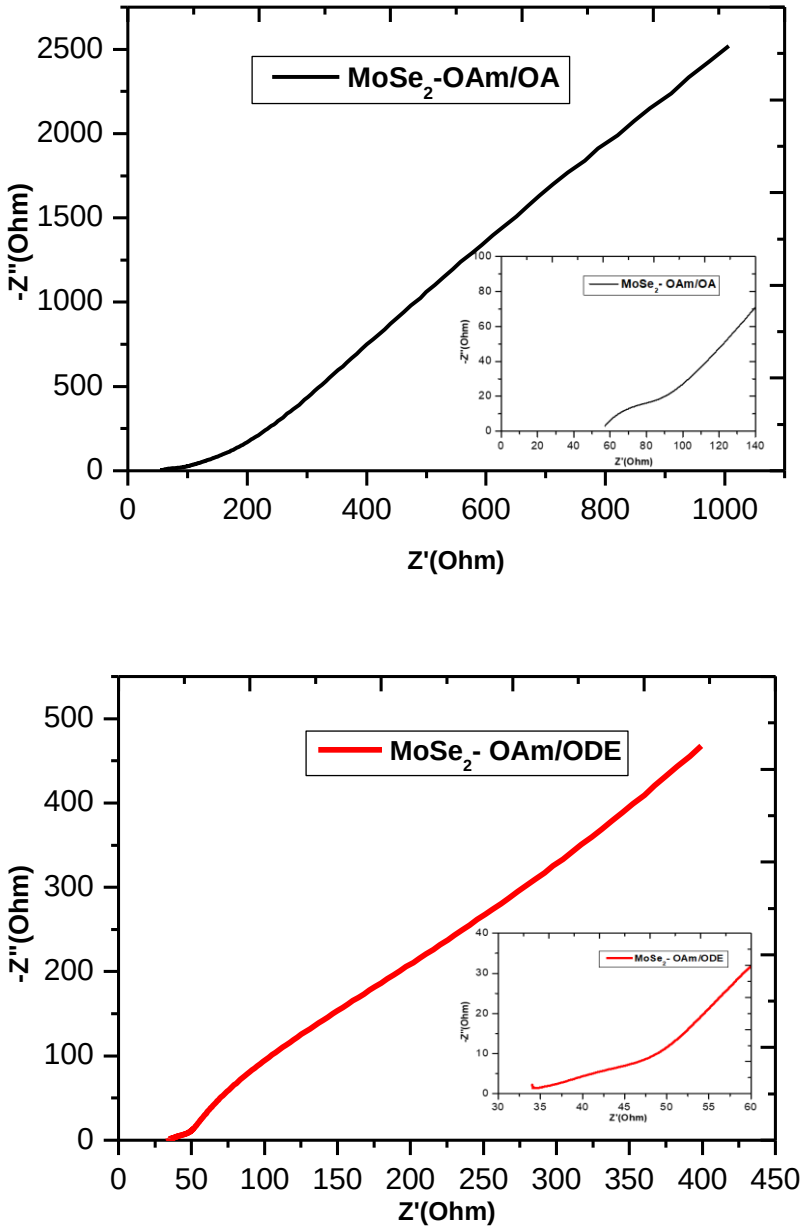

Figure 6.7: Nyquist plots and the corresponding zoomed in view at -Z ~ 0 Ω, (a) for the network of $MoSe_2$-OAm/OA nanosheets and (b) $MoSe_2$-OAm/ODE nanoflowers.

The Nyquist plot for $MoSe_2$-OAm/OA is shown in Fig. 6.7(a) and that of $MoSe_2$-OAm-ODE is shown in Fig. 6.7(b). The Nyquist plots of the nanomaterials shows typical supercapacitor behaviour. The high frequency region consists of a semi-circle which relates to the charge transfer resistance, the smaller the diameter of the semi-circle the smaller the charge transfer resistance.[21] The charge transfer resistance is associated with the resistance to the transfer of charge from the electrolyte to the electrode. The semicircle in the high frequency regions can be seen in the zoomed in images shown inside the Nyquist plots of the respective samples. The diameter of the semi-circle for the $MoSe_2$-OAm/ODE was found to be smaller than that of the $MoSe_2$-OAm/OA. The charge transfer resistance of the MoS_2-OAm/ODE nanoflower sample is lower than that of the $MoSe_2$-OAm/OA nanosheets. The lower charge transfer resistance would also contribute to the improved capacitance of the material as the ions would have less resistance when interacting with the electrode surface. The low frequency region of the Nyquist plots shows straight nearly vertical lines which is expected for ideal supercapacitor behaviour. The equivalent series resistance(ESR) is an important parameter for supercapacitor materials, it refers to the resistance for the components of the supercapacitor such as the resistance between the electrodes and the electrolyte. The ESR values can be determined by reading the value where the curve intersects the x-axis which represents the real impedance. The ESR values for the $MoSe_2$-OAm/OA was determined to be ~ 57.1 Ω and 34.0 Ω for the $MoSe_2$-OAm/ODE. The ESR of the $MoSe_2$-OAm/ODE is slightly lower than that of the $MoSe_2$-OAm/OA, this could be due to the higher capacitative capabilities of the nanoflowers compared to the nanosheets. The ions of the electrolyte would easily be able to access the inner surface of the electrodes in the nanoflowers and would diffuse more easily into the layers of the nanoflowers compared to the nanosheets which explains why the ESR of the $MoSe_2$-OAm/ODE nanoflowers is much lower than that of the $MoSe_2$-OAm/OA nanosheets. The ESR values for the samples are quite high compared to ESR values of other supercapacitor nanomaterials including $MoSe_2$ synthesized using other synthesis techniques.[22-23] TMDs are known to have low conductivity but their ESR are much lower than those found in this study. A comparison of the specific capacitance of the materials in this work and that of materials in other work synthesized using other techniques is shown in table 6.2.

Table 6.2: Comparison of the specific capacitance MoS_2 and $MoSe_2$ electrodes from nanomaterials synthesized through different routes and the route used in this work

Material	Synthetic procedure	Morphology	ESR	Specific capacitance	Reference
MoS_2	Hydrothermal	Flower like	< 4 Ω	162 Fg^{-1} at 1Ag^{-1} In 1 M KCl	[26]
MoS_2	Chemical bath deposition(CBD)	Ultrathin nanosheets	8.50 Ω	214.28 Fg^{-1} at 1.7 Ag^{-1} in 0.5 M Na_2SO_4	[27]
$MoSe_2$	Hydrothermal	nanosheets	1.16 Ω	41.5 Fg^{-1} at 0.1 Ag^{-1} in 0.5 M H_2SO_4	[22]
$MoSe_2$	Solvothermal method	Microspheres	10.41 Ω	272 Fg^{-1} at 1 Ag^{-1} in 3 M KOH	[23]
$MoSe_2$	**This work**	**Nanosheets**	57.1 Ω	31 Fg^{1} at 1 Ag^{-1} in 1 M Na_2SO_4	
$MoSe_2$	**This work**	**Nanoflowers**	34.0 Ω	81 Fg^{-1} at 1 Ag^{-1} in 1 M Na_2SO_4	

This could be due to the use of surfactants in the colloidal synthesis of the nanomaterials which would impede the adsorption of the electrolyte ions on the surface of the nanomaterials.[25] This would negatively affect the storage capabilities of the materials as evidenced by the low capacitance of the materials compared to other supercapacitor electrode materials including $MoSe_2$ synthesized using other synthetic techniques.[23] Guo *et al.* stress the importance of the removal of the capping agent in their electrochemical testing of $MoSe_2$ nanomaterials for Hydrogen evolution reactions (HER) applications.[19]

6.4 Conclusion

A study of the electrochemical properties of the $MoSe_2$ nanomaterials are dominated by EDLC behaviour which is confirmed by the CV curves of both the $MoSe_2$-OAm/OA and the $MoSe_2$-OAm/ODE. The specific capacitance calculated from the discharge curve of the charge-discharge cycle for the $MoSe_2$-OAm/OA nanosheets (30 Fg^{-1}) was lower than that of the $MoSe_2$-OAm/ODE nanoflowers (81 Fg^{-1}). This was the expected result due to the fact that the flower like morphology allows for faster electrolyte transport compared to the nanosheets. The 3D interconnected network of nanosheets in the $MoSe_2$-OAm/ODE nanoflowers does result in a higher surface area compared to the $MoSe_2$-OAm/OA nanosheets. Overall the electrochemical performance of the $MoSe_2$-Oam/ODE nanoflowers was much superior to that of the $MoSe_2$-OAm/OA nanosheets. The capacitance was however much lower than expected compared to the capacitance reported in literature for MoS_2 or $MoSe_2$ nanomaterials synthesized using other synthetic techniques.[23,27] The equivalent series resistance(ESR) was also much higher for the $MoSe_2$ synthesized in this study compared to that of the $MoSe_2$ synthesized using other synthetic techniques.[23] The use of capping agents in the system that adsorb on the surface of the nanomaterials essentially reducing the available surface area for the electrolyte ions to adsorb. This has been identified as the likely cause for the low capacitance observed in these materials.

6.5 References

1. Farhadi, M.; Mohammed, O., Energy storage technologies for high-power applications. *IEEE Transactions on Industry Applications* **2016,** *52* (3), 1953-1961.
2. Schneuwly, A.; Gallay, R., Properties and applications of supercapacitors: From the state-of-the-art to future trends. *Rossens, Switzerland* **2000**.
3. Basri, N.; Dolah, B., Physical and electrochemical properties of supercapacitor electrodes derived from carbon nanotube and biomass carbon. *Int. J. Electrochem. Sci* **2013,** *8*, 257-273.
4. Halper, M. S.; Ellenbogen, J. C., Supercapacitors: A brief overview. *The MITRE Corporation, McLean, Virginia, USA* **2006**, 1-34.
5. Tan, Y. B.; Lee, J.-M., Graphene for supercapacitor applications. *Journal of Materials Chemistry A* **2013,** *1* (47), 14814-14843.

6. Bissett, M. A.; Worrall, S. D.; Kinloch, I. A.; Dryfe, R. A., Comparison of two-dimensional transition metal dichalcogenides for electrochemical supercapacitors. *Electrochimica Acta* **2016,** *201*, 30-37.
7. Tiwari, A., *Advanced 2D Materials*. John Wiley & Sons: 2016.
8. Wang, H.; Wang, L.; Wang, X.; Quan, J.; Mi, L.; Yuan, L.; Li, G.; Zhang, B.; Zhong, H.; Jiang, Y., High quality $MoSe_2$ nanospheres with superior electrochemical properties for sodium batteries. *Journal of The Electrochemical Society* **2016,** *163* (8), A1627-A1632.
9. Savjani, N.; Lewis, E. A.; Bissett, M. A.; Brent, J. R.; Dryfe, R. A.; Haigh, S. J.; O'Brien, P., Synthesis of Lateral Size-Controlled Monolayer 1 H-MoS_2@ Oleylamine as Supercapacitor Electrodes. *Chemistry of Materials* **2016,** *28* (2), 657-664.
9. Huang, K.-J.; Zhang, J.-Z.; Shi, G.-W.; Liu, Y.-M., Hydrothermal synthesis of molybdenum disulfide nanosheets as supercapacitors electrode material. *Electrochimica Acta* **2014,** *132*, 397-403.
10. Huang, K.-J.; Zhang, J.-Z.; Fan, Y., Preparation of layered $MoSe_2$ nanosheets on Ni-foam substrate with enhanced supercapacitor performance. *Materials Letters* **2015,** *152*, 244-247.
11. Eftekhari, A., Molybdenum diselenide ($MoSe_2$) for energy storage, catalysis, and optoelectronics. *Applied Materials Today* **2017,** *8*, 1-17.
12. Wang, R.; Jayakumar, A.; Xu, C.; Lee, J.-M., $Ni(OH)_2$ nanoflowers/graphene hydrogels: a new assembly for supercapacitors. *ACS Sustainable Chemistry & Engineering* **2016,** *4* (7), 3736-3742.
13. Cheng, M.; Fan, H.; Xu, Y.; Wang, R.; Zhang, X., Hollow Co_2P nanoflowers assembled from nanorods for ultralong cycle-life supercapacitors. *Nanoscale* **2017,** *9* (37), 14162-14171.
14. Zhou, M.; Zhang, Z.; Huang, K.; Shi, Z.; Xie, R.; Yang, W., Colloidal preparation and electrocatalytic hydrogen production of MoS_2 and WS_2 nanosheets with controllable lateral sizes and layer numbers. *Nanoscale* **2016,** *8* (33), 15262-15272.
15. Sun, D.; Feng, S.; Terrones, M.; Schaak, R. E., Formation and interlayer decoupling of colloidal $MoSe_2$ nanoflowers. *Chemistry of Materials* **2015,** *27* (8), 3167-3175.

16. Hill, H. M., *Probing Transition Metal Dichalcogenide Monolayers and Heterostructures by Optical Spectroscopy and Scanning Tunneling Spectroscopy*. Columbia University: **2016**.
17. Niu, L.; Li, K.; Zhen, H.; Chui, Y. S.; Zhang, W.; Yan, F.; Zheng, Z., Salt-Assisted High-Throughput Synthesis of Single-and Few-Layer Transition Metal Dichalcogenides and Their Application in Organic Solar Cells. *Small* **2014,** *10* (22), 4651-4657.
18. Guo, W.; Chen, Y.; Wang, L.; Xu, J.; Zeng, D.; Peng, D.-L., Colloidal synthesis of $MoSe_2$ nanonetworks and nanoflowers with efficient electrocatalytic hydrogen-evolution activity. *Electrochimica Acta* **2017,** *231*, 69-76.
19. Wu, Z.; Li, B.; Xue, Y.; Li, J.; Zhang, Y.; Gao, F., Fabrication of defect-rich MoS_2 ultrathin nanosheets for application in lithium-ion batteries and supercapacitors. *Journal of Materials Chemistry A* **2015,** *3* (38), 19445-19454.
20. Choudhary, N.; Li, C.; Chung, H.-S.; Moore, J.; Thomas, J.; Jung, Y., High-Performance One-Body Core/Shell Nanowire Supercapacitor Enabled by Conformal Growth of Capacitive 2D WS_2 Layers. *ACS nano* **2016,** *10* (12), 10726-10735.
21. Stoller, M. D.; Ruoff, R. S., Best practice methods for determining an electrode material's performance for ultracapacitors. *Energy & Environmental Science* **2010,** *3* (9), 1294-1301.
22. Balasingam, S. K.; Lee, J. S.; Jun, Y., Molybdenum diselenide/reduced graphene oxide based hybrid nanosheets for supercapacitor applications. *Dalton Transactions* **2016,** *45* (23), 9646-9653.
23. Jia, J.; Wu, J.; Dong, J.; Tu, Y.; Lan, Z.; Fan, L.; Wei, Y., High-performance molybdenum diselenide electrodes used in dye-sensitized solar cells and supercapacitors. *IEEE Journal of Photovoltaics* **2016,** *6* (5), 1196-1202.
24. Oz, A.; Hershkovitz, S.; Tsur, Y. In *Electrochemical impedance spectroscopy of supercapacitors: A novel analysis approach using evolutionary programming*, AIP Conference Proceedings, *AIP*, **2014**, 76-80.
25. Li, D.; Wang, C.; Tripkovic, D.; Sun, S.; Markovic, N. M.; Stamenkovic, V. R., Surfactant removal for colloidal nanoparticles from solution synthesis: the effect on catalytic performance. *Acs Catalysis* **2012,** *2* (7), 1358-1362.

26. Wang, X.; Ding, J.; Yao, S.; Wu, X.; Feng, Q.; Wang, Z.; Geng, B., High supercapacitor and adsorption behaviors of flower-like MoS_2 nanostructures. *Journal of Materials Chemistry A* **2014,** *2* (38), 15958-15963.
27. Karade, S. S.; Dubal, D. P.; Sankapal, B. R., MoS_2 ultrathin nanoflakes for high performance supercapacitors: room temperature chemical bath deposition (CBD). *RSC Advances* **2016,** *6* (45), 39159-39165.

Chapter 7: Conclusions and future work

7.1 Conclusions

In this dissertation, colloidal synthesis was explored as a suitable synthetic method for the synthesis of molybdenum diselenide nanomaterials. The effects of the various reaction parameters in the system on the structural, optical, morphological and electrochemical properties were investigated. The electrochemical properties of the nanomaterials were investigated to assess whether the $MoSe_2$ nanomaterials synthesized using the colloidal synthesis would be suitable for use as electrode materials in supercapacitors. The effect of morphology on the electrochemical performance of the $MoSe_2$ nanomaterial was also investigated. A colloidal synthetic method was developed to synthesize the nanomaterials. This was initially accomplished through the thermal decomposition of molybdenum hexacarbonyl and selenourea in oleylamine at 300 °C. Well defined wrinkled Few-layer nanosheets of $MoSe_2$ were synthesized. The reaction time study revealed that a flocculate is formed in the initial stages of the reaction (30 min) containing an amorphous mixture of the starting materials. As the duration of the reaction is prolonged the flocculate is consumed to form the wrinkled few-layer nanosheets after the reaction was allowed to continue for 90 mins. When the metal precursor is changed from molybdenum hexacarbonyl to molybdic acid the morphology of the nanomaterials changes from the wrinkled few-layer nanosheets to a nanoflower morphology. The nanoflowers are formed from a central core that is formed at the initial stages of the reaction. Molybdic acid was used for the proceeding studies as it is a cheaper reagent, the nanomaterials could be synthesized at lower temperatures and nanoflowers are known to be a more desired morphology for use in supercapacitors. The introduction of a co-surfactants in the reaction system resulted in structural changes in the nanomaterials. The introduction of oleic acid as a co-surfactant resulted in a reduction of the thickness of the nanosheets and a slight change in the optical and morphological properties of the nanomaterials. The introduction of 1-octadacene did not result in any changes in the morphology or the optical and structural properties of the nanomaterials. The introduction of 1-octadacene did result in a heightened reactivity of the Se monomer forming nanoflowers with a denser central core. The electrochemical properties of the nanomaterials were evaluated and it was found that the nanoflower morphology of the nanomaterials had superior electrochemical properties compared to the few-layer

nanosheets. The specific capacitance of the $MoSe_2$ nanoflowers was found to be 81 Fg^{-1} while the few-layer nanosheets had a specific capacitance of 30 Fg^{-1}. The $MoSe_2$ nanoflowers had superior electrochemical performance to other $MoSe_2$ counterparts in literature synthesized using other means but inferior to $MoSe_2$ microspheres synthesized through a solvothermal method. This inferior performance compared to the microspheres has been attributed in part to the use of surfactants in colloidal synthesis that adsorb on the surface of the nanomaterials which block sites for electrolyte ions to adsorb.

7.2 Recommendations

- The colloidal synthetic method developed in this work could be adapted for use in the synthesis of other transition metal dichalcogenides such as MoS_2, WS_2 and WSe_2. This could be used as a simple and adaptable method for the synthesis of such nanomaterials.
- The use of DOSY spectroscopy and NOE spectroscopy to further study the capping of oleylamine molecules on the surface of nanoparticles in the presence of other surfactants such as oleic acid.
- The surfactants can be removed from the surface of the nanomaterials by various methods such as acid prickling and annealing to improve the electrochemical performance of the nanomaterials.
- The use of the transition metal dichalcogenides synthesized using colloidal synthesis could be used in other applications such as photovoltaic devices, other energy storage devices, hydrogen evolution reactions and photocatalytic degradation.

Appendix

Chapter 4

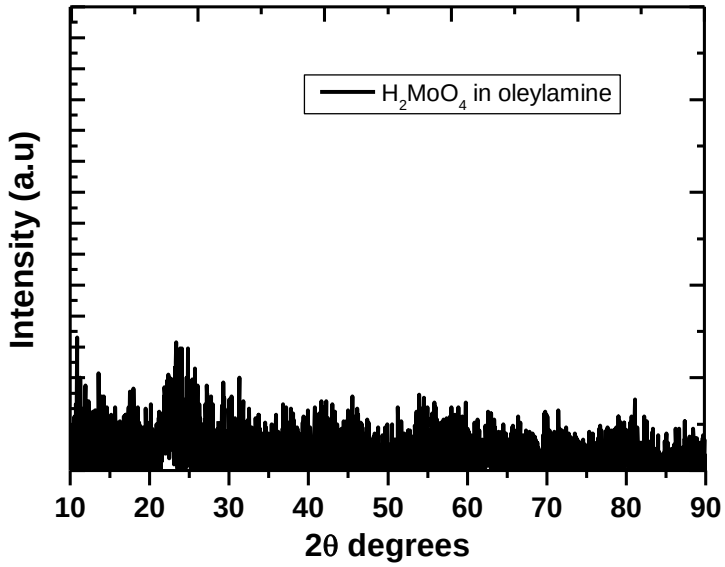

Figure A4.1: The PXRD pattern of the product obtained when H_2MoO_4 heated in oleylamine at 300 °C.

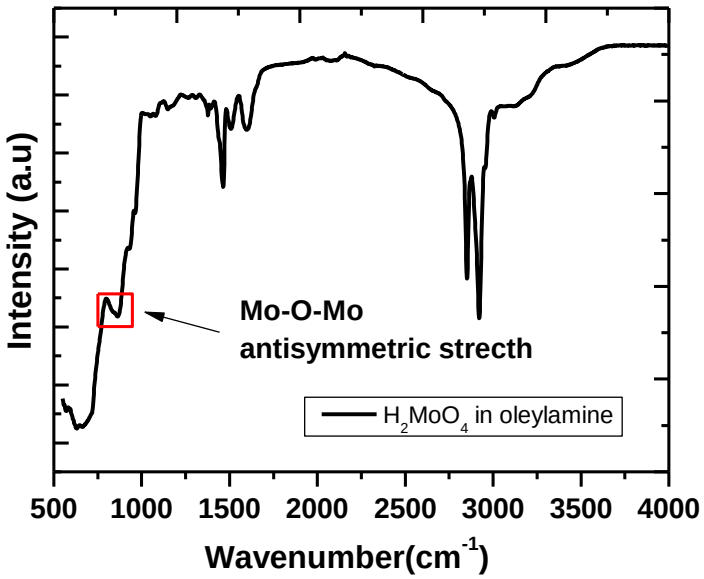

Figure A4.2: The FTIR spectrum of the product obtained when H_2MoO_4 heated in oleylamine at 300 °C.

Chapter 5

The 1D ^{1}H NMR spectra of free(unbound) surfactants. The assignments of the resonance peaks for the various surfactants is also shown. The ^{1}H NMR spectrum of free oleylamine is shown in Fig. A5.1, The ^{1}H NMR spectrum of free of 1-octadacene is shown in Fig. A5.2 and the ^{1}H NMR spectrum of free oleic acid is shown in Fig. A5.3.

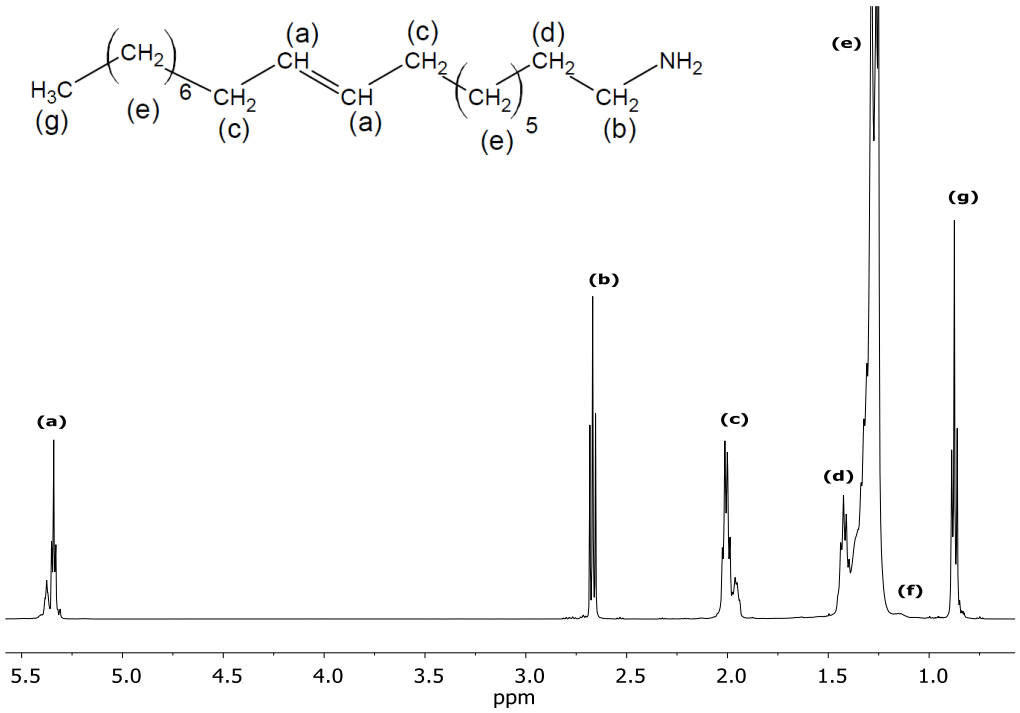

Figure A5.1: ^{1}H NMR spectrum of free oleylamine with the assigned resonance peaks for the respective protons.

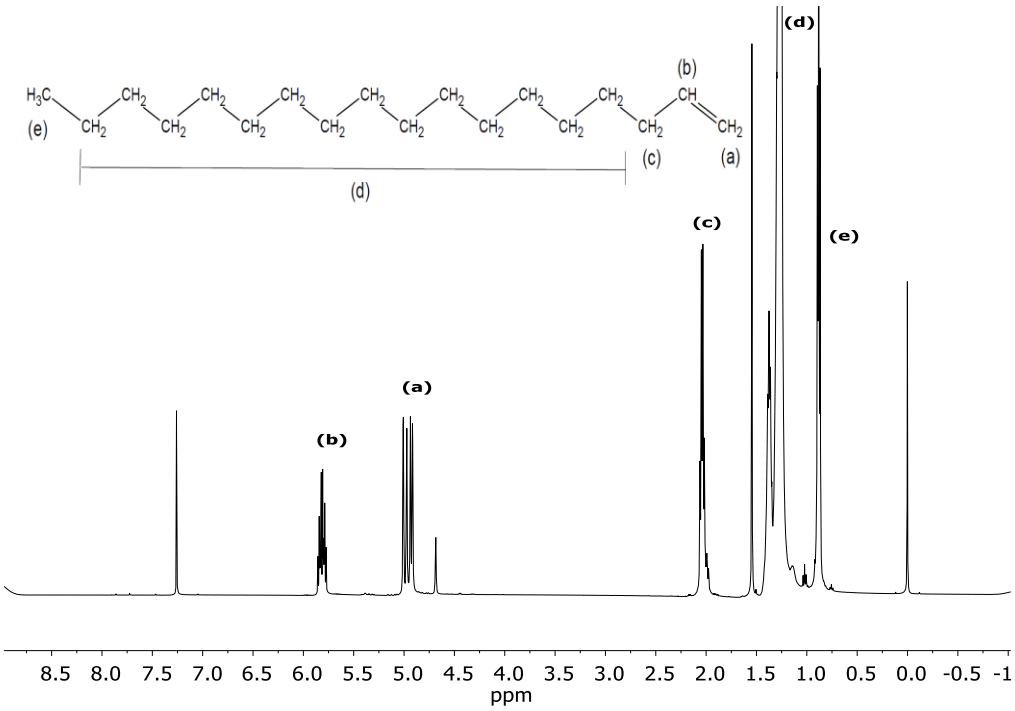

Figure A5.2: ^{1}H NMR spectrum of free 1-octadacene with the assigned resonance peaks for the respective protons.

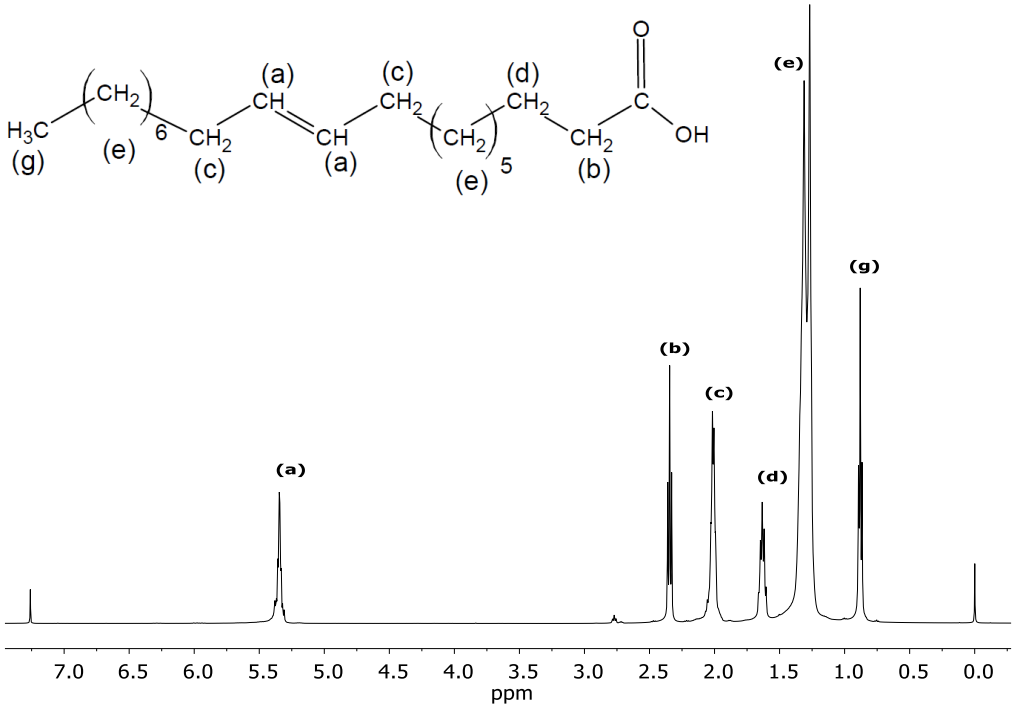

Figure A5.3: ^{1}H NMR spectrum of free oleic acid with the assigned resonance peaks for the respective protons.

The Diffusion ordered NMR spectroscopy (DOSY) was used to determine the diffusion coefficient of the free surfactants and the nanomaterials. The DOSY spectra of the free surfactants oleylamine and 1-octadacene are shown in Fig. A5.4 and Fig. A5.5. The bottom axis shows the chemical shifts of the oleylamine resonance peaks and the right axis shows the diffusion constant for the resonance peaks.

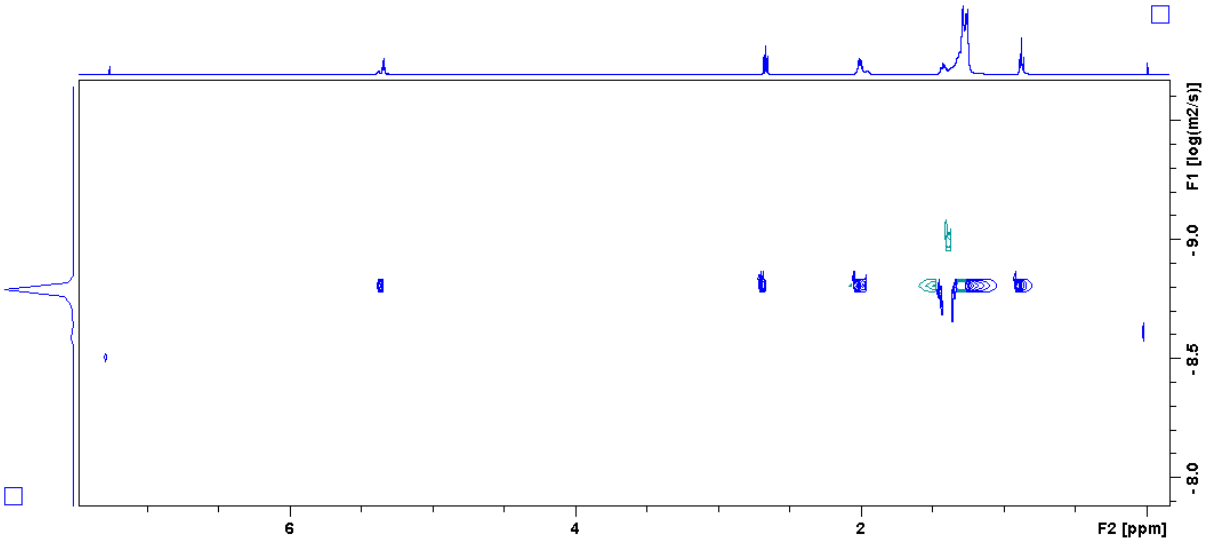

Figure A5.4: DOSY spectrum of free oleylamine. The resonance peaks from the oleylamine line up to give the same diffusion coefficient.

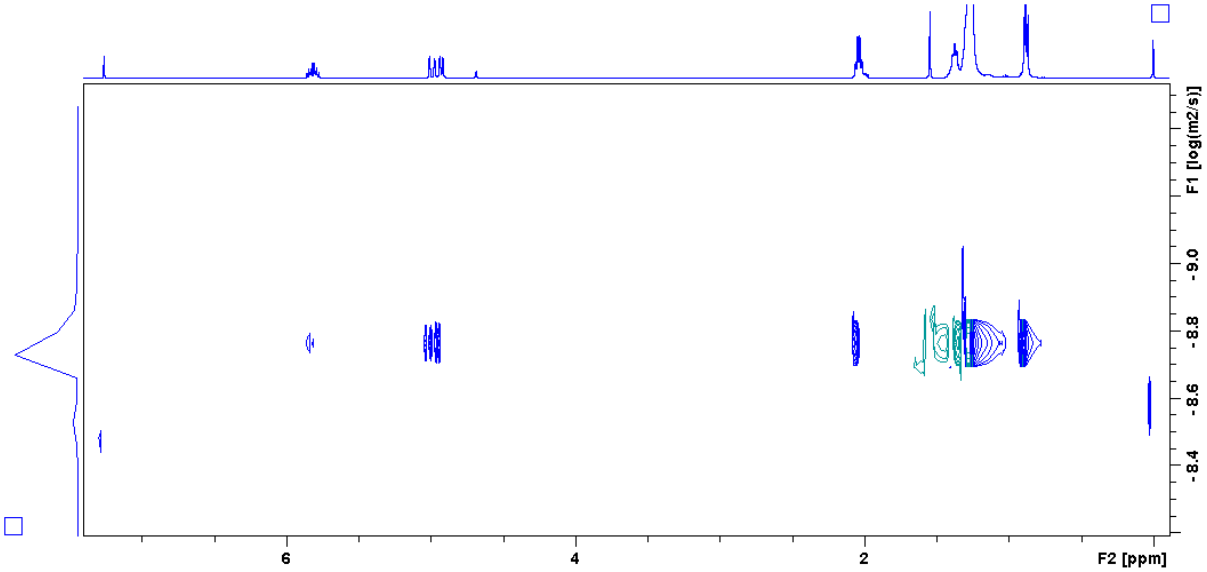

Figure A5.5: DOSY spectrum of 1-octadacene.

The DOSY spectrum of the nanomaterials were also obtained. The DOSY spectra of $MoSe_2$-OAm and $MoSe_2$-OAm/ODE are shown in Fig. A5.6 and Fig. A5.7.

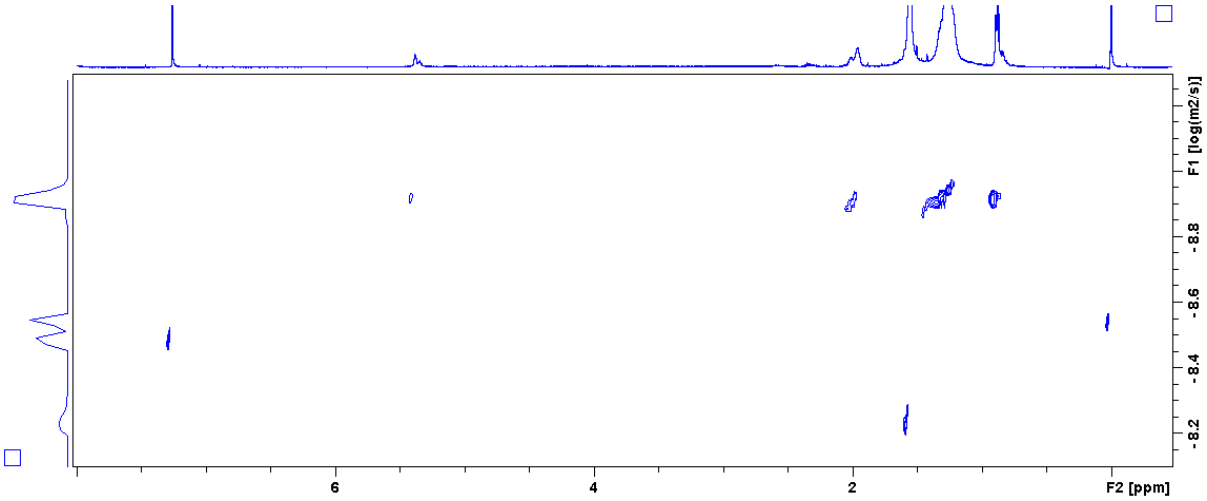

Figure A5.6: DOSY spectrum of $MoSe_2$-OAm.

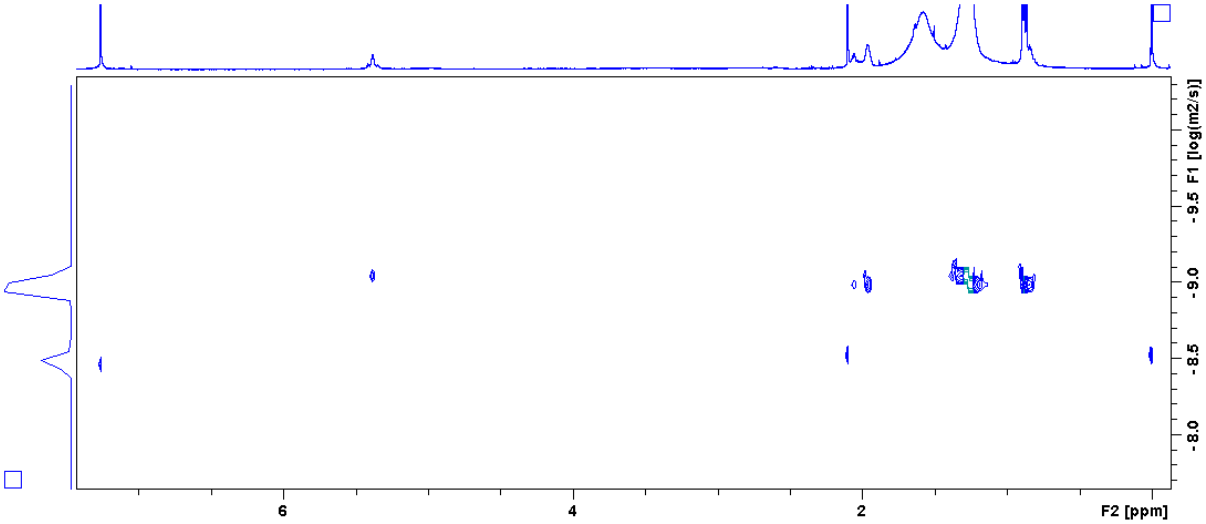

Figure A5.7: DOSY spectrum of $MoSe_2$-OAm/ODE.